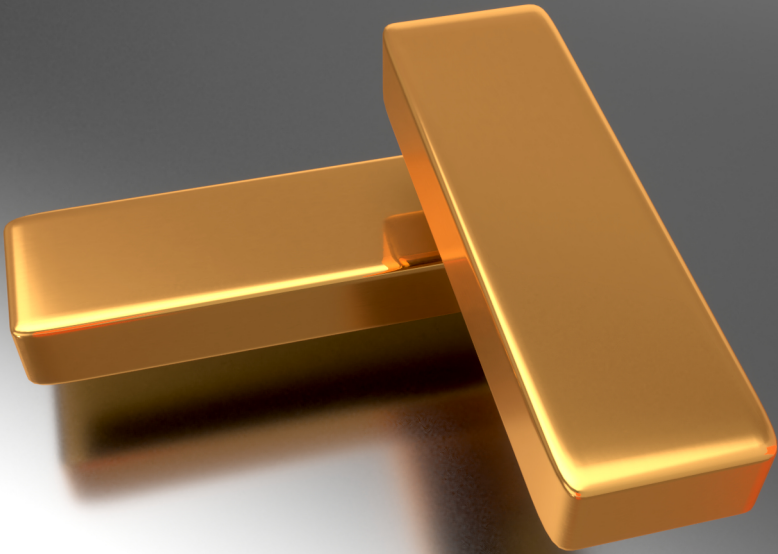
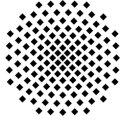


Theory of nonlinear nanophotonics

Josselin Defrance



University of Stuttgart
2020



University of Stuttgart
Germany

Theory of nonlinear nanophotonics

Von der Fakultät Mathematik und Physik der Universität Stuttgart
zur Erlangung der Würde eines Doktors der
Naturwissenschaften (Dr. rer. nat.) genehmigte Abhandlung

Vorgelegt von
Josselin Defrance
aus Clermont-Ferrand (Frankreich)

Hauptberichter:	Jun. -Prof. Dr. Thomas Weiss
Vorsitzender:	Prof. Dr. Sebastian Loth
Mitberichter:	Prof. Dr. Eric Lutz

Tag der Einreichung:	23.06.2020
Tag der mündlichen Prüfung:	15.09.2020

4. Physikalisches Institut der Universität Stuttgart

September 2020

I hereby certify that this dissertation is entirely my own work except where otherwise indicated. Passages and ideas from other sources have been clearly indicated.

Stuttgart, September 2020
Josselin Defrance

To my family

Contents

Abbreviations	11
Abstract	14
Publications	18
1 Introduction	19
2 Theoretical approaches in nanophotonics	23
2.1 Introduction	24
2.2 Maxwell's equations	24
2.2.1 Covariant form of Maxwell's equations	24
2.2.2 Matrix formulation of Maxwell's equations	29
2.3 Plane wave decomposition	30
2.4 Reciprocity principle	32
2.5 Resonant states	36
2.6 The Fourier modal method	39
2.6.1 Basic principles of the Fourier modal method	39
2.6.2 The scattering matrix formalism	46
2.7 Derivation of resonant poles within the scattering matrix formalism	47
3 Mittag Leffler expansion of electromagnetic fields	50
3.1 A new pole expansion	51
3.1.1 The Mittag-Leffler expansion	51
3.1.2 General formulation	55
3.2 Numerical results	56
3.2.1 Dielectric slab	56
3.2.2 Convergence of pole expansion approaches	58
3.2.3 Reflectance and transmittance expansion	63
3.2.4 Efficiency of the method applied to periodic structures	65
4 Nonlinear optics	71
4.1 Introduction	72
4.2 Different microscopic models	72
4.3 Non-propagative and reciprocity based approaches	75
4.3.1 The non-propagative method	75
4.3.2 Emission by reciprocity	75

4.4	Nonlinear optics in modal methods	78
4.4.1	Inhomogeneous Maxwell's equations	78
4.4.2	Factorization rules	82
4.4.3	Scattering matrix of an emitted field	85
4.4.4	Numerical calculations	87
4.5	Modeling of harmonic generation within the pole expansion	91
4.5.1	Theoretical formulation and mode matching	91
4.5.2	Numerical analysis	97
4.6	Kerr optical effect	100
4.6.1	Modeling of a third order nonlinear effect	100
4.6.2	Numerical example	103
5	Experimental and numerical study of third-harmonic generation	109
5.1	Nonlinear optics within chiral systems	110
5.1.1	Linear and nonlinear circular dichroism	110
5.1.2	Numerical model and experiment	112
5.2	Influence of symmetry breaking on the third-harmonic generation	118
5.2.1	Electromagnetically induced absorption	118
5.2.2	Enhanced third-harmonic generation in dolmen structures	124
6	Conclusion and outlook	128
	Bibliography	132
	Art work	143
	Acknowledgment	144

Abbreviations

Technical abbreviations:

FMM	Fourier modal method
ASR	adaptive spatial resolution
S-matrix	scattering matrix
s	from German <i>senkrecht</i> = perpendicular
p	parallel

General definitions:

$\alpha, \beta, \gamma, \sigma$	variable integers for components 1, 2, 3 of three-dimensional vectors unless specified
nm	variable integers or placeholders for integers
$\epsilon^{\alpha\beta\gamma}$	Levi-civita symbol, see equation (2.13)
\mathbf{B}	three-dimensional vector
\mathbf{e}^α	contravariant basis vectors
\mathbf{e}_α	covariant basis vectors
B^α, C^α	contravariant vector components
B_α, C_α	covariant vector components
\mathbb{U}, \mathbb{V}	six-dimensional super-vector containing the components of electric and magnetic fields
$\mathbb{U}_\mathbf{E}, \mathbb{U}_\mathbf{H}$	vectors containing the electric and magnetic field components of \mathbb{U}

Physical quantities:

c	speed of light in vacuum
ε, μ	permittivity and permeability tensors with components $\varepsilon^{\alpha\beta}$ and $\mu^{\alpha\beta}$, respectively
ζ, ξ	bi-anisotropic tensors
ρ	charge term
ω	angular frequency
k_0, k	vacuum wave number $k_0 = \frac{\omega}{c}$
\mathbf{k}, k_α	incident wave vector and its covariant components
\mathbf{E}, E_α	electric field and its covariant components
\mathbf{H}, H_α	magnetic field and its covariant components
\mathbf{D}, D^α	electric displacement and its contravariant components
\mathbf{B}, B^α	magnetic induction and its contravariant components
\mathbf{j}, j^α	current vector and its contravariant components
\mathbf{P}, P^α	nonlinear polarization vector and its contravariant components
$\chi^{(2)}, \chi^{(3)}$	second- and third-order nonlinear susceptibilities
\mathbf{G}, \mathbf{K}	lattice vector and the associated in-plane momentum
$\mathbf{G}_{\alpha m}$	lattice vector component
$K_{\alpha, m}$	$K_{\alpha m} = k_\alpha + G_{\alpha m}$

Coordinate systems:

\mathbf{r}	three-dimensional vector with spatial components
x, y, z, \bar{x}^α	Cartesian coordinates
x^α	general non-uniform coordinates
$\partial_\alpha, \frac{\partial}{\partial x^\alpha}$	derivative with respect to x^α
$J_{\bar{x} \rightarrow x}$	Jacobian matrix, see equation (2.2)
Λ_β^α	component of the Jacobian matrix $J_{\bar{x} \rightarrow x}$
\sqrt{g}	determinant of the Jacobian matrix $J_{x \rightarrow \bar{x}}$
θ	polar incidence angle as angle between incident wave vector and z axis
ϕ	azimuth incidence angle as angle between x axis and projection of incident wave vector on xy plane

Special quantities:

\mathbb{J}	source current super-vector
$\mathbb{J}_A, \mathbb{F}_A$	current super-vector belonging to the source A and the corresponding radiated field super-vector
\mathbb{F}_n	field super-vector of the resonant pole n
\mathbb{I}, \mathbb{O}	Super-vectors of plane wave basis describing incoming and out going fields
$\hat{\mathbb{M}}$	Maxwell's operator
$\hat{\mathbb{G}}$	Green's dyadic
$\mathbb{B}_V, \mathbb{B}_{\partial\nu}$	vector functions defined by equations (2.43) and (2.42)
$F_{\alpha mn}$	Fourier coefficient of order mn for vector component F_α
\hat{l}_α^-	Li operator, see equation (2.73)
$\hat{m}_\alpha^-, \hat{j}_\alpha^-$	Fourier factorization operators, see equations (4.15) and (4.17)
$\tilde{\varepsilon}, \tilde{\mu}$	Fourier transform of permittivity and permeability tensors
$\tilde{\varepsilon}, \tilde{\mu}$	$\hat{l}_3^-(\tilde{\varepsilon})$ and $\hat{l}_3^-(\tilde{\mu})$, respectively
γ_m, Γ_l^\pm	eigenvalues of equation (2.75) and eigenvalue matrix, with $+/-$ indicating the subsets of forward/backward propagating or decaying solutions in direction x^3 and layer l
\tilde{M}	operator of the eigenvalue equation (2.75)
\mathcal{E}, \mathcal{F}	eigenvector and material matrix
\mathbf{A}_l^\pm	vector of expansion coefficients for forward or backward propagation or decay in layer l
$S_{l,l'}$	scattering matrix between the position x_l^3 (top) and the position $x_{l'}^3$ (bottom)

Abstract

Nonlinear optical phenomena represent a large family of effects. We can cite for instance Raman and Brillouin scatterings, second-, third- and higher-harmonic generations as well as sum-frequency generation and Kerr optical effect. These phenomena are often neglected; however they might appear in nanophotonic systems. While micro- or nano-structured media can be tailored in order to control far-field emission pattern and achieve high intensities in the near-field, it is known that resonantly enhanced near-fields can produce significant nonlinear optical phenomena. As a consequence, nonlinear nanophotonics has been subject to many investigations in the last years [1, 2].

In this thesis, we aim to solve linear and nonlinear Maxwell's equations within layered nanostructures at a reasonable numerical cost. To achieve this goal, we will use the scattering matrix formalism as well as the Fourier modal method also called rigorous coupled wave analysis [3, 4]. While the Fourier modal method will be used as the main solver this entire thesis long, we will discuss in detail different approaches that can be implemented upon the Fourier modal method to solve linear and nonlinear Maxwell's equations.

In recent years, it has been shown that the near- and far-field properties of nanostructures can be described using a basis of resonant states, also known as quasi-normal modes. This approach is extremely fast and can be implemented upon existing solvers. In this thesis, we will describe the mathematics behind the decomposition of the inner fields of a structure over its resonant poles. Then, we provide a new formulation of the pole-expansion of electromagnetic fields that we will compare with the older formulation.

Then, we discuss a first approach that describes nonlinear optical phenomena by solving nonlinear Maxwell's equations [5]. In this approach, we explain the implementation of new factorization rules for nonlinear susceptibility and matched coordinates that are indispensable to achieve accurate results with the Fourier modal method. Then we show that the speed of such method can be improved using the pole expansion approach for the nonlinear emission problem.

In addition, the pole expansion provides a deep insight in the description and understanding of nonlinear phenomena within nanostructures. Indeed, this method leads to an analytic expression measuring the impact of symmetries and the importance of a resonant excitation of nanoparticles in the generation of second and higher harmonics.

Thus, this thesis presents a full set of approaches for the description of nonlinear phenomena within nanostructures. Additionally, these methods are used to calculate second- and third-harmonic generations as well as the Kerr optical effect within nanostructures of different shapes.

Finally, we compare the results of our method with experimental results on the generation of third harmonic within rather complex plasmonic systems, which are subject to the chiroptical effect in the first example [6] and plasmonic dark modes hybridization in a second example [7].

Zusammenfassung

Nichtlineare optische Phänomene repräsentieren eine große Anzahl an Effekten. Beispiele dafür sind die Raman- und Brillouin-Streuung, Frequenzverdopplung und -verdreifachung und allgemein die Erzeugung von höheren Harmonischen, Summenfrequenzerzeugung und der optische Kerr-Effekt. Diese Phänomene werden in vielen Fällen vernachlässigt; allerdings können sie in nanophotonischen Systemen auftreten. Während mikro- oder nanostrukturierte Materialien modifiziert werden können, um das Fernfeld zu kontrollieren und hohe Intensitäten im Nahfeld zu erzielen, ist bekannt, dass resonant verstärkte Nahfelder signifikante nichtlineare optische Phänomene hervorrufen. Folglich ist das Gebiet der nichtlinearen Nanophotonik in den letzten Jahren zum Gegenstand zahlreicher Untersuchungen geworden [1, 2].

Das Ziel dieser Arbeit ist die Lösung der linearen und nichtlinearen Maxwell-Gleichungen bei mehrlagigen Nanostrukturen mit vertretbarem numerischen Aufwand. Um dieses Ziel zu erreichen, verwenden wir den Streumatrix-Formalismus und die Fourier-Modal-Methode, auch bekannt als rigorose gekoppelte Wellenanalyse [3, 4]. Während im Wesentlichen die Fourier-Modal-Methode verwendet wird, werden wir im Detail die verschiedenen Ansätze diskutieren, die wir implementiert haben, um die linearen und nichtlinearen Maxwell-Gleichungen zu lösen.

In den letzten Jahren wurde gezeigt, dass die Nahfeld- und Fernfeldeigenschaften von Nanostrukturen durch eine Basis von resonanten Zuständen beschrieben werden können, auch bekannt als quasinormale Moden. Dieser Ansatz ist extrem schnell und kann einfach implementiert werden. In dieser Arbeit beschreiben wir die Mathematik hinter der Zerlegung der inneren Felder einer Struktur über ihren resonanten Polen. Dann präsentieren wir eine neue Formulierung der Polentwicklung von elektromagnetischen Feldern, den wir mit der alten Formulierung vergleichen.

Dann diskutieren wir einen ersten Ansatz zur Beschreibung nichtlinearer optischer Phänomene durch die Lösung der nichtlinearen Maxwell-Gleichungen [5]. In diesem Ansatz erklären wir die Implementierung von neuen Faktorisierungsregeln für die nichtlineare Suszeptibilität und angepassten Koordinaten, die unverzichtbar sind, um akkurate Ergebnisse mit der Fourier-Modal-Methode zu erzielen. Anschließend zeigen wir, dass die Geschwindigkeit der Methode verbessert werden kann, indem der Polentwicklungsansatz für das nichtlineare Emissionsproblem verwendet wird.

Zusätzlich bietet die Polentwicklung tiefe Einsichten in die Beschreibung und das Verständnis von nichtlinearen Phänomenen in Nanostrukturen. Tatsächlich führt diese Methode zu einem analytischen Ausdruck, der den Einfluss von Symmetrien und die Bedeutung von resonanter Anregung von Nanopartikeln bei der Erzeugung von höheren Harmonischen beschreibt.

Somit präsentiert diese Arbeit eine ganze Reihe von Methoden für die Beschreibung von nichtlinearen Phänomenen in Nanostrukturen. Zusätzlich werden diese Methoden benutzt, um Frequenzverdopplung und Frequenzverdreifachung sowie den optischen Kerr-Effekt in Nanostrukturen mit verschiedener Form zu berechnen.

Zum Schluss vergleichen wir die Ergebnisse unserer Methoden mit experimentellen Ergebnissen von Frequenzverdreifachung in komplexen plasmonischen Systemen, die im ersten Beispiel einen chiro-optischen Effekt [6] und im zweiten Beispiel dunkle Moden durch plasmonische Hybridisierung [7] zeigen.

Publications

Parts of this work have already been published:

- J. Defrance, M. Schaferling, and T. Weiss, “Modeling of second-harmonic generation in periodic nanostructures by the Fourier modal method with matched coordinates,” *Opt. Express* **26**, 13746–13758 (2018).
- J. Krauth, T. Schumacher, J. Defrance, B. Metzger, M. Lippitz, T. Weiss, H. Giessen, and M. Hentschel, “Nonlinear Spectroscopy on the Plasmonic Analog of Electromagnetically Induced Absorption: Revealing Minute Structural Asymmetries,” *ACS Photonics* **6**, 2850–2859 (2019).
- L. Gui, M. Hentschel, J. Defrance, J. Krauth, T. Weiss, and H. Giessen, “Nonlinear Born-Kuhn Analog for Chiral Plasmonics,” *ACS Photonics* **6**, 3306–3314 (2019).

Publications under review:

- J. Defrance, and T. Weiss, “On the pole expansion of electromagnetic fields,” *Opt. Express*, (2020).

Publications in preparation:

- J. Defrance, and T. Weiss, “On the Kerr optical effect within the pole expansion approach,” (2020).

1 Introduction

If you want to find the secrets of the universe, think in terms of energy, frequency and vibration.

Nikola Tesla (1856-1943)

I insist upon the view that 'all is waves'.

Erwin Schrödinger (1887-1951)

Light-matter interactions represent a very large field of study. From the pioneering work of Descartes and Newton in optics and infinitesimal calculus, to the formulation of Maxwell's equations [8], this topic has greatly evolved over the past centuries. In recent years, modern theoretical advances and the development of new fabrication methods for nanostructured media opened large perspectives in nanophotonics.

Though the intrinsic polarizability of a medium defines most of its optical properties, it is possible to build mediums with artificial optical characteristics by the means of nanostructures [9–11]. Indeed, the effective magnetic and electric polarizabilities of a material can be tailored by nanostructuring the material at the scale of optical wavelengths. For instance, by these methods it is possible to mimic natural nanostructures such as feather tails and butterfly wings to produce bright structural colors [12–14]. Beyond natural phenomena, periodic nanostructures such as photonic crystals and metamaterials provide many different kinds of effects used for example in perfect absorbers [15, 16], optical wave-guides [17, 18] and chemical sensors [19, 20].

Most of nano-structured materials contain metallic particles that exhibit plasmonic resonances. Plasmon resonances are collective oscillations of free electrons within metallic structures. We distinguish two types of plasmon resonances, propagating plasmon polariton occurring at metallo-dielectric interfaces and standing particle resonances. These types of resonant modes are able to focus intense electromagnetic fields in deep sub-wavelength volumes. At large intensities, electromagnetic fields are subject to a very broad family of nonlinear optical phenomena. Though in quantum mechanical representations even vacuum exhibits nonlinear properties, note that in classical approaches nonlinear phenomena concern just light-matter interactions. These interactions are theoretically expressed within the so called constitutive equations that describe the local polarization of matter induced by an external electromagnetic field. This process can be subject to non-locality [21]. Although in linear optics the polarization of matter is expressed as susceptibility tensors multiplied by the components of the incoming electromagnetic field, it is an approximation. Light-matter interactions are merely governed by the an-harmonic oscillations of charged particles, such as free and bounded electrons, induced by an incoming field. As a consequence the induced polarization-field contains harmonics of the excitation frequency. In the constitutive equations the electric nonlinear polarization is expressed as higher order tensors multiplied multiple times with the components of electric field. Thus, in simple models the nonlinear polarization is proportional to the incoming field raised to the power two or higher. Many materials exhibit a very small nonlinear suscepti-

bility and thus a negligible nonlinear polarization. However, there exist some materials such as GaAs that exhibit high optical nonlinearities. Additionally, a n^{th} -order nonlinear polarization scales with the amplitude of the pump field raised to the power n . As a consequence, even-though the metal of a nano-particle do not own a high nonlinear susceptibility, the strongly enhanced near fields in the vicinity of the particle can be subject to nonlinear phenomena [1, 22–24].

Nonlinear optical phenomena proved to be indispensable tools in many domains. We can cite for instance, fiber-amplifiers and wavelength multiplexer for telecommunications, microscopes [24, 25], chemical sensors [2, 26, 27]. As a consequence, while nanostructures are able to drastically enhance nonlinear optical phenomena, the tailoring of nonlinear effects at the scale of nanostructures is still an active field of research. Indeed, though the influence of crystalline symmetries is well understood and described within the formalism of susceptibility tensors, the conjunction of structural symmetries with the optical susceptibilities of materials within nanostructures to produce nonlinear responses is not well understood.

In this context, numerical algorithms calculating the linear and nonlinear behavior of plasmonic nanostructures offer good optimization tools and provide the mean to achieve a better understanding of these phenomena. Different approaches have been developed to account for the nonlinear contributions to Maxwell’s equations in either time or frequency domain [28, 29]. Plasmonic structures are often produced as layers of patterns repeated periodically in one or two dimensional arrays. This type of structure is typically produced using lithographic methods and numerical modal methods are the most suited tools to solve Maxwell’s equations in such layered systems. These methods belong to the category of frequency domain solvers, which resolve Maxwell’s equations for one single frequency in each calculation. In addition, these methods require a numerical discretization only along two directions. Indeed, in the stacking direction of the layered system, one searches for eigenmodes that can propagate or decay for each layer. These eigenmodes serve as a basis for deriving the propagation of fields through a layer, which is usually carried out by the scattering matrix approach [3]. In the case of the Fourier modal method, the eigenmodes are calculated by decomposing Maxwell’s equations in a finite Fourier basis. This implies periodic boundary conditions that are the reason why the Fourier modal method is ideal for layered periodic structures.

The thesis is structured as follows: In chapter 2, we express Maxwell’s equations within the formalism of general coordinate systems that is indispensable for the modeling of nanostructures with arbitrary shapes. In

a second step, we introduce the matrix formulation of Maxwell's equations. This new formulation proved to be extremely useful and leads us to the expression of the reciprocity principle, in addition to the resolution of Maxwell's equations using the pole expansion approach. Finally, this chapter ends with a detailed description of the Fourier modal method (FMM) within the scattering matrix formalism. The description includes a reminder about factorization rules [4, 30] and adaptive spatial resolution [31, 32] that we might re-define in a broader picture, further in the thesis. In chapter 3, we present a detailed description of the Mittag's Leffler theorem and the associated series expansion. Then, we use the properties of the latter to solve Maxwell's equations using a different approach from the standard pole expansion [33]. The novel as well as the older formulation of the pole expansion improves significantly the calculation speed of frequency domain solvers that will be relevant in the resolution of nonlinear Maxwell's equations, which is known to be time consuming. In chapter 4 we will study three different approaches to compute nonlinear optical phenomena using the Fourier modal method as the main solver. The first method calculates the second-harmonic generation within the Fourier modal method using a direct emission scheme. We consider materials with nonlinear properties as volumetric sources, thus the emission of these sources to the far field at the harmonic frequency is calculated using the scattering matrices formalism. A second method expresses the field scattered at the harmonic frequency in the same fashion as the field scattered at the pump frequency, using the pole expansion approach. Finally, the last method uses an indirect scheme based on the reciprocity principle. The radiation of the nonlinear material to the far field is calculated as the overlap integral of two quantities: The nonlinear polarization expressed as a source current and the near field scattered by plane waves propagating in the inverse direction, from far to near field at the harmonic frequency. In the chapter 5 we study the third-harmonic generation in two rather complex nanostructures. In the first system, we compute the third-harmonic generated in a chiral plasmonic structure [6, 34–36]. In the second system, we study the influence of plasmonic dark modes and symmetry breaking, in the enhancement of third-harmonic generation in metallic nanostructures [7, 37].

2 Theoretical approaches in nanophotonics

A scientist is happy, not in resting on his attainments but in the steady acquisition of fresh knowledge.

Max Planck (1858-1947)

2.1 Introduction

Though the context and the reasons why we need to further improve numerical methods has been discussed, we might now introduce the state of the art in this field. The resolution of Maxwell's equations using modal methods have been a field of research for a few decades now. Originally, the Fourier modal method (also called rigorous coupled wave analysis, RCWA) had few issues in the calculation of transverse magnetic fields (i.e. p-polarized fields). L. Li proposed later his so called Fourier factorization rules [38], which account for the limited size of the reciprocal basis used in modal methods. The factorization rules improved greatly the Fourier modal method, however issues with metal dielectric or curved interfaces were still hampering the accuracy of the method. These two problems were tackled by the implementation of adaptive spatial resolution and general coordinates within the numerical scheme achieved by G. Granet and T. Weiss [31, 32]. This new feature enables the use of stretched and matched coordinates. On one hand, the stretched coordinates strongly reduce the Gibbs phenomenon, which was the origin of the convergence issues aforementioned for metallo-dielectric interfaces. On the other hand, it allows the description of curved interfaces by surfaces of constant coordinates, which prevent the use of staircase approximation, another source of inaccuracy in the older approach.

The implementation of the Fourier modal method with factorization rules and adaptive spatial resolution exhibits very good convergence pattern in most cases and thus it is ready for the implementation of more complicated schemes, for instance the description of nonlinear optical phenomena. Additionally, new approaches based on a semi-analytic scheme solving Maxwell's equations using Mittag-Leffler series expansion offer a plethora of possible improvements.

In this chapter we will introduce the necessary formalism and the ideas necessary to push the Fourier modal method further and use pole expansion approaches in more situations than the traditional ones.

2.2 Maxwell's equations

2.2.1 Covariant form of Maxwell's equations

In the following chapters, we will use the CGS (centimeters, grams and seconds) unit system and the covariant notation, which provides an efficient tool for the description of electromagnetic fields in general coordinates. Additionally, bold letters in this document will refer to vector quantities.

The covariant formalism describes spatial dimensions using two reciprocal bases, the covariant basis $(\mathbf{e}_1, \mathbf{e}_2, \mathbf{e}_3)$ and the contravariant basis $(\mathbf{e}^1, \mathbf{e}^2, \mathbf{e}^3)$ that we will define in this discussion. Thus, covariant quantities own a lower index and contravariant one's own an upper index. The product of elements of each basis sharing the same symbol as lower and upper index $U^\alpha V_\alpha$, implicitly refers to the sum convention over the three dimensions:

$$U^\alpha V_\alpha \equiv \sum_{\alpha=1}^3 U^\alpha V_\alpha. \quad (2.1)$$

Let us first assume the coordinate transformation from a Cartesian coordinate system $(O, \bar{x}^1, \bar{x}^2, \bar{x}^3)$ to non-uniform (curvilinear) coordinates (O, x^1, x^2, x^3) , in a flat space. Depending whether a physical quantity is expressed in Cartesian coordinates or general coordinates, it will be written with or without an upper bar. The Jacobian matrix of the transformation from Cartesian to the curvilinear system is denoted by:

$$J_{\bar{x} \rightarrow x} = \begin{pmatrix} \frac{\partial x^1}{\partial \bar{x}^1} & \frac{\partial x^1}{\partial \bar{x}^2} & \frac{\partial x^1}{\partial \bar{x}^3} \\ \frac{\partial x^2}{\partial \bar{x}^1} & \frac{\partial x^2}{\partial \bar{x}^2} & \frac{\partial x^2}{\partial \bar{x}^3} \\ \frac{\partial x^3}{\partial \bar{x}^1} & \frac{\partial x^3}{\partial \bar{x}^2} & \frac{\partial x^3}{\partial \bar{x}^3} \end{pmatrix}. \quad (2.2)$$

In the Cartesian coordinates, the covariant and contravariant basis vectors are the unit vectors $\bar{\mathbf{e}}_\alpha$. In addition, the coordinates of any point in space are defined relatively to an origin by a linear combination of translations expressed using the coordinate vector defined as $\mathbf{r}(\bar{x}^1, \bar{x}^2, \bar{x}^3) = \bar{x}^\alpha \bar{\mathbf{e}}_\alpha$. In curvilinear coordinates, the latter vector becomes

$$\mathbf{r}(x^1, x^2, x^3) = \bar{x}^\alpha (x^1, x^2, x^3) \bar{\mathbf{e}}_\alpha. \quad (2.3)$$

In curvilinear coordinates, the vectors of the covariant basis at the position $\mathbf{r}(x^1, x^2, x^3)$ are the tangents of the curves $\mathbf{r}(x^1, c^2, c^3)$, $\mathbf{r}(c^1, x^2, c^3)$ and $\mathbf{r}(c^1, c^2, x^3)$, where c^1 , c^2 and c^3 are constants. Similarly, the vectors of the contravariant basis are the normals of the surfaces of constant parameters, $x^\alpha = \text{constant}$. Thus, the vectors of the covariant and contravariant basis in curvilinear coordinates are defined as

$$\mathbf{e}_\alpha = \frac{\partial \mathbf{r}}{\partial x^\alpha}, \quad (2.4)$$

$$\mathbf{e}^\alpha = \bar{\nabla} x^\alpha. \quad (2.5)$$

As you can see in Fig. 2.1, the direction and the norm of the co- and contravariant basis vectors depend on the spatial position marked as a

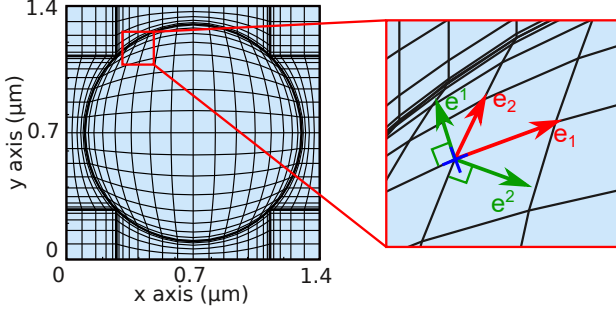


Figure 2.1: Example of two-dimensional curvilinear coordinates with a line of constant coordinates matching the shape of a circle of radius $r=300$ nm. In this curvilinear coordinate system the characteristics of the covariant and contravariant basis vary with the spatial position. At the position of the blue cross, the directions of the covariant and contravariant basis vectors are given by red and green arrows, respectively.

blue cross in the figure. As a consequence, in stretched or curvilinear coordinates the Jacobian matrix and the weight \sqrt{g} are functions of space.

In general coordinates, physical quantities as vectors are represented within the two reciprocal bases with the decomposition:

$$\mathbf{U} = U^\alpha \mathbf{e}_\alpha, \quad \& \quad \mathbf{U} = U_\alpha \mathbf{e}^\alpha, \quad (2.6)$$

The transformation of a vector of weight W from Cartesian coordinates to curvilinear coordinates is obtained using the elements of the Jacobian matrix $J_{\bar{x} \rightarrow x}$ written as $\Lambda_\beta^\alpha = \partial x^\alpha / \partial \bar{x}^\beta$. Thus,

$$U^\alpha = \bar{U}^\beta \Lambda_\beta^\alpha \sqrt{g}^W, \quad \& \quad \bar{U}_\alpha = U_\beta \Lambda_\alpha^\beta \sqrt{g}^W, \quad (2.7)$$

where \sqrt{g} is the determinant of the Jacobian matrix of the inverse transformation $J_{x \rightarrow \bar{x}}$. Depending on their properties, physical quantities carry different weights.

The covariant form of the electric and magnetic fields have a weight zero, the contravariant form of the current vector, the magnetic induction, the displacement and the polarization fields are of weight one. The transformation of these quantities from Cartesian to curvilinear coordinates yields

$$E_\alpha = \bar{E}_\beta \Lambda_\alpha^\beta, \quad H_\alpha = \bar{H}_\beta \Lambda_\alpha^\beta, \quad (2.8)$$

$$D^\alpha = \bar{D}^\beta \sqrt{g} \Lambda_\beta^\alpha, \quad B^\alpha = \bar{B}^\beta \sqrt{g} \Lambda_\beta^\alpha, \quad (2.9)$$

$$P^\alpha = \bar{P}^\beta \sqrt{g} \Lambda_\beta^\alpha, \quad J^\alpha = \bar{J}^\beta \sqrt{g} \Lambda_\beta^\alpha. \quad (2.10)$$

The dielectric permittivity and permeability are tensors of second order with a weight one:

$$\varepsilon^{\alpha\beta} = \bar{\varepsilon}^{\rho\tau} \sqrt{g} \Lambda_\rho^\alpha \Lambda_\tau^\beta, \quad \mu^{\alpha\beta} = \bar{\mu}^{\rho\tau} \sqrt{g} \Lambda_\rho^\alpha \Lambda_\tau^\beta. \quad (2.11)$$

Finally the charge density is a scalar quantity of weight 1:

$$\rho = \bar{\rho} \sqrt{g}. \quad (2.12)$$

In covariant notation the vector product and the curl operator are expressed using the Levi-Civita symbol:

$$\epsilon^{\alpha,\beta,\gamma} = \begin{cases} 1, & \text{for } \alpha\beta\gamma = \{123, 231, 312\}; \\ -1, & \text{for } \alpha\beta\gamma = \{321, 213, 132\}; \\ 0, & \text{otherwise.} \end{cases} \quad (2.13)$$

The weight of this operator is directly linked to the deformation of the parallelepiped whose edges are the vectors of the covariant basis. The volume of this parallelepiped is locally expressed as a vector product:

$$V_u = \mathbf{e}_\alpha \epsilon^{\alpha,\beta,\gamma} \mathbf{e}_\beta \mathbf{e}_\gamma. \quad (2.14)$$

This elementary volume is equal to the determinant of the inverse Jacobian matrix $V_u = \sqrt{g}$ that is unitary in Cartesian coordinates $\bar{V}_u = 1$. Nonetheless, V_u is not unitary in curvilinear coordinates. As a consequence, the Levi-Civita symbol owns a weight one:

$$\epsilon^{\alpha\beta\gamma} = \bar{\epsilon}^{\mu\nu\tau} \sqrt{g} \Lambda_\mu^\alpha \Lambda_\nu^\beta \Lambda_\tau^\gamma, \quad (2.15)$$

and \sqrt{g} can be regarded as a volumetric normalization or a density [39]. The previous demonstrations and definitions provide a rather detailed description of electromagnetic fields in general coordinates. We might conclude this demonstration with the expression of linear Maxwell's equations in covariant notation [32]:

$$\partial_\alpha D^\alpha = 4\pi\rho, \quad (2.16)$$

$$\partial_\alpha B^\alpha = 0, \quad (2.17)$$

$$\epsilon^{\alpha\beta\gamma} \partial_\beta E_\gamma = ik_0 \mu^{\alpha\beta} H_\beta, \quad (2.18)$$

$$\epsilon^{\alpha\beta\gamma} \partial_\beta H_\gamma = -ik_0 \varepsilon^{\alpha\beta} E_\beta. \quad (2.19)$$

The reader will recognize that in each of these equations the left and right terms of the equality have a total weight of one. Thus, the Maxwell's

equations are invariant under coordinate transformation. Similarly, we can derive the constitutive equations that embrace the same property:

$$D^\gamma = \varepsilon^{\gamma\beta} E_\beta + \xi^{\gamma\alpha} H_\alpha, \quad (2.20)$$

$$B^\gamma = \mu^{\gamma\beta} H_\beta + \zeta^{\gamma\alpha} E_\alpha. \quad (2.21)$$

Here, $\xi^{\gamma\alpha}$ and $\zeta^{\gamma\alpha}$ known as bi-anisotropic contributions are second-order tensors of weight one.

It has been demonstrated that Maxwell's equations can be solved for circular and other geometries in general coordinates. The use of curvilinear coordinates is eminently useful for numerical methods. Resolving accurately the optical properties of a structure with curved interfaces requires curvilinear coordinates and the definition of surfaces of constant coordinates that match the interfaces of the structure of interest. At this condition, the normal and tangential components of the field are defined correctly and the numerical description of curved interfaces does not suffer from artificial discontinuities due to spatial discretization.

Though coordinate transformation is a useful tool for numerical methods, it carries a physical meaning. For instance, changing the optical properties of a particle or applying the corresponding change in the structural geometry of the same object is equivalent. This characteristic is the equivalence principle, thus a particle with an arbitrary shape made of homogeneous material, is equivalent to a cubic particle made of a corresponding non-trivial material. The permittivity and permeability of the latter material in Cartesian coordinates is defined by the transformation of these tensors from the matched coordinates basis to the Cartesian one. This principle is intensively used in transformation optics for the nano-structuring and the shaping of materials to achieve new artificial permittivities and permeabilities [40–42]. Such materials are usually called metamaterials, amidst them a large family containing materials made of metallic particles that are the subject of intense research because of the properties they exhibit. Indeed, metallic materials are subject to plasmonic resonances which are collective oscillations of free electrons at interfaces that couple with incoming light. Nanostructured media containing metallic particles are experimentally built with few methods such as electron beam lithography. Thus, such structures are organized in planar layers stacked on top of each other. In the case the layers are periodic in one or two directions with a common translational symmetry and invariant in the stacking direction, the structure can be perfectly described numerically using the Fourier modal method. This numerical method will be described in the last section of this chapter. However, in the following calculations we will assume that the dielectric permittivity and the magnetic permeability are defined

in general coordinates such that our demonstrations remain as general as possible.

2.2.2 Matrix formulation of Maxwell's equations

"As is often the case in mathematics and physics, a good notation is half the battle" [43]. Thus, depending on the goal to be achieved, one or the other formulation of Maxwell's equations is required. Besides the usual vector forms, these equations possess matrix formulations, the most known is using the four dimensional electromagnetic tensor eminently useful in electrodynamics [39]. However, another matrix formulation exists, it can be written in frequency domain [time dependence $\exp(-i\omega t)$, Gauss units, wavenumber $k = \omega/c$] as [44]:

$$\hat{\mathbb{M}}(\mathbf{r}; k)\mathbb{F}(\mathbf{r}; k) = \mathbb{J}(\mathbf{r}; k), \quad (2.22)$$

where $\hat{\mathbb{M}}(\mathbf{r}; k) = k\hat{\mathbb{P}}(\mathbf{r}; k) - \hat{\mathbb{D}}(\mathbf{r})$ assuming:

$$\hat{\mathbb{P}}(\mathbf{r}; k) = \begin{bmatrix} \varepsilon(\mathbf{r}; k) & -i\xi(\mathbf{r}; k) \\ i\zeta(\mathbf{r}; k) & \mu(\mathbf{r}; k) \end{bmatrix}, \quad \hat{\mathbb{D}}(\mathbf{r}) = \begin{pmatrix} 0 & \nabla \times \\ \nabla \times & 0 \end{pmatrix}, \quad (2.23)$$

where ε , μ , ζ and ξ are the dielectric permittivity, the dielectric permeability, and possible bi-anisotropic contributions, respectively. The six-dimensional supervector \mathbb{F} contains the electric and magnetic fields denoted by \mathbf{E} and \mathbf{H} . The current supervector \mathbb{J} contains an electric source current $\mathbf{J}_E = -4\pi\mathbf{j}/c$ and a magnetic current \mathbf{J}_H introduced for symmetry reasons,

$$\mathbb{F}(\mathbf{r}; k) = \begin{bmatrix} \mathbf{E}(\mathbf{r}; k) \\ i\mathbf{H}(\mathbf{r}; k) \end{bmatrix}, \quad \mathbb{J}(\mathbf{r}; k) = \begin{bmatrix} \mathbf{J}_E(\mathbf{r}; k) \\ i\mathbf{J}_H(\mathbf{r}; k) \end{bmatrix}. \quad (2.24)$$

The value of the field $\mathbb{F}(\mathbf{r}; k)$ is obtained solving the Maxwell's equations (2.22). A usual method to solve in-homogeneous differential equations makes use of a Green function G that is solution of the equation for a second term equal to a Dirac distribution. The equation (2.22) is written for six dimensional supervectors. Hence, instead of a Green's function, we use the Green's dyadic operator \mathbb{G} that obeys

$$\hat{\mathbb{M}}(\mathbf{r}; k)\hat{\mathbb{G}}(\mathbf{r}, \mathbf{r}'; k) = \mathbb{1}\delta(\mathbf{r} - \mathbf{r}'). \quad (2.25)$$

The solution \mathbb{F} of the inhomogeneous Maxwell's equation is obtained by the convolution of the Green's dyadic with the source current supervector in the region of emission v :

$$\mathbb{F}(\mathbf{r}; k) = \int_v \hat{\mathbb{G}}(\mathbf{r}, \mathbf{r}'; k)\mathbb{J}(\mathbf{r}'; k)dv. \quad (2.26)$$

Though in the latter formula we model only the emission of a source current, the linear properties of a scattering geometry as well as the non-linear process taking place in some materials are well described by source currents. The occurrence of these phenomena in layered media will be the subject of the coming chapters.

2.3 Plane wave decomposition

Let us assume the example of stacked arrays of nanostructures with common translation symmetry. Each layer is invariant along \mathbf{x}^3 and contains nanostructures arranged periodically along one or two directions \mathbf{x}^1 and \mathbf{x}^2 with the periods d_1 and d_2 . Consequently, the layers are stacked along the direction \mathbf{x}^3 . In such periodic structures, the light-matter interaction tensors as the dielectric permittivity can be decomposed in terms of Fourier harmonics. Additionally, the system can be excited by plane waves coming from the top and bottom half spaces above and below the structure. Each incoming plane wave owns a wave vector $\mathbf{k} = (k_1, k_2, k_3)$ that is related to the azimuthal and polar incidence angles θ and ϕ as

$$k_1 = \frac{\omega}{c} \sin(\theta) \cos(\phi), \quad k_2 = \frac{\omega}{c} \sin(\theta) \sin(\phi), \quad (2.27)$$

$$k_3 = \frac{\omega}{c} \cos(\theta). \quad (2.28)$$

Thus, the in-plane momentum $\mathbf{k}_{//} = (k_1, k_2)$ of the incoming plane wave interacts with the pseudo momentum of the structure represented by the Fourier harmonics of the dielectric permittivity and the magnetic permeability. As a consequence, owing to the Bloch's theorem, the system responds by reflecting and transmitting the incoming field in Bragg's diffraction orders that will be a natural basis to represent the fields outside the structure. Bragg's diffraction orders are described by the reciprocal lattice vectors:

$$\mathbf{G} = \left(\frac{2\pi}{d_1} m, \frac{2\pi}{d_2} n \right) \text{ with } m, n \in \mathbb{Z}, \quad (2.29)$$

$$\mathbf{K} \equiv \mathbf{k}_{//} + \mathbf{G}. \quad (2.30)$$

Let us define $K_{\alpha, m} = k_{\alpha} + \mathbf{G}_{\alpha, m}$ with $\mathbf{G}_{\alpha, m} = \frac{2\pi}{d_{\alpha}} m$.

The top and bottom half-spaces are homogeneous sub- and super-strate, thus for every diffraction order of the reciprocal basis \mathbf{K} , we can define one propagation constant:

$$k_{z, \mathbf{K}}^{t/b} = \sqrt{\frac{\omega^2 \varepsilon^{t/b} \mu^{t/b}}{c^2} - \mathbf{K}^2}, \quad (2.31)$$

where the superscript t/b refers to superstrate and substrate material properties.

Through the last equations, we have defined a basis of wave vectors $\mathbf{k}_{\mathbf{K}}^{t/b} = (\mathbf{K}, k_{z,\mathbf{K}}^{t/b})$ for all \mathbf{K} that corresponds to the plane wave basis:

$$\psi_{\mathbf{K},\pm}^{t/b}(\mathbf{r}, k) = e^{i(\mathbf{K}\cdot\mathbf{r}/\pm k_{z,\mathbf{K}}^{t/b}z)}. \quad (2.32)$$

In the case of loss-less surrounding mediums, the propagation constants defined in Eq. (2.31) are either purely real or imaginary. Modes owning purely real propagation constants are loss-less and can propagate from- and to- the far field. Purely imaginary propagation constants describe evanescent fields exponentially decaying in the direction along which the mode would propagate if its eigenvalue had a real part. The sign of the square root in Eq. (2.31) is chosen to obtain forward decaying and propagating fields for a positive \mathbf{x}^3 direction. In the case of complex wave vectors the sign of the square root is chosen to match the sign of the corresponding channel with a real propagation constant.

The Fourier reciprocal basis ensures the conservation of the in-plane momentum of fields that propagate from the far field through the structure. Thus, the tangential components of fields can be written in this reciprocal basis and should remain unchanged on both sides of each interface to fulfill the boundary conditions expressed within Maxwell's equations. This procedure is used in the Fourier Modal method and will be explained later.

The elements of the basis defined above are degenerated over two orthogonal polarizations. To distinguish these two polarization states, we have to introduce a polarization basis. It could be the left and right-circular polarization basis or any set of two orthogonal polarizations. In the current document, we will choose the s- and p-polarizations as a basis. The unit vectors of the Bragg's diffraction order basis Eq. (2.32) are to be, for the s-polarized light:

$$\check{\mathbf{E}}_{s,\mathbf{K},\pm}^{t/b}(k) = \frac{1}{|\mathbf{K}|} \begin{pmatrix} -K_2 \\ K_1 \\ 0 \end{pmatrix}, \quad (2.33)$$

$$\check{\mathbf{H}}_{s,\mathbf{K},\pm}^{t/b}(k) = \frac{1}{|\mathbf{k}_{\mathbf{K}}^{t/b}||\mathbf{K}|} \begin{pmatrix} \mp K_1 k_{z,\mathbf{K}}^{t/b} \\ \mp K_2 k_{z,\mathbf{K}}^{t/b} \\ |\mathbf{K}|^2 \end{pmatrix}. \quad (2.34)$$

K_α refers to the vector components $K_{\alpha m}$ associated to the in-plane

momentum \mathbf{K} . The unit vectors for the p-polarized fields are:

$$\check{\mathbf{E}}_{p,\mathbf{K},\pm}^{t/b}(k) = \mp \check{\mathbf{H}}_{s,\mathbf{K},\pm}^{t/b}(k), \quad (2.35)$$

$$\check{\mathbf{H}}_{p,\mathbf{K},\pm}^{t/b}(k) = \pm \check{\mathbf{E}}_{s,\mathbf{K},\pm}^{t/b}(k). \quad (2.36)$$

Thus, the vectors of the plane-wave basis are written with three subscripts, that describe the polarization state $a \equiv s$ or p , the in-plane momentum in the reciprocal basis \mathbf{K} and the forward or backward directions of propagation $+$ or $-$:

$$\hat{\mathbf{E}}_{a,\mathbf{K},\pm}^{t/b}(\mathbf{r}, k) = N^{t/b} \check{\mathbf{E}}_{a,\mathbf{K},\pm}^{t/b}(k) \psi_{\mathbf{K},\pm}^{t/b}(\mathbf{r}, k), \quad (2.37)$$

$$\hat{\mathbf{H}}_{a,\mathbf{K},\pm}^{t/b}(\mathbf{r}, k) = \frac{N^{t/b}}{Z^{t/b}} \check{\mathbf{H}}_{a,\mathbf{K},\pm}^{t/b}(k) \psi_{\mathbf{K},\pm}^{t/b}(\mathbf{r}, k), \quad (2.38)$$

where $Z^{t/b} = \sqrt{\mu^{t/b}/\varepsilon^{t/b}}$ is the optical impedance, and N is a normalization constant.

Owing to the propagation directions of incoming and outgoing fields in the top and bottom half spaces, we use Eqs. (2.33-2.38) to build the four corresponding bases

$$\mathbb{O}_{a,\mathbf{K}}^t = \mathbb{F}_{a,\mathbf{K},-}^t, \quad \mathbb{I}_{a,\mathbf{K}}^t = \mathbb{F}_{a,\mathbf{K},+}^t, \quad (2.39)$$

$$\mathbb{O}_{a,\mathbf{K}}^b = \mathbb{F}_{a,\mathbf{K},+}^b, \quad \mathbb{O}_{a,\mathbf{K}}^b = \mathbb{F}_{a,\mathbf{K},-}^b, \quad (2.40)$$

where \mathbb{I} and \mathbb{O} are field supervectors built as \mathbb{F} in Eq. (2.24), each field is a function of \mathbf{r} and k .

These four bases provide a precise description of the fields reflected and transmitted by the structure. The incoming and outgoing field profiles are scaled with the size of a single unit cell that is of the order of the field wavelength. Thus, in such a small area, incoming fields might be approximated by a single plane wave while near fields can exhibit more complex spatial distributions. As a consequence, incoming fields often contain one plane wave of the total basis while transmitted and reflected fields are described as superposition of many plane waves.

2.4 Reciprocity principle

The previous section provides a non-exhaustive description of electromagnetic fields outside a layered structure. In the following sections we will study the relations and rules that fields obey at interfaces. To achieve this goal we will formulate the reciprocity principle.

To preserve the clarity of the coming derivations, we introduce two vector functions \mathbb{B}_V and $\mathbb{B}_{\partial\nu}$. We define the new functions using the example of two six-dimensional complex supervectors:

$$\mathbb{U} = \begin{pmatrix} \mathbf{U}_E \\ i\mathbf{U}_H \end{pmatrix}, \quad \& \quad \mathbb{V} = \begin{pmatrix} \mathbf{V}_E \\ i\mathbf{V}_H \end{pmatrix}. \quad (2.41)$$

The first function \mathbb{B}_V is mapping $\mathbb{C}^6 \times \mathbb{C}^6 \rightarrow \mathbb{C}$ and is expressed as a volumetric integral over a finite volume V :

$$\mathbb{B}_V(\mathbb{U}; \mathbb{V}) = \int_V (\mathbf{U}_E \cdot \mathbf{V}_E - \mathbf{U}_H \cdot \mathbf{V}_H) dV. \quad (2.42)$$

\mathbb{B}_V is linear and symmetric.

The second vector function is an integral over the surface ∂V enclosing the volume V :

$$\mathbb{B}_{\partial\nu}(\mathbb{U}; \mathbb{V}) = i \int_{\partial\nu} (\mathbf{U}_E \times \mathbf{V}_H - \mathbf{V}_E \times \mathbf{U}_H) \cdot d\mathbf{S}. \quad (2.43)$$

The latter function is linear and anti-symmetric: $\mathbb{B}_{\partial\nu}(\mathbb{U}; \mathbb{V}) = -\mathbb{B}_{\partial\nu}(\mathbb{V}; \mathbb{U})$. Owing to the properties of the curl operator and the Gauss's theorem, one can write:

$$\mathbb{B}_{\partial\nu}(\mathbb{U}; \mathbb{V}) = \mathbb{B}_V(\mathbb{V}; \hat{\mathbb{D}}\mathbb{U}) - \mathbb{B}_V(\mathbb{U}; \hat{\mathbb{D}}\mathbb{V}). \quad (2.44)$$

In addition, applying the second vector function to the plane wave basis vectors $\hat{\mathbb{F}}$, we find the orthogonality relation:

$$\mathbb{B}_{\partial\nu}(\mathbb{F}_{a,\mathbf{K},+}^R; \mathbb{F}_{a,\mathbf{K}',+}) = \mathbb{B}_{\partial\nu}(\mathbb{F}_{a,\mathbf{K},-}^R; \mathbb{F}_{a,\mathbf{K}',-}) = 0, \quad (2.45)$$

$$\mathbb{B}_{\partial\nu}(\mathbb{F}_{a,\mathbf{K},+}^R; \mathbb{F}_{a,\mathbf{K}',-}) = -\mathbb{B}_{\partial\nu}(\mathbb{F}_{a,\mathbf{K},-}^R; \mathbb{F}_{a,\mathbf{K}',+}) = \delta_{\mathbf{K}\mathbf{K}'} \delta_{a,a'}, \quad (2.46)$$

where the super script R denotes the reciprocal conjugate. In the case of incident plane waves, the reciprocal conjugate denotes plane waves with opposite in-plane wave vector components. In the case of a resonant state, the reciprocal conjugate refers to a resonance at the same energy but with reciprocal boundary conditions.

Abiding by the orthogonality relation above, some calculus demonstrate that N has to fulfill

$$N^{t/b} = \sqrt{i \frac{Z^{t/b} k^{t/b}}{2k_{z,\mathbf{K}}^{t/b}}}. \quad (2.47)$$

Let us study the reciprocity principle applied to a convex volume V , chosen to be one unit cell of a periodic and layered medium (see Fig. 2.2). A thorough description of the reciprocity principle comes through the emitting properties of two sources A and B in the closed volume V . Each of these sources is described by a supervector \mathbb{J} and is radiating an electromagnetic field abiding by Maxwell's equations

$$\hat{\mathbb{M}}(\mathbf{r}; k)\mathbb{F}_A(\mathbf{r}; k) = \mathbb{J}_A(\mathbf{r}; k), \quad (2.48)$$

$$\hat{\mathbb{M}}(\mathbf{r}; k)\mathbb{F}_B(\mathbf{r}; k) = \mathbb{J}_B(\mathbf{r}; k). \quad (2.49)$$

With some calculus it is possible to reach the relation:

$$k \left[\mathbb{B}_V(\mathbb{F}_B; \mathbb{J}_A) - \mathbb{B}_V(\mathbb{F}_A; \mathbb{J}_B) \right] = k \left[\mathbb{B}_V(\mathbb{F}_B; \hat{\mathbb{P}}\mathbb{F}_A) - \mathbb{B}_V(\mathbb{F}_A; \hat{\mathbb{P}}\mathbb{F}_B) \right] - \left[\mathbb{B}_V(\mathbb{F}_B; \hat{\mathbb{D}}\mathbb{F}_A) - \mathbb{B}_V(\mathbb{F}_A; \hat{\mathbb{D}}\mathbb{F}_B) \right]. \quad (2.50)$$

Furthermore, one can prove

$$k \left[\mathbb{B}_V(\mathbb{F}_B; \hat{\mathbb{P}}\mathbb{F}_A) - \mathbb{B}_V(\mathbb{F}_A; \hat{\mathbb{P}}\mathbb{F}_B) \right] = 0, \quad \text{if} \quad \begin{cases} \varepsilon = \varepsilon^T; \\ \mu = \mu^T; \\ \xi = -\zeta^T. \end{cases} \quad (2.51)$$

The conditions written on the right hand side are often referred to as the reciprocity conditions. Owing to these conditions, and the equation (2.44), we can rewrite Eq. (2.52) as

$$\mathbb{B}_{\partial\nu}(\mathbb{F}_B; \mathbb{F}_A) = \mathbb{B}_V(\mathbb{F}_B; \mathbb{J}_A) - \mathbb{B}_V(\mathbb{F}_A; \mathbb{J}_B). \quad (2.52)$$

As it is formulated above, the reciprocity equation provides two formulations of a constant quantity that is nil if the two emitting currents are inside the same closed volume. However, this equation becomes much more useful in the situation where one source is located outside V and infinitely far away. For instance, we take the example of a source A in a closed volume V . Then, we express in the same volume the field \mathbb{F}_B shaped as a plane wave that is radiated by another source B located outside V . Thus, the reciprocity equation becomes:

$$\oint_{\partial\nu} (\mathbf{E}_a \times \mathbf{H}_b - \mathbf{E}_b \times \mathbf{H}_a) \cdot d\mathbf{S} = \int_{\nu} (\mathbf{E}_b \cdot \mathbf{J}_E^a + \mathbf{H}_b \cdot \mathbf{J}_H^a) dV \neq 0. \quad (2.53)$$

In the case of an emission inside a layer containing a periodic arrangement of nano-structures, the volume of integration is the volume of a grating single unit cell. The integration of the fields over the sides of

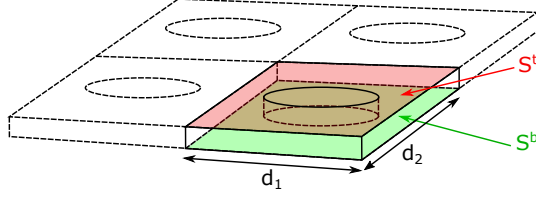


Figure 2.2: Example of a two-dimensional photonic crystal consisting of a periodic arrangement of circular holes with periods d_1 and d_2 inside an arbitrary material.

the unit cell is canceled due to the periodic boundary conditions. Thus, the surface of integration will be the top and bottom interfaces of the cell ($\partial_\nu \equiv S^t$ or S^b in Fig. 2.2).

As described by Eqs. (2.37 - 2.38), the fields \mathbb{F}_A emitted outside the structure can be expanded in Floquet-Fourier series in the top and bottom half space as:

$$\mathbf{F}_A^t = \sum_{\mathbf{K}, a} \alpha_{a, \mathbf{K}}^t \hat{\mathbf{F}}_{a, \mathbf{K}, -}^t, \quad (2.54)$$

$$\mathbf{F}_A^b = \sum_{\mathbf{K}, a} \alpha_{a, \mathbf{K}}^b \hat{\mathbf{F}}_{a, \mathbf{K}, +}^b, \quad (2.55)$$

where \mathbf{F} denotes either \mathbf{E} or \mathbf{H} .

Owing to the Lorentz reciprocity principle and the orthogonality relations in Eq. (2.46), we can calculate the coefficients $\alpha_{\mathbf{K}}$ through the equation:

$$\alpha_{a, \mathbf{K}}^{t/b} = \mathbb{B}_{\partial\nu} \left[\left(\mathbb{I}_{a, \mathbf{K}}^{t/b} \right)^R, \mathbb{F}_A^{t/b} \right]. \quad (2.56)$$

At the top interface, the field \mathbb{F}_B is written as the superposition of an incoming plane wave \mathbb{I}^t and its reflected part \mathbb{O}^t . However $\mathbb{F}_A^{t/b}$ is a purely outgoing wave and the surface integral $\mathbb{B}_{\partial\nu} \left[\left(\mathbb{O}_{a, \mathbf{K}}^t \right)^R, \mathbb{F}_A^t \right]$ is nil as expected from the Eq. (2.46). The equation (2.56) provides an efficient method to calculate the radiated field outside a structure with the sole knowledge of the field distribution at the interfaces, without knowing the profile of the source current.

Nonetheless, in the situation where the distribution \mathbb{J}_A is known the right hand side of Eq. (2.53) becomes useful:

$$\alpha_{a, \mathbf{K}}^{t/b} = \mathbb{B}_V \left[\left(\mathbb{F}_B \right)_{a, \mathbf{K}}^R, \mathbb{J}_A \right]. \quad (2.57)$$

The component $(\mathbb{F}_B)_{a,\mathbf{K}}^R$ is the part of the incoming field $\left(\mathbb{I}_{a,\mathbf{K}}^{t/b}\right)^R$ that propagates inside the structure.

Thus, we showed in this part how the reciprocity principle and the orthogonality relations Eqs. (2.45) and (2.46) provides efficient tools for the calculation of a field emitted inside a closed volume.

2.5 Resonant states

One century ago, G. Mie demonstrated that the field scattered by a sphere whose diameter is of the order of the incoming field wavelength can be written in terms of spherical harmonics. The spherical harmonics being resonant states of the studied spherical system, it leads later to the more general idea of representing the field scattered inside an arbitrary system as a superposition of its resonant states. This idea is formulated through the pole expansion approach [45].

In general, a purely propagating field contains incoming and outgoing parts, such a situation is described by Eq. (2.22) with a vanishing source term $\mathbb{J} = 0$. In this case, the homogeneous Maxwell's equations possess a discrete set of solutions for complex wavenumbers k satisfying purely outgoing boundary conditions. These solutions are the resonant states of the system obeying:

$$\hat{\mathbb{M}}(\mathbf{r}; k_n)\mathbb{F}_n(\mathbf{r}) = 0. \quad (2.58)$$

Additionally, field distributions of resonant states have to be normalized according to the following equation:

$$\mathbb{B}_V(\mathbb{F}_n^R; (k\hat{\mathbb{P}})'\mathbb{F}_n) + \mathbb{B}_{\partial V}(\mathbb{F}_n^R; \mathbb{F}'_n) = 1. \quad (2.59)$$

As explained in the previous section the first term denotes an integral over V as the volume of a unit cell and the second term denotes integrals over the top and bottom interfaces of the same unit cell, in the case of a periodic structure similar to the one depicted in Fig. 2.2. The prime refers to the derivative of the corresponding quantities with respect to k at k_n . The first derivative is carried out for the product of k_n times the material tensors contained inside V . The second derivative is applied to the analytic continuation of \mathbb{F}_n in the complex k -plane.

In a scattering geometry described by a local material change, the Maxwell's operator $\hat{\mathbb{M}}$ in Eq. (2.22) can be split into two contributions: the background operator $\hat{\mathbb{M}}_{\text{BG}} = k\hat{\mathbb{P}}_{\text{BG}} - \hat{\mathbb{D}}$, and the scattering contribution $\Delta\hat{\mathbb{M}} = k(\hat{\mathbb{P}} - \hat{\mathbb{P}}_{\text{BG}})$. In addition, the field supervector can be

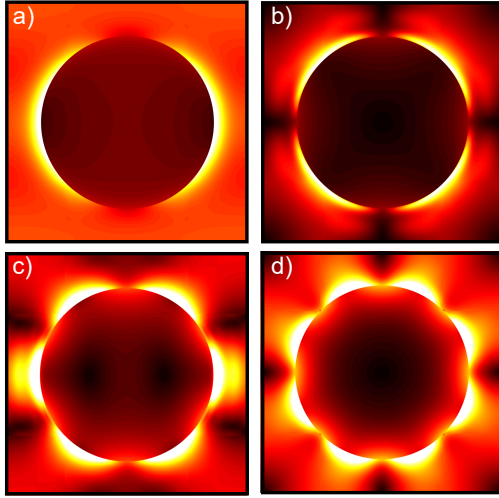


Figure 2.3: In panels (a-d) are displayed exemplary resonant modes of a nano-cylinder made of gold. We draw no detailed study of this system, hence we do not need to focus on the dimensions of the structure. In the pole expansion approach presented in this section, resonant modes are used as a basis to represent the field scattered inside the structure as written Eq. (2.64).

expressed as the superposition of a background and a scattered field as $\mathbb{F}_{\text{tot}} = \mathbb{F}_{\text{BG}} + \mathbb{F}_{\text{scat}}$. The background field fulfills:

$$\hat{\mathbb{M}}_{\text{BG}}(\mathbf{r}; k)\mathbb{F}_{\text{BG}}(\mathbf{r}; k) = 0. \quad (2.60)$$

The background field is the incoming excitation inducing the scattering inside the structure. On one hand, the background field propagates through the system as if it was an homogeneous medium with the permittivity of the background, i.e., the permittivity of the half space where the excitation comes from. On the other hand, from Eqs. (2.22) and (2.60), we can rewrite Maxwell's equations for the scattered field as an emission problem, where the source term is proportional to the background field:

$$\hat{\mathbb{M}}(\mathbf{r}, k)\mathbb{F}_{\text{scat}}(\mathbf{r}, k) = \underbrace{-\Delta\hat{\mathbb{M}}(\mathbf{r}, k)\mathbb{F}_{\text{BG}}(\mathbf{r}, k)}_{\equiv \mathbb{J}_{\text{scat}}(\mathbf{r}, k)}. \quad (2.61)$$

In the latter equation, the second term is equivalent to a source current emitting the scattered field. Knowing the Green's dyadic $\mathbb{G}(\mathbf{r}, \mathbf{r}'; k)$ of

Eq. (2.22), we can calculate the scattered field as

$$\mathbb{F}_{\text{scat}}(\mathbf{r}; k) = \int_V dV' \hat{\mathbb{G}}(\mathbf{r}, \mathbf{r}'; k) \mathbb{J}_{\text{scat}}(\mathbf{r}'; k). \quad (2.62)$$

Based on the Mittag-Leffler theorem, the Green's dyadic can be expanded in terms of the resonant poles [44, 46, 47]:

$$\hat{\mathbb{G}}(\mathbf{r}, \mathbf{r}'; k) = \sum_n \frac{\mathbb{F}_n(\mathbf{r}) \otimes \mathbb{F}_n^{\text{R}}(\mathbf{r}')}{k - k_n}. \quad (2.63)$$

Combining Eq. (2.63) with Eqs. (2.62) and (2.61), we thus can construct the total field as

$$\mathbb{F}_{\text{tot}}(\mathbf{r}; k) = \mathbb{F}_{\text{BG}}(\mathbf{r}; k) - \underbrace{\sum_n \frac{\mathbb{F}_n(\mathbf{r})}{k - k_n} I_n(k)}_{\mathbb{F}_{\text{scat}}(\mathbf{r}, k)}, \quad (2.64)$$

$$I_n(k) = k \mathbb{B}_V \left[\mathbb{F}_n^{\text{R}}(r); \Delta \hat{\mathbb{M}}(r; k) \mathbb{F}_{\text{BG}}(r; k) \right], \quad (2.65)$$

where the block matrix $\Delta \mathbb{M}$, for a nonchiral material, contains only two tensors $\Delta \varepsilon = \varepsilon_{\text{scat}} - \varepsilon_{\text{BG}}$ and $\Delta \mu = \mu_{\text{scat}} - \mu_{\text{BG}}$. The latter tensors are k dependent 3×3 tensors describing the difference of dielectric permittivity and permeability between the background material distribution and the scatterer. Additionally, we will not consider any bi-anisotropic materials in the following chapters, thus $\Delta \zeta$ and $\Delta \xi$ are nil. The superscript R refers to the reciprocal conjugate of the electric and magnetic fields of the resonant states [48, 49]. The reciprocal conjugates are evaluated at the same resonant energies but for reciprocal boundary conditions. In this approach of the pole expansion, the scattered field inside the structure $\mathbb{F}_{\text{scat}}(\mathbf{r}, k)$ is decomposed as a superposition of the resonant modes of the system. Each resonance n contributes to the scattered field proportionally to the coefficient I_n . The latter factor is the overlap integral between the background field and the field at the resonance n . This overlap integral indicates how efficiently the mode is excited by the incoming field. In the end, the total field is the sum of the scattered field and the background field. This approach is broadly used as a semi-analytical method to solve Maxwell's equations for a given system [48–56] henceforth referred to as *Mittag-Leffler expansion of the Green's dyadic*.

This new approach is in itself a significant improvement of numerical methods. It can be implemented upon any numerical frequency solver (Fourier modal method, finite differences, finite element method). It provides an accurate description of the electromagnetic field at any energy

within an arbitrary spectral range by the only mean of very few calculations. Although, most methods fully solve Maxwell's equations at any evaluated energies, the pole expansion requires only the full wave calculation of field distributions at the resonant energies and two or three off-resonant energies. The accuracy of this method is directly related to the efficiency of the mode searcher. Finding all the resonant modes and their field distributions within the spectral range of interest is a necessary condition to obtain accurate results. This numerical scheme allows the calculation of hundreds of field distributions within a time scale of minutes that is utterly fast compared to the traditional methods. However, the necessary condition to fulfill can be difficult to satisfy in certain circumstances and prevent the accurate evaluation of a certain type of phenomenon. Rayleigh anomalies also called Wood anomalies that mark the energy at which the first diffraction orders open is not modeled within the resonant state expansion. Such features are usually denoted by very sharp finger prints in the transmission and reflectance spectra as well as the field distribution inside the structure. Thus, the field can undergo swift changes while the structure is excited at energies close to the anomaly. Driving numerical calculations with the pole expansion approach near these features often lead to large numerical errors.

Additionally, non-local optical properties of metallic nano-structures are described within the so-called *Hydrodynamic model*. This model predicts a shift of the plasmon resonances and the apparitions of so called Bennett resonances [57, 58]. To describe nonlocal phenomena, the pole expansion would require a mode solver that accounts for non-locality and can find Bennett resonances.

Nonetheless, Mittag-Leffler series expansion does not need any solver in the case where the resonant modes of a system can be calculated analytically. Eventually more complex structures can be modeled from analytic results through approaches based on perturbations applied on the geometry of analytic systems [48, 56, 59].

2.6 The Fourier modal method

2.6.1 Basic principles of the Fourier modal method

In section (2.3), we derived a description of the fields reflected and transmitted by a system of stacked periodic layers. In this section, we will discuss the propagation of electromagnetic fields inside the structure. We first have to choose a reciprocal basis in which we will decompose the permittivity and permeability tensors and the fields. Then, we will solve

Maxwell's equations for each layer separately within the chosen reciprocal space before connecting the fields of the different layers using boundary conditions.

In the case of a periodic layer, it seems logic to use the Fourier reciprocal space. Thus, owing to the Bloch theorem, fields can be decomposed in the Fourier basis as

$$F_\alpha(x^1, x^2, x^3) = \sum_{mn} F_{\alpha, mn} e^{i(K_{1,m}x^1 + K_{2,n}x^2)}. \quad (2.66)$$

Here, F_α denotes the vector components of either E_α or H_α with $\alpha \in \{1, 2, 3\}$ and m, n referring to a Fourier harmonic associated to the lattice vector \mathbf{G} as described in Eq. (2.29).

The interactions of the electric field with matter are described by the constitutive equations (2.20) which yields in the Fourier reciprocal space:

$$D_{mn}^\beta = \sum_{m'n'} \varepsilon_{mn, m'n'}^{\beta, \alpha} E_{\alpha, m'n'}, \quad (2.67)$$

where $\varepsilon_{mn, m'n'}^{\beta, \alpha}$ is the convolution tensor built out of the Fourier transformation of $\varepsilon(x^1, x^2, x^3)$ along x^1 and x^2 :

$$\varepsilon_{mn, m'n'}^{\alpha, \beta} = \frac{1}{d_1 d_2} \int_S \varepsilon(x^1, x^2, x^3) e^{-i(K_{1,m} - K_{1,m'})x^1 - i(K_{2,n} - K_{2,n'})x^2} dS. \quad (2.68)$$

In addition, we do not account for bi-anisotropic properties in this scheme, thus ξ and ζ are nil.

The same decomposition can be derived for the second constitutive equation (2.21). To be exact the summation in Eq. (2.67) has to be infinite. However, numerical derivations can only be computed for a finite number of harmonics. Let us consider an interface with a normal vector that equals the contravariant basis vector \mathbf{e}^α . This means that D^α is normal to the interface, while E_β with $\beta \neq \alpha$ gives the two tangential electric field components. The constitutive equation for D^α is as follows:

$$D^\alpha = \varepsilon^{\alpha\alpha} E_\alpha + \varepsilon^{\alpha\beta} E_\beta, \quad \alpha \neq \beta. \quad (2.69)$$

For brevity of notations, there is no sum convention over indices α in the current section, and the sum convention over β runs only over indices $\beta \neq \alpha$. For all other indices, we maintain the standard sum convention over all three components.

One method to Fourier transform the quantities of the aforementioned equation in direction \mathbf{e}_α is to use the Laurent rule expressed as

$$[D^\alpha]_\alpha = [\varepsilon^{\alpha\alpha}]_\alpha [E_\alpha]_\alpha + [\varepsilon^{\alpha\beta}]_\alpha [E_\beta]_\alpha, \quad \alpha \neq \beta, \quad (2.70)$$

where the square brackets with the subscript α denote the Fourier transformation in the direction \mathbf{e}_α . As in the publication of P. Lalanne [60], we need to draw some observations on the representation of continuous and discontinuous quantities in truncated reciprocal spaces. On one hand, we assume that the Fourier transformation of a smooth and continuous quantity does not contain high spatial-frequencies, the derivation of such quantity in a truncated Fourier space do not induce a large error if the Fourier space contains enough harmonics. On the other hand, the Fourier transformation of discontinuous quantities always include an infinite sum of harmonics with non vanishing amplitudes in the infinity, which implies that the representation of such discontinuous quantities in a truncated reciprocal space introduces an error in the derivation.

As a consequence, the Fourier transformation of D^α and E_β in a truncated Fourier space can be almost exact, while the Fourier transformation of the dielectric permittivity components and E_α will introduce a much larger error. In addition, it has been demonstrated by L. Li that the Fourier transformation of the product of two quantities with concurrent jump discontinuities cannot converge at the position of the discontinuities, even in a reciprocal space with an infinite number of harmonics [30]. Thus the Fourier transformation leading to the product $[\varepsilon^{\alpha\alpha}]_\alpha [E_\alpha]_\alpha$ has to be avoided.

To overcome the above-mentioned issues, the Fourier transformations of the material tensors have to abide by factorization rules. In the case of the Fourier modal method, such rules have been very accurately formulated by L. Li. Let us consider the same interface as above with the normal vector \mathbf{e}^α . In a first step, we express the discontinuous component of the electric field as a function of the other field components:

$$E_\alpha = (\varepsilon^{\alpha\alpha})^{-1} D^\alpha - (\varepsilon^{\alpha\alpha})^{-1} \varepsilon^{\alpha\beta} E_\beta, \quad \alpha \neq \beta. \quad (2.71)$$

In this equation, the product of the linear permittivity and the field component E^α with a concurrent jump discontinuity has been removed, so that we can Fourier transform Eq. (2.71) in the x^α direction according to Li's factorization rules also called the inverse rule. In addition, the jump discontinuities of $(\varepsilon^{\alpha\alpha})^{-1}$ and $(\varepsilon^{\alpha\alpha})^{-1} \varepsilon^{\alpha\beta}$ are smaller than the jumps of $\varepsilon^{\alpha\alpha}$ and $\varepsilon^{\alpha\beta}$, thus the error introduced by $\left[(\varepsilon^{\alpha\alpha})^{-1} \right]$ and $\left[(\varepsilon^{\alpha\alpha})^{-1} \varepsilon^{\alpha\beta} \right]$ is smaller than the error of the truncated Fourier transform $[\varepsilon^{\alpha\alpha}]$ and $[\varepsilon^{\alpha\beta}]$. Finally, assuming that the Fourier transformation of the continuous functions D^α and E_β is almost exact, the main error in Eq. (2.71) is introduced only by the truncation of $(\varepsilon^{\alpha\alpha})^{-1}$ and $(\varepsilon^{\alpha\alpha})^{-1} \varepsilon^{\alpha\beta}$ which cannot be avoided and correspond to the error inherent to the truncation of the Fourier transformation of the discontinuous function E_α .

Let us denote this Fourier transformation by square brackets with subscript α and reorganize the terms in order to obtain the Fourier transform of the electric displacement:

$$[D^\alpha]_\alpha = [(\varepsilon^{\alpha\alpha})^{-1}]_\alpha^{-1} ([E_\alpha]_\alpha + [(\varepsilon^{\alpha\alpha})^{-1} \varepsilon^{\alpha\beta}]_\alpha [E_\beta]_\alpha). \quad (2.72)$$

This simple derivation provides the accurate Fourier transformation of D^α for \mathbf{e}^α being normal to the interface.

The Fourier transformation of the other two components D^β in direction x^α can be found by substituting E_α in the constitutive equation for D^β by Eq. (2.71). Following the notation of Li [4], we can summarize the two steps described above by defining an operator l_τ^+ and its inverse l_τ^- , with

$$B \equiv l_\tau^\pm A, \quad B^{\rho\sigma} = \begin{cases} (A^{\tau\tau})^{-1}, & \rho = \tau, \sigma = \tau; \\ (A^{\tau\tau})^{-1} A^{\tau\sigma}, & \rho = \tau, \sigma \neq \tau; \\ A^{\rho\tau} (A^{\tau\tau})^{-1}, & \rho \neq \tau, \sigma = \tau; \\ A^{\rho\sigma} \pm A^{\rho\tau} (A^{\tau\tau})^{-1} A^{\tau\sigma}, & \rho \neq \tau, \sigma \neq \tau. \end{cases} \quad (2.73)$$

Thus, the correct application of the Fourier factorization rules to the permittivity tensor yields

$$\tilde{\varepsilon} = l_2^+ F_2 l_2^- l_1^+ F_1 l_1^- \varepsilon, \quad (2.74)$$

where F_τ is the Fourier transformation in the direction τ .

Such formulation provides an accurate Fourier transformation of the material tensors, and allows the convergence of the field toward correct values at the position of interfaces.

While factorization rules allow to accurately describing products of functions with concurrent jump discontinuities in a finite Fourier space, they cannot overcome the Gibbs phenomenon in general. In particular, the Fourier expansion of functions with discontinuities exhibits over- and undershoots at the discontinuity that are at least 18% of the jump height. This means that the size of the finite Fourier basis in the Fourier modal method needs to be large in order to achieve a convincing convergence behavior in the case that the index contrast in the dielectric function is large. This occurs, e.g., at interfaces between semiconductors and air, as well as at interfaces between dielectrics and metals. Therefore, G. Granet developed a new formulation of the Fourier modal method [31], in which he implemented coordinate transformations such that the spatial resolution near material interfaces is increased. The implementation of this adaptive spatial resolution requires replacing the original permittivity tensor by a redefined tensor that contains the discontinuous dielectric function times

the metric components of the coordinate transformation. Thus, the influence of the Gibbs phenomenon is drastically reduced, because the metric components are close to zero near the jump discontinuities, providing a smaller effective jump height in the adaptive coordinates.

However, the implementation of adaptive spatial resolution and factorization rules is only straight-forward in cases, where all material interfaces are aligned along the directions of periodicity [61, 62]. The application of factorization rules in layers with complex cross sections requires finding at least a decomposition of the fields into normal and tangential components [63, 64]. In the covariant formulation of Maxwell's equations, normal and tangential field components are directly provided by the contra- and covariant field components in the case that all material interfaces are aligned along surfaces of constant coordinates [32]. This requires finding matched coordinate systems that are adapted to the geometry of interest, which can be easily combined with adaptive spatial resolution in order to achieve a fast convergence behavior even for metallo-dielectric systems [32, 65, 66]. An example of coordinates with adaptive spatial resolution matching a circular geometry can be seen in Fig. 2.4.

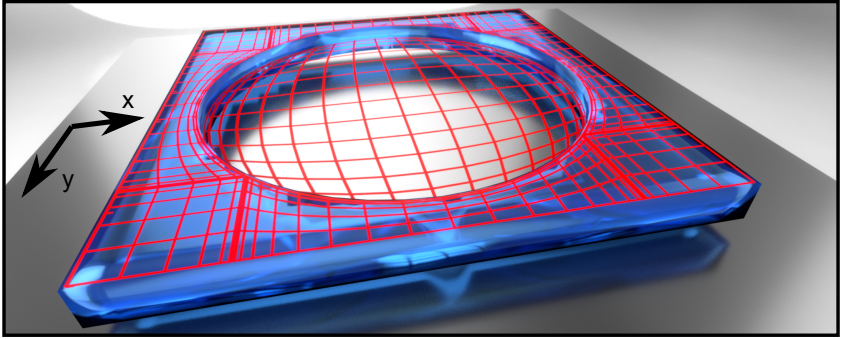


Figure 2.4: Example of a structure described within the corresponding matched coordinates displayed in Fig. 2.1. Note that the matched coordinates include the material interfaces as surfaces of constant coordinates with an increased spatial resolution in their vicinity. The coordinate transformation is included in the numerical calculations in the form of redefined permittivity and permeability.

The transformation of the material tensors and fields from uniform to nonuniform coordinates is described in the definition of electromagnetic quantities with general coordinates cf. Eqs. (2.8-2.10).

Let us solve Maxwell's equation in an arbitrary layer of the structure. By eliminating the E_3 and H_3 components from Maxwell's equations, we

obtain the matrix form of the equation of propagation in the Fourier reciprocal space [4]:

$$-i\partial_3\mathcal{E}(x^3) = \tilde{M}\mathcal{E}(x^3). \quad (2.75)$$

Here, $\mathcal{E} = (E_1, E_2, H_1, H_2)^T$ denotes the supervector containing the Fourier transform of the transverse field components. The matrix operator \tilde{M} is:

$$\tilde{M} = \begin{bmatrix} -\check{\mu}^{23}K_2 - K_1\check{\varepsilon}^{31} & \check{\mu}^{23}K_1 - K_1\check{\varepsilon}^{32} \\ \check{\mu}^{13}K_2 - K_1\check{\varepsilon}^{31} & -\check{\mu}^{13}K_1 - K_2\check{\varepsilon}^{32} \\ -k_0\check{\varepsilon}^{21} - (k_0)^{-1}K_1\check{\mu}^{33}K_2 & -k_0\check{\varepsilon}^{22} + (k_0)^{-1}K_1\check{\mu}^{33}K_1 \\ k_0\check{\varepsilon}^{11} - (k_0)^{-1}K_2\check{\mu}^{33}K_2 & k_0\check{\varepsilon}^{12} + (k_0)^{-1}K_2\check{\varepsilon}^{33}K_1 \\ k_0\check{\mu}^{21} + (k_0)^{-1}K_1\check{\varepsilon}^{33}K_2 & k_0\check{\mu}^{22} - (k_0)^{-1}K_1\check{\varepsilon}^{33}K_1 \\ -k_0\check{\mu}^{11} + (k_0)^{-1}K_2\check{\varepsilon}^{33}K_2 & -k_0\check{\mu}^{12} - (k_0)^{-1}K_2\check{\varepsilon}^{33}K_1 \\ -\check{\varepsilon}^{23}K_2 - K_1\check{\mu}^{31} & \check{\varepsilon}^{23}K_1 - K_1\check{\mu}^{32} \\ \check{\varepsilon}^{33}K_2 - K_2\check{\mu}^{31} & \check{\varepsilon}^{13}K_1 - K_2\check{\mu}^{32} \end{bmatrix}, \quad (2.76)$$

where each quantity is evaluated in matched coordinates and the inverted hat denotes the tensors $\check{\varepsilon} = l_3^- \tilde{\varepsilon}$ and $\check{\mu} = l_3^- \tilde{\mu}$ [4]. Furthermore, K_1 and K_2 are diagonal matrices with diagonal elements $K_{\alpha,m}$.

Most importantly, each layer is invariant along the stacking direction \mathbf{x}^3 . Thus, M is independent of x^3 , so that we can make the ansatz $\mathcal{E}(x^3) = \mathcal{E}_m \exp(i\gamma_m x^3)$, which transforms Eq. (2.75) into the eigenvalue problem

$$\gamma_m \mathcal{E}_m = \tilde{M} \mathcal{E}_m, \quad (2.77)$$

with eigenmodes \mathcal{E}_m that can propagate or decay with propagation constant γ_m in the direction of \mathbf{x}^3 . The eigenmodes form a basis, in which we can expand arbitrary solutions of Maxwell's equations inside that layer. To each eigenmode is associated an eigenvalue and an eigenvector. The eigenvalue is the propagation constant of the corresponding mode in the direction \mathbf{x}^3 . The whole set of eigenvectors can be combined to build a matrix \mathcal{F} . Though this matrix is usually called a *material matrix*, it behaves mathematically as a base change matrix between the Fourier basis and the eigenmode basis. This matrix will be used later to fulfill the continuity equations at the interfaces between layers.

In the following, we split the full set of eigenmodes $\{\mathcal{E}_m\}$ into subsets $\{\mathcal{E}_m^\pm\}$ with eigenvalues γ_m^\pm . The superscript $+$ or $-$ denotes the sign of the real part of γ_m^\pm (i.e., forward or backward propagation along the x^3 direction) in the case that the imaginary part of γ_m^\pm vanishes. Otherwise,

$\text{sign}(\text{Im}\gamma_m^\pm) = \pm 1$ (i.e., forward or backward decay in the x^3 direction). Thus, an arbitrary field can be expanded inside a layer as

$$\mathbf{F}(x^1, x^2, x^3) = \sum_m A_m^+ \mathcal{E}_m^+(x^1, x^2) e^{i\gamma_m^+(x^3-x_+^3)} + A_m^- \mathcal{E}_m^-(x^1, x^2) e^{i\gamma_m^-(x^3-x_-^3)}, \quad (2.78)$$

where A_m^\pm is the expansion coefficient calculated at positions x_\pm^3 . The expansion coefficients A_m^\pm can be summarized as elements of supervectors \mathbf{A}_l^\pm as amplitude vectors for each layer l . The connection of the amplitude vectors at top and at the bottom of an arbitrary layer l of thickness L is given by the propagation matrix $P_l(L)$ using the eigenvalues of this layer:

$$\begin{bmatrix} \mathbf{A}_l^+(L) \\ \mathbf{A}_l^-(L) \end{bmatrix} = \underbrace{\begin{pmatrix} e^{i\Gamma_l^+ L} & 0 \\ 0 & e^{-i\Gamma_l^- L} \end{pmatrix}}_{P_l(L)} \begin{bmatrix} \mathbf{A}_l^+(0) \\ \mathbf{A}_l^-(0) \end{bmatrix}. \quad (2.79)$$

$P_l(L)$ is constituted by blocks of sub-matrices defined by the matrix exponentials of Γ_l^\pm , i.e., diagonal matrices containing the set of eigenvalues γ_m of layer l .

In this paragraph we provided the method to solve Maxwell's equations in an arbitrary layer using the correct factorization rules and matched coordinates. The downside of the application of matched coordinates is that it requires solving homogeneous and isotropic layers numerically, even though we know their analytical solutions in uniform coordinates. This additional effort is usually compensated by the fast convergence of the results in layers with high index contrast, and it can be reduced by additional means [67].

Finally, the procedure leads to the construction of the operator $\hat{\mathbb{M}}$ and the definition of an eigenvalue problem whose solution provides a set of eigenvectors that form an eigenmode basis. The projection of the Fourier harmonics on this new basis is calculated using the material matrix and then the propagation constants of the eigenmodes are calculated as the eigenvalues of the problem. Thus, we finally were able to construct the matrix P_l describing the propagation of an electromagnetic field through the layer l in which Maxwell's equations have been solved. The propagation of an electromagnetic field through a full set of layers requires the calculation of the propagation through the top and bottom interfaces separating the different layers. For this purpose we will define and use scattering matrices in the next paragraph.

2.6.2 The scattering matrix formalism

The scattering matrix approach is a general formalism that provides the relations between the incoming and outgoing fields of a system. In a modal method, this system can be an interface, a layer or a system containing several layers and interfaces. In the case of the latter, the propagation through the layers and interfaces is calculated separately, and the results are combined iteratively to obtain the scattering matrix of the multilayer. This procedure is performed in three steps [3].

In the first step, we build the propagation matrix $P_l(L)$ in layer l by solving Maxwell's equations in a chosen reciprocal space as explained in the previous section [section (2.6.1)].

In the second step, we build the transfer matrix $I_{l,l-1}$ of an interface between the layer $l-1$ and layer l using the boundary conditions of the tangential field components. Owing to the properties of the eigenvectors in the eigenmode basis, the material matrix \mathcal{F}_l is the base change matrix from the reciprocal basis to the eigenmode basis for the tangential components of the fields. According to the boundary conditions, the transverse components of the fields at the interfaces between layers are continuous. As a consequence one can write:

$$\mathcal{E}_{\mathbf{K},l} = \mathcal{F}_l \begin{pmatrix} \mathbf{A}_l^+ \\ \mathbf{A}_l^- \end{pmatrix}, \quad (2.80)$$

$$\begin{pmatrix} \mathbf{A}_l^+ \\ \mathbf{A}_l^- \end{pmatrix} = \underbrace{\mathcal{F}_l^{-1} \mathcal{F}_{l-1}}_{I_{l,l-1}} \begin{pmatrix} \mathbf{A}_{l-1}^+ \\ \mathbf{A}_{l-1}^- \end{pmatrix}. \quad (2.81)$$

Here \mathcal{F}_l and \mathcal{F}_{l-1} are the material matrices of layers l and $l-1$, respectively. The columns of these matrices are the eigenvectors of the corresponding layers. $\mathcal{E}_{\mathbf{K},l}$ is the supervector containing Floquet Fourier components of the tangential fields.

In the last step, we use an iterative procedure to combine subsequently the matrices of the interfaces between layers and the propagation inside each layer. The iteration starts with a unit scattering matrix. At each iteration, the correct scattering matrix is combined with a matrix Z that is either an interface matrix $I_{l,l-1}$ or an inverse propagation matrix $P_l(-L)$, with

$$Z \equiv \begin{pmatrix} Z^{++} & Z^{+-} \\ Z^{-+} & Z^{--} \end{pmatrix}. \quad (2.82)$$

The scattering matrix S and the transfer matrix Z are combined using the operator $*$ and result in a new scattering matrix

$$\mathbf{Z} * \mathbf{S} = \begin{bmatrix} -(W^{++})^{-1}S^{++} \\ S^{-+} - S^{--}Z^{-+} - (W^{++})^{-1}S^{++} \\ -(W^{++})^{-1}W^{+-} \\ S^{--}Z^{--} - S^{--}Z^{-+} - (W^{++})^{-1}W^{+-} \end{bmatrix}, \quad (2.83)$$

with:

$$W^{\alpha\beta} = S^{\alpha-}Z^{-\beta} - Z^{\alpha\beta}. \quad (2.84)$$

Where the superscript $-$ do not refer to the inverted quantities but to the second row or column of the block matrices as illustrated by Eq. (2.82).

Thus, the propagation of an electromagnetic field inside the structure, from a position x_l^3 to a position $x_{l'}^3$ through an arbitrary number of layer is described as [3]:

$$\underbrace{\begin{pmatrix} \mathbf{A}_{l'}^+ \\ \mathbf{A}_l^- \end{pmatrix}}_{\equiv \mathbf{A}_{l',l'}^{\text{out}}} = \underbrace{\begin{pmatrix} S_{l',l}^{++} & S_{l',l}^{+-} \\ S_{l',l}^{+-} & S_{l',l}^{--} \end{pmatrix}}_{\equiv S_{l',l}} \underbrace{\begin{pmatrix} \mathbf{A}_l^+ \\ \mathbf{A}_{l'}^- \end{pmatrix}}_{\equiv \mathbf{A}_{l',l'}^{\text{in}}}. \quad (2.85)$$

This scheme is very general and can be applied to many modal methods. For instance one can chose the Legendre or Hermite polynomials as a reciprocal basis, solve Maxwell's equations and build an eigenmode basis. Thus, the scattering matrices have to be built according to the computed eigenvalues and boundary conditions. Although the field is decomposed in the Floquet-Fourier basis outside the structure, it might be inconvenient to solve Maxwell's equations in a different reciprocal basis inside the structure. This can lead to a mismatch of the basis at the interfaces that result in spurious oscillations at the top and bottom interfaces of the structure.

Thus, in this chapter we described within a consistent formalism the calculation of the field inside and outside layered structures using the Fourier modal method, the pole expansion approach and the reciprocity principle. In the next chapter we will see an alternative formulation of the pole expansion approach, which provide an additional insight in this method.

2.7 Derivation of resonant poles within the scattering matrix formalism

Resonant frequencies of a nanophotonic system are located within the complex ω -plane. The real part of a pole frequency corresponds to the frequency of an incident wave that can excite the corresponding resonant

mode, the imaginary part of a pole frequency corresponds to half of its line-width. Let us derive how the resonant poles of a structure are related to its scattering matrix and how we find these poles in the complex plane.

We saw in the previous section how the propagation of electromagnetic waves in layered system is described using scattering matrices. Deriving and combining the scattering matrices of every layers and interfaces of a structure provides the scattering matrix of the whole structure. The latter expresses the scattered (outgoing) amplitudes in the top and bottom half-spaces as a function of the incoming amplitudes from the same regions as in Eq.(2.85). Let us rewrite the latter equation with a slightly different formalism to name explicitly the incoming and scattered amplitude vectors:

$$\begin{pmatrix} \mathbf{A}_{\text{out}}^b \\ \mathbf{A}_{\text{out}}^t \end{pmatrix} = S \begin{pmatrix} \mathbf{A}_{\text{in}}^t \\ \mathbf{A}_{\text{in}}^b \end{pmatrix}, \quad (2.86)$$

where S is the scattering matrix of an arbitrary structure, \mathbf{A}_{in} and \mathbf{A}_{out} denote the incoming and scattered amplitudes and the superscripts t and b denote the fields located in the top and bottom half spaces.

From Eq.(2.87) one can derive:

$$S^{-1} \begin{pmatrix} \mathbf{A}_{\text{out}}^b \\ \mathbf{A}_{\text{out}}^t \end{pmatrix} = \begin{pmatrix} \mathbf{A}_{\text{in}}^t \\ \mathbf{A}_{\text{in}}^b \end{pmatrix}. \quad (2.87)$$

The kernel of the operator $[S^{-1}(\omega)]$ refers to the solution of Eq.(2.87) for a right hand side equal to zero. It provides the solutions of Maxwell's equations describing a field scattered by the structure in the absence of an incoming field. Solutions of Maxwell's equations with such property correspond to resonant states of the structure. The resonant frequencies satisfying this conditions will be written ω_m .

As it has been demonstrated in the last years [45], the scattering matrix of a structure excited at the frequency ω can be written:

$$S(\omega) = S_{\text{BG}}(\omega) + \sum_{m=1}^M \frac{B_m}{\omega - \omega_m}. \quad (2.88)$$

S_{BG} denotes a smooth background contribution, and M the number of resonant poles considered in the derivation. B_m is the residue of the scattering matrix at the frequency ω_m . As a more suitable representation for the residue, we might refer to the more general formula [68, 69]:

$$S(\omega) = S_{\text{BG}}(\omega) + \sum_{m=1}^M \frac{L_m R_m}{\omega - \omega_m}, \quad (2.89)$$

2.7 Derivation of resonant poles within the scattering matrix formalism

where L_m and R_m correspond to the rank factorization of B_m . Then, the latter equation can be written using block matrices as

$$S(\omega) = S_{\text{BG}}(\omega) + L(\omega I - \Omega)^{-1}R. \quad (2.90)$$

Ω is a diagonal matrix containing the resonant frequencies ω_m , I is the identity matrix and L and R are built using L_m and R_m . Thus, the dimension of the scattering matrix should be larger than the number of resonant poles considered $\dim(S) \geq \dim(\Omega)$. Finally, one can derive the derivative of Eq.(2.90) with respect to ω :

$$S'(\omega) \approx -L(\omega I - \Omega)^{-2}R. \quad (2.91)$$

We assume that the background term is very slowly varying as a function of ω and its derivative is neglected. Then, in the case where $\dim(S) = \dim(\Omega)$ one can multiply Eq.(2.90) with the inverse of Eq.(2.91) that provides the eigenvalue equation:

$$[S'(\omega)]^{-1}S(\omega) = R^{-1}(\omega I - \Omega)R. \quad (2.92)$$

In the latter equation, another occurrence of the background term is neglected that is acceptable in the cases where ω is sufficiently close to a resonant pole so that the background contribution becomes negligible. Thus, $\omega I - \Omega$ and the column vectors of R are eigenvalues and eigenvectors respectively of $[S'(\omega)]^{-1}S(\omega)$. Thus, deriving S and S' at the guess frequency ω_0 , one can derive the eigenvalues $\omega_0 - \omega_1$ of Eq.(2.92), where ω_1 is closer to a resonant mode than ω_0 . Then, using ω_1 as the next guess value to derive S and S' one can proceed iteratively until the eigenvalue of Eq.(2.92) becomes small enough to consider that the guess value converged to the frequency of a resonance.

In a more general case where $\dim(S) > \dim(\Omega)$, assuming that S' has not full rank or at least that some singular values are close to zero, then one can derive the singular value decomposition

$$S' = U\Sigma V^\dagger. \quad (2.93)$$

Σ is the diagonal matrix containing the singular values, U and V are unitary matrices. As explained in [69], one can remove the singular values of Σ that are below a certain threshold and the corresponding columns in U and V . The resulting matrices are called U_r , Σ_r and V_r . Thus, we obtain the equation:

$$(\omega I - \Omega)\mathbf{v} = \Sigma_r^{-1}U_r^\dagger S V_r \mathbf{v}. \quad (2.94)$$

Using the same iterative procedure as for Eq.(2.91), it is possible to build a routine that converges to the resonant poles of S .

3 Mittag Leffler expansion of electromagnetic fields

The history of science shows that theories are perishable. With every new truth that is revealed we get a better understanding of Nature and our conceptions and views are modified.

Nikola Tesla (1856-1943)

3.1 A new pole expansion

3.1.1 The Mittag-Leffler expansion

In this section we will provide the derivation and assumptions behind the Mittag-Leffler expansion. This derivation is rarely given in textbooks and an interested reader needs the following details to understand the more general scheme behind the pole expansion. Within this picture we will see that the Green's dyadic is not the only quantity that can be expanded in Mittag-Leffler series. Thus, we will study the requirements under which one might build the series expansion of arbitrary physical quantities, the bias and challenges behind such mathematics.

A thorough description of the Mittag-Leffler expansion is based on few mathematical theorems from complex analysis that I will remind shortly. Consider U a subset of the complex plane \mathbb{C} , D is a compact subspace of U simply connected and γ the positively oriented curve enclosing D .

Theorem 3.1: Residue theorem. —

Let $f(\xi)$ be analytic in $(D \setminus \{w_1, w_2, \dots, w_n\})$, where D contains the singular points w_i . Then,

$$\frac{1}{2i\pi} \int_{\gamma} f(w)dw = \sum_{i=1}^n \text{Res}(f, w_i). \quad (3.1)$$

Using the generalized Cauchy integral formula it is possible to calculate the Laurent coefficient of a function f at a pole of order n higher than one, a textbook would provide the following formula:

$$LC(f, z_0) = \lim_{z \rightarrow z_0} \left\{ \frac{d^{n-1}}{dz^{n-1}} [(z - z_0)^n f(z)] \frac{1}{(n-1)!} \right\}. \quad (3.2)$$

Theorem 3.2: Mittag-Leffler theorem (1876). —

Let $\{a_n\}_{n=1}^{\infty}$ be a sequence of distinct complex numbers, $|a_1| < |a_2| < \dots$ with $\lim_{n \rightarrow \infty} |a_n| = \infty$. Let $g_n(z)$ be a sequence of rational functions of the form:

$$g_n(z) = \sum_{k=1}^{l_n} \frac{c_{nk}}{(z - a_n)^k}, \quad (3.3)$$

where l_n is a finite entire number and a_n is the unique pole of the corresponding function $g_n(z)$. Then there are meromorphic functions $f(z)$ in the complex z plane \mathbb{C} having poles at a_n , and only there, with given principal parts $g_n(z)$ of the Laurent series corresponding to the points a_n

3 Mittag Leffler expansion of electromagnetic fields

and the associated Laurent coefficient c_{nk} . All these functions $f(z)$ are representable in the form of a Mittag-Leffler expansion

$$f(z) = h_m(z) + \sum_{n=1}^{\infty} [g_n(z) + p_n(z)], \quad (3.4)$$

where $p_n(z)$ is a polynomial chosen in dependence of a_n and $g_n(z)$ so that the series expansion is uniformly convergent on any compact set $D \subset \mathbb{C}$ and $h_m(z)$ is an arbitrary function analytic in \mathbb{C} .

Few versions of this theorem have been formulated by Mittag-Leffler through the years, thus the year of the theorem mentioned above has been indicated.

The formulation of the Mittag-Leffler theorem can be rather disturbing, it is an existence theorem and hence the logic of its statement is inverted. The content can be summed-up into two points:

- for an arbitrary set of points in the complex plane $\{a_n\}_{n=1}^{\infty}$, we can build functions that admit these points as poles
- the latter functions can be expanded in Mittag-Leffler series, which will have the form of Eq. (3.4).

Though the first statement is not of much interest in this study, the second statement is the core of the following demonstration.

Consider a holomorphic function f on $(D \setminus \{a_1, a_2, \dots, a_n\})$, containing the simple poles $\{a_1, a_2, \dots, a_n\}$ associated to the corresponding residues $\{b_1, b_2, \dots, b_n\}$. According to the Mittag-Leffler theorem this function can be expressed as

$$f(z) = h_m(z) + \sum_{n=1}^{\infty} \left[\frac{b_n}{z - a_n} + p_n(z) \right], \quad (3.5)$$

where the complex values b_n are the residues of f at each pole a_n . To build the series expansion of f , $P_n(z)$ and $h_m(z)$ have to be expressed relatively to $1/(z - a_n)$ such that the sum in Eq. (3.5) converges.

Let us build the function $h_m(z)$ and the polynomial $P_n(z)$ for a function with simple poles. Choose a sequence of circles C_n of radius R_n centered around the origin such that the contour does not pass through the singular points and $f(z)$ is bounded on C_n . The radius R_n grows toward infinity as $n \rightarrow \infty$. Then let us integrate around C_n the equality:

$$\frac{f(z)}{z - x} = f(z) \left[\left(\frac{x}{z}\right)^m \frac{1}{z - x} + \sum_{p=0}^{m-1} \frac{x^p}{z^{p+1}} \right]. \quad (3.6)$$

The integral of the latter equation along the circle C_n is be calculated with the residue theorem. The integral of the left side of Eq. (3.6) along C_n yields

$$\frac{1}{2i\pi} \int_{C_n} \frac{f(z)}{z-x} dz = \sum_{r=1}^n \frac{b_r}{a_r-x} + f(x). \quad (3.7)$$

The right side of Eq. (3.6) carry the factor $f(z)(x/z)^m$ that has a pole of order m in $z = 0$. Thus, the Laurent coefficient of f at this pole is calculated with Eq. (3.2) and the integral of the right side of Eq. (3.6) follows:

$$\frac{1}{2i\pi} \int_{C_n} \frac{f(z)}{z-x} dz = \sum_{p=0}^{m-1} \left\{ \frac{x^p}{2i\pi} \left[\frac{1}{p!} \frac{d^p f(z)}{dz^p} \Big|_{z=0} + \sum_{r=1}^n \frac{b_r}{a_r^{p+1}} \right] \right\} \quad (3.8)$$

$$+ \frac{x^n}{2i\pi} \int_{C_n} \frac{f(z)}{z^n(z-x)} dz. \quad (3.9)$$

According to the Mittag-Leffler theorem, as the radius of integration R_n increases, the last term of the above equation should converge to zero:

$$\lim_{n \rightarrow \infty} \left(\frac{x^n}{2i\pi} \int_{C_n} \frac{f(z)}{z^n(z-x)} dz \right) = 0. \quad (3.10)$$

Thus, using Eq. (3.7) and Eq. (3.8) we prove that a complex function $f(z)$ that is analytic except for a countable number of poles a_n with residues b_n and that obeys the asymptotic behavior $\lim_{z \rightarrow \infty} f(z)/z^p = 0$ can be expanded as

$$f(z) = \sum_{m=0}^{p-1} z^m \left[\frac{f^{(m)}(0)}{m!} + \sum_n \frac{b_n}{a_n^{m+1}} \right] + \sum_n \frac{b_n}{(z-a_n)}, \quad (3.11)$$

where $f^{(m)}(0)$ denotes the m^{th} order derivative of f at $z = 0$. Other

3 Mittag-Leffler expansion of electromagnetic fields

formulations of the p^{th} order Mittag-Leffler expansion are [70]

$$f(z) = \underbrace{\sum_{m=0}^{p-1} z^m \frac{f^{(m)}(0)}{m!}}_{h_m(z)} + \sum_n \left[\frac{b_n}{(z - a_n)} \frac{z^p}{a_n^{p+1}} \right], \quad (3.12)$$

$$f(z) = \underbrace{\sum_{m=0}^{p-1} z^m \frac{f^{(m)}(0)}{m!}}_{h_m(z)} + \sum_n \left[\frac{b_n}{(z - a_n)} + \underbrace{\sum_{m=0}^{p-1} \frac{z^m b_n}{a_n^{m+1}}}_{P_n(z)} \right]. \quad (3.13)$$

For instance, the zeroth-order Mittag-Leffler expansion yields

$$f(z) = \sum_n \frac{b_n}{(z - a_n)}, \quad (3.14)$$

while we obtain for the first-order Mittag-Leffler expansion:

$$f(z) = f(0) + \sum_n \frac{b_n}{(z - a_n)} \frac{z}{a_n} = f(0) + \sum_n b_n \left(\frac{1}{a_n} + \frac{1}{z - a_n} \right). \quad (3.15)$$

In both cases, a rather simple pole contribution as a sum over $b_n/(z - a_n)$ arises, with a nontrivial background $h_m = f(0)$ and a polynomial $p_n = \sum_n b_n/a_n$ for the first-order Mittag-Leffler expansion. That means that for any order p , we obtain a pole contribution of the form $\sum_n b_n/(z - a_n)$, accompanied by a polynomial of order $p - 1$ and $p - 1$ background terms. According to Eq. (3.10), if the p^{th} order Mittag-Leffler expansion is applicable, an expansion of order p' with $p' > p$ is possible, too. From the uniqueness of the Mittag-Leffler expansion, we infer the sum relations of the form

$$\sum_n \frac{b_n}{a_n^{m+1}} = -\frac{f^{(m)}(0)}{m!}, \quad (3.16)$$

which holds for any order m larger than p .

In principle, the sum relations in Eq. (3.11) can be used in order to estimate the accuracy of a series expansion using only a finite set of poles. In the same context, it should be noted that a finite number of poles in the expansion results in an error that can be compensated locally by a polynomial correction. Indeed assuming that $f(z)$ can be calculated with both, a time consuming but exact method and an incomplete pole expansion, it is possible to calculate an error correction for the pole expansion at

few position z . Thus, the error correction can be interpolated and added to the pole expansion as a background term. This procedure is a fit of a correction term between the exact value of $f(z)$ and its pole expansion. It has a very low numerical cost that is of high interest to calculate solutions of Maxwell's equations inside resonant systems. In the end, it is possible to use a higher order expansion without analytically deriving the background terms that are fitted during the error correction. In this situation, the fit procedure will return an error correction containing both background terms and eventually the contribution of distant poles that were not considered during the expansion. In that case, the background and the distant pole's contributions are fitted at once and thus they are not distinguishable anymore.

3.1.2 General formulation

In the pole expansion of the Green's dyadic described in Chapter 2, the field inside the structure is split in background and scattered parts. The background field is equal to the incoming plane wave propagating through the structure as if it was a medium with the same refractive index as the upper or lower half space where the plane wave comes from. The scattered field is calculated multiplying the Mittag-Leffler expansion of Green's dyadic with the term $\Delta\hat{\mathcal{M}}$ and the background field. Then it is summed to the background contribution, to retrieve the total internal field. However, the Mittag-Leffler theorem can be used for the expansion of other quantities than the Green's dyadic, such as optical scattering matrices [45]. In this chapter, we will focus on the Mittag-Leffler expansion of the whole total field inside a structure, without distinction between background and scattered fields. In the case that the background field is free of poles, according to Eq. (3.11) the p^{th} -order Mittag-Leffler expansion of the total field yields

$$\mathbb{F}_{\text{tot}}(\mathbf{r}; k) = \sum_{m=0}^{p-1} \left[\frac{1}{m!} \frac{\partial \mathbb{F}_{\text{tot}}}{\partial k^m}(\mathbf{r}; 0) + \sum_n \frac{\mathbb{F}_n(\mathbf{r})}{k_n^{m+1}} I_n(k_n) \right] k^m + \sum_n \frac{\mathbb{F}_n(\mathbf{r})}{(k-k_n)} I_n(k_n), \quad (3.17)$$

where

$$I_n(k) = k\mathbb{B}_V \left[\mathbb{F}_n^{\mathbf{R}}(\mathbf{r}); \Delta\hat{\mathcal{M}}(\mathbf{r}; k)\mathbb{F}_{\text{BG}}(\mathbf{r}; k) \right]. \quad (3.18)$$

Though in the Green's dyadic expansion Eq (2.63) the overlap integral expressed Eq. (2.65) has to be calculated at every wavenumber k , the Mittag-Leffler expansion of the total fields requires only the calculation of the overlap integral at the wavenumbers k_n of the resonant modes. Thus,

the calculation of the field expansion is faster and does not account for a background field explicitly. However, "background like" constant terms arise for the series expansion of the total field at orders higher than 0. In the end, the higher is the order of the expansion, the more complex is the term $h_m(z)$ whose components draw a picture more and more accurate of the function.

In the last years the same simplification has been developed for the Mittag-Leffler expansion of optical scattering matrices. The first step has been the formulation of a series expansion of scattering matrices with k -dependent overlap integrals [71]. Then, another form of this pole expansion arose based on k -independent overlap integrals [45]. Nonetheless, this simplification often leads to the calculation of more complex background terms.

Only the field inside the structure can be rigorously decomposed over the basis of resonant poles since resonance field-distributions exponentially grow in the exterior of the system. However, methods have been developed to regularize the resonant fields outside the structure [72]. Other methods based on the calculation of the scattering matrix coefficient provide the pole expansion of the reflected and transmitted fields [45]. Finally, using the orthogonality relations given by Eqs. (2.45) and (2.46) in addition to the reciprocity principle expressed in Eq. (2.56), one can calculate the transmitted and reflected fields from the internal field at the top and bottom interfaces. This method will be used in the following numerical example to compute the complete near field inside and outside nanostructures.

3.2 Numerical results

3.2.1 Dielectric slab

The first example is a planar isotropic and homogeneous dielectric slab of thickness h . In this structure, most of the optical properties can be evaluated analytically that will allow a rigorous calculation of relative errors. Let us assume a plane wave incoming from the top half space above the slab with normal incidence. The incoming electric field is parallel to the top interface of the dielectric with an arbitrary azimuthal direction. We choose a coordinate system with the axis \mathbf{x} aligned along the direction of the incoming electric field $\mathbf{E}_{\text{tot}} = E_{\text{tot}} \mathbf{x}$. The reflection and the transmission Fresnel coefficients ρ and τ , between a surrounding medium of refractive index n_1 and the dielectric material of refractive index n_2 are

at normal incidence:

$$\rho = (n_1 - n_2)/(n_1 + n_2), \quad (3.19)$$

$$\tau = 2n_1/(n_1 + n_2). \quad (3.20)$$

The origin of the coordinate system is centered inside the dielectric slab such that the refractive index is n_2 for $z \in [-h/2, h/2]$ and n_1 otherwise. Few analytic derivations lead to the expression of fields inside and outside the structure:

$$E_{\text{tot}}(z; k) = \begin{cases} \left(e^{ikn_1(z+h/2)} - r(k)e^{-ikn_1(z+h/2)} \right) e^{i\phi} E_0 \equiv E_{\text{top}}, & (3.21a) \\ \tau \frac{e^{ikn_2(z-h/2)} - \rho e^{-ikn_2(z-3h/2)}}{1 - (\rho^2 e^{2ikn_2h})} e^{i\phi} E_0 \equiv E_{\text{int}}, & (3.21b) \\ t(k)e^{ikn_1(z-h/2)} e^{i\phi} E_0 \equiv E_{\text{bot}}, & (3.21c) \end{cases}$$

where E_{top} , E_{int} and E_{bot} are defined on the intervals: $z \leq -h/2$; $z \in [-h/2, h/2]$ and $z \geq h/2$, respectively. E_0 is the amplitude of the incidence plane wave and ϕ is the phase of the incoming electric field at the top interface of the slab. The coefficients r and t are the reflectance and transmittance of the dielectric slab:

$$r = \rho(e^{2in_2kh} - 1)/(1 - \rho^2 e^{2in_2kh}), \quad (3.22)$$

$$t = \tau \frac{n_2}{n_1} e^{ikn_2h} / (1 - \rho^2 e^{2in_2kh}). \quad (3.23)$$

From the poles of the field defined in Eq. (3.21b), we can derive the wave number and field distribution of the resonant states inside the slab as:

$$k_n = \frac{n\pi + i \ln(|\rho|)}{2h}, \quad n \in Z, \quad (3.24)$$

$$E_n(z; k_n) = \frac{(-i)^n}{2n_2\sqrt{h}} [e^{ik_n n_2 z} + (-1)^n e^{-ik_n n_2 z}]. \quad (3.25)$$

For the Mittag-Leffler expansion of the total field, we need to investigate the asymptotic behavior of the field inside the slab. We need to distinguish two cases:

$$\lim_{k \rightarrow \infty} |E_{x,\text{tot}}(z; k)| = \begin{cases} \frac{2n_1}{|n_1 - n_2|}, & \text{for } z = z_{\text{top}}; & (3.26a) \\ 0, & \text{otherwise.} & (3.26b) \end{cases}$$

The total field converges to a constant value at the position of the top interface, so that we have to use a first-order Mittag-Leffler expansion. The

3 Mittag Leffler expansion of electromagnetic fields

total field inside the structure is calculated using Eq. (3.17) and $E_{\text{tot}}(z; k = 0) = 1$, thus the overlap integral yields:

$$I_n(k) = \frac{(-i)^n i k \Delta \varepsilon \sqrt{h}}{2n_2} e^{ikn_1 h/2} \left\{ \text{sinc} \left[\frac{h}{2} (k_n n_2 + k n_1) \right] + (-1)^n \text{sinc} \left[\frac{h}{2} (k_n n_2 - k n_1) \right] \right\}. \quad (3.27)$$

In the case of the pole expansion of the total field, $k = k_n$, and the overlap integral can be further simplified as

$$I_n(k_n) = \frac{(i)^n \tau}{2i\sqrt{h}} e^{ikn_1 h/2}. \quad (3.28)$$

In addition, assuming

$$E^{\text{BG}}(z; k) = \exp[ikn_1(z + h/2)], \quad (3.29)$$

we can combine Eq (3.27) with Eq. (2.64) to calculate the total field using the Mittag-Leffler expansion of the Green's dyadic.

3.2.2 Convergence of pole expansion approaches

Let us illustrate the analytic results derived in the previous paragraphs. Consider a slab 1 μm thick, made of GaAs ($n_2 = 3.5$) and surrounded by air illustrated in Fig. 3.1. The incoming plane wave has a normal incidence with a wave vector oriented along z as displayed in the top right corner of the picture. The excited modes of this structure are the Fabry Perot modes corresponding to the maximum of transmittance in the spectra in Fig. 3.1. According to Eq. (3.24), these modes occur at energies with the rounded value $177.1n - 33.1i$ meV where n is an integer number. The Fabry Perot resonances own identical imaginary parts represented by red crosses in the complex plane illustrated in the lower panel of Fig. 3.1. Identical imaginary parts denote modes of the same linewidth as it can be observed in the spectra. The profiles of the first four Fabry Perot modes are illustrated on the edge of the slab in the same figure.

A map of the electric field induced inside and outside the slab by a top incoming plane wave is calculated analytically and displayed Fig. 3.2 in the panel (a). The ordinates axis denotes the position along z in the slab, while the abscissa refers to the energy in meV. The top and bottom interfaces of the dielectric slab are marked with two horizontal black dashed lines. The red dashed line indicates at which energy is calculated the field in the panels below, which is 650 meV.

In Panel (b) is displayed the electric field inside the slab calculated with the zeroth-order pole expansion of the field, the first order pole expansion

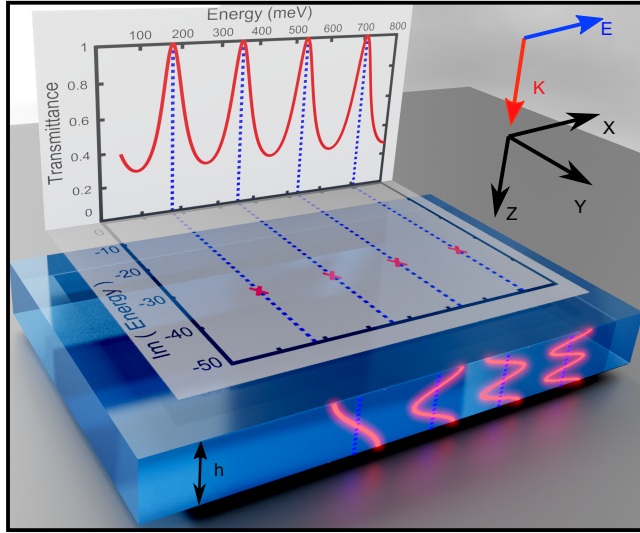


Figure 3.1: Schematic of homogeneous slab. The top panel displays transmittance spectra for a GaAs slab of thickness $h = 1 \mu\text{m}$ and a refractive index of 3.5 in air at normal incidence. Below the spectra, we depict the complex energy plane, with each resonant state corresponding to a pole marked by a red cross.

of the field and the Green's dyadic pole expansion, respectively, from right to left. The pole expansion of the field displayed in each row is calculated with an increasing number of poles from top to bottom. For each Mittag-Leffler expansion, we account for poles whose energy real part can be positive, nil or negative. Since the poles are located symmetrically around the imaginary axis of the complex plane with identical imaginary parts, we consider one resonant energy with negative real part for each resonant energy with a positive real part. In addition we account for a pole with a real part equal to zero. Thus, in each row, taking into account 9, 17 and 33 poles correspond to the calculation of 4, 8 and 16 poles with a positive real energy and in addition, the same number of virtual poles owning a negative real energy and one pole with nil real energy.

Owing to the asymptotic behavior of the electric field at the top interface expressed in Eq. (3.26a) and Eq. (3.26b), the field expansion at this position requires a Mittag-Leffler expansion of order one or higher. As a consequence, we observe in Fig. 3.2 (b) that the result computed using the zeroth-order field expansion is incorrect at the top interface. Moreover, even though we increase the number of poles in the calculations displayed

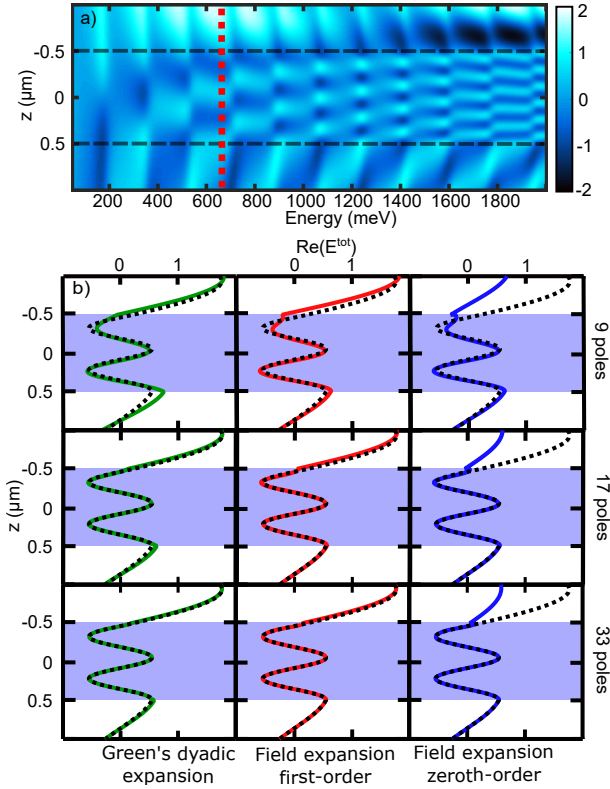


Figure 3.2: (a) Real part of the electric field displayed inside the dielectric slab (from -0.5 to $0.5 \mu\text{m}$) and outside, for a top incoming plane wave at normal incidence. (b) Real part of the electric field displayed as a function of the z coordinate at an energy of 650 meV [denoted by the red dashed line in panel (a)]. In each panel, the analytic result is displayed as a black dashed line. From top to bottom, the number of physical poles in each expansion is 9, 17 and, 33. In the columns, the pole expansion of the field has been calculated using the Mittag-Leffler expansion of the Green's dyadic (left) as well as the first (middle) and zeroth-order (right) expansion of the total field.

in the lower part of the figure, the zeroth-order field expansion does not converge to the right value at the top interface. The error manifests itself through spurious field oscillations along z . The amplitude of the oscillation increases while getting closer to the top and bottom interfaces. In addition, the frequency of these oscillations appears to be the energy of the pole chosen for the truncation of the expansion. We will investigate these spurious oscillations in the next figure panel (b).

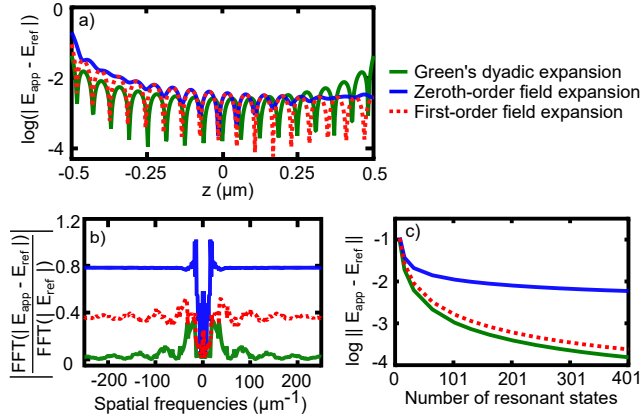


Figure 3.3: (a) Absolute error of the electric field in logarithmic scale when using 33 resonant states as basis for zeroth (red dashed line) and first-order (blue solid line) expansion of the field as well as the expansion of the Green's dyadic (green solid line). (b) Normalized Fourier transform of the absolute error of electric fields in dependence of the spatial frequencies. The relative error for the higher frequency components becomes dominant except for the approach based on the expansion of the Green's dyadic. (c) Evolution of the L^2 error as a function of the number of resonant states used for each of the three methods.

In Fig. (3.3), we produce a detailed analysis of the analytic error owned by each method at an energy of 650 meV. In panel (a) is displayed the logarithm of the absolute error of the field, calculated as a function of the position z . We observe that the error pattern exhibited by the Mittag-Leffler expansion of the field is asymmetric, as discussed, the reason is that the asymptotic behavior of the field inside the structure is asymmetric and so is the derived error. A similar calculation in the case of a dielectric slab excited from top and bottom half spaces with same incidence and characteristics would provide a symmetric asymptotic behavior at the top and bottom interfaces. Consequently, the field expansion in such situations would lead to an almost symmetric error pattern. The asymptotic behavior

of the Green's dyadic does not suffer from such asymmetry and the error exhibited by the corresponding calculation is less asymmetric, yet, not completely symmetric neither, due to the fact that the total field itself is not symmetric at 650 meV.

The panel (b) in Fig. (3.3) displays the Fourier transformation of the absolute error divided by the Fourier transform of the analytic result. Thus, the panel displays a relative error of the field in Fourier space, which seems relevant considering the spurious oscillation observed in Fig. 3.2. The relative error grows until a cut off frequency is reached. It appears that it is the frequency of the truncation pole, i.e., the pole of higher energy considered in the pole expansion. In addition, this energy corresponds to the frequency of the spurious oscillations observed earlier. It seems rather logic to assume that the spatial resolution of the field in the z direction is limited by the inverse of the frequency of the pole of higher energy considered for the expansion. This holds in the situation where we do not fit any background contribution. In the situation of a fitted background, the fit procedure will also take into account the contribution of distant poles in the spectra and the limitation over the spatial resolution will be lifted. Finally, the presence of pure background terms reduces the amplitude of the spurious oscillations without completely suppressing them. Indeed, the spurious oscillations do not hamper so heavily the higher-order field expansions or the series expansion of the Green's dyadic. This behavior has a mathematics origin. In Eq. (3.12) one can observe for a fixed position z close to a pole a_n in the complex plane that the higher is the order of the expansion p the lower is the contribution of the pole. This phenomenon is balanced by the occurrence of more and more background terms in the function $h_m(z)$. While the calculation of the Mittag-Leffler expansion always assumes a small error due to the finite number of poles, the evaluation of the background term requires exact values. Thus, the higher is the order of the pole expansion the closer we are from an analytic or fitted calculation of the expanded function. Though the error of the result computed with field expansion stabilizes to a constant value at higher frequencies in panel (b), the relative error of the result from the Green's dyadic expansion decreases for higher frequencies. The background term of the Green's dyadic expansion is a sinusoidal function, thus it carries more information than the background term of the field expansion that is just 1. The latter argument could be a reason why the Green's dyadic expansion is more accurate.

In panel (c) we integrate the absolute error of each method over the thickness of the dielectric slab to obtain an overall L^2 error for each method

as a function of the number of considered poles. The L^2 error is defined as

$$\|f_{\text{approx}} - f_{\text{ref}}\|^2 = \int dz |f_{\text{approx}}(z) - f_{\text{ref}}(z)|^2 \quad (3.30)$$

The L^2 error is higher for the field expansion than for the Green's dyadic series expansion. The zeroth-order field expansion does not converge to a low error due to the incorrect field calculation at the top interface that does not vanish. Thus, the Mittag-Leffler expansion of the Green's dyadic has the fastest convergence pattern even though the first order field expansion exhibit an error of the same order, accounting for the same number of poles.

3.2.3 Reflectance and transmittance expansion

It is relevant to emphasize that the previous derivations can be extended and prove to be fully consistent with the models developed in a broader context for the calculation of the transmittance and reflection based on the series expansion of scattering matrices [45]. In the previous paragraph we have derived the total field inside and outside a dielectric slab, thus owing to the reciprocity principle Eq. (2.56), we can express the reflection and transmittance of the dielectric slab as

$$r = \alpha_{s,0}^t = \mathbb{B}_{\partial\nu} [\mathbb{I}_{a,0}^t(\mathbf{r}; k); \mathbb{F}_{\text{tot}}^t(\mathbf{r}; k)], \quad (3.31)$$

$$t = \alpha_{s,0}^b = \mathbb{B}_{\partial\nu} [\mathbb{I}_{a,0}^b(\mathbf{r}; k); \mathbb{F}_{\text{tot}}^b(\mathbf{r}; k)], \quad (3.32)$$

where $\mathbb{F}_{\text{tot}}^{t/b}$ is the value of the total field derived with Eq. (3.17) at the top and bottom interfaces. a denotes the polarization, and 0 refers to the zeroth diffraction order considered for a normal incidence.

To ensure unitary orthogonality relations in the form of Eqs. (2.45) and (2.46) at normal incidence in a surrounding material with an optical index $n_1 = 1$, the super vectors $\mathbb{I}^{t/b}(r; k)$ have to be normalized with the constant $N^{t/b} = \sqrt{i/2}$. Then the equations (2.56), (3.17), (3.25) and (3.28) lead to the first-order Mittag-Leffler expansion of r and t

$$r = \frac{in_1(1+n_1)}{h(n_1^2 - n_2^2)} \sum_n \left(\frac{1}{k_n} + \frac{1}{k - k_n} \right), \quad (3.33)$$

$$t = \frac{i(-1)^n n_1(1+n_1)}{h(n_1^2 - n_2^2)} \sum_n \left(\frac{1}{k - k_n} \right). \quad (3.34)$$

These expressions exhibits residues rigorously equal to the residues obtained in the Mittag-Leffler expansion of scattering matrices [45].

3 Mittag Leffler expansion of electromagnetic fields

For instance let us pursue the calculation of the latter numerical example. We assume a 1 μm thick dielectric slab of refractive index $n_2 = 2.5$ under normal incidence in a surrounding material of index $n_1 = 1$.

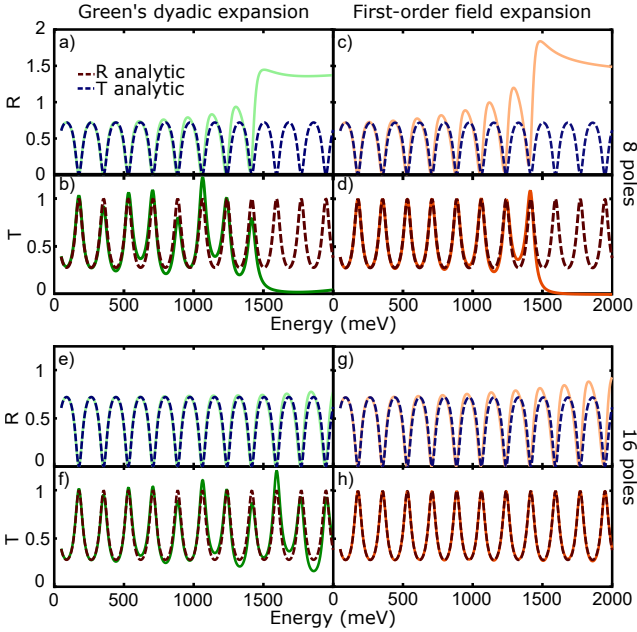


Figure 3.4: Transmittance and reflection of a dielectric slab calculated using the reciprocity principle on the fields Fig. 3.2 that has been obtained whether with the Mittag-Leffler expansion of the Green's dyadic (a,b) or the expansion of the total field (c,d). The reciprocity principle has been applied on the different pole expansion for different truncation order, 8 poles with positive real parts in the first row and 16 in the second row.

The transmittance and reflection of the structure have been computed applying the reciprocity principle to the internal fields calculated with the k -dependent and -independent series expansions. In Fig (3.4), the coefficients in the left and right columns have been calculated using the Green's dyadic Mittag-Leffler expansion and the field first-order expansion, respectively. The results have been calculated with 17 and 33 poles in the top and bottom rows. In figures 3.2 and 3.3, we studied the convergence of the field at a fixed energy for an increasing number of poles. In Fig. 3.4, it becomes obvious that the energy range of the calculations is also limited by the number of poles considered. It has been shown in Fig 3.3 that even though the expansion of the Green's dyadic provides the best overall

accuracy, the field expansion at the bottom interface provides locally the best result. Thus, on one hand the transmittance calculated applying the reciprocity principle to the field expansion at the bottom interface is more accurate than the result obtained with the Green's dyadic expansion. On the other hand, the Green's dyadic expansion provides better results for the calculation of the reflection coefficients. Since the zeroth-order field expansion provides an incorrect value of the electric field at the top interface, no coefficient has been displayed for this method.

The previous calculations on the dielectric slab provide an intuitive approach to the pole expansion and the different convergence behavior obtained with different number of poles. We discussed in the first part of this chapter that a higher order Mittag-Leffler expansion is equivalent to a zeroth order expansion with a higher-order fitted background-correction. However, fitted background terms are not necessary in the case of the dielectric slab because all the resonant modes can be found and the electric fields belonging to the background and resonant modes can be calculated analytically. Nonetheless, fitting procedures provide a powerful tool for more complex structures such as the gratings studied in the next paragraphs.

3.2.4 Efficiency of the method applied to periodic structures

The next numerical example is a one-dimensional dielectric grating with a periodicity of $d_x = 0.8 \mu\text{m}$, a width of $w = 0.53 \mu\text{m}$, and a thickness of $h = 0.1 \mu\text{m}$ displayed in Fig. 3.5. The structure is made of ZnSe with a refractive index of 2.6 surrounded by air. We consider a s-polarized incident plane wave with in-plane wave vectors $k_x = 0.5 \mu\text{m}^{-1}$ and $k_y = 0.7 \mu\text{m}^{-1}$. Using the Green's dyadic Mittag-Leffler expansion, the field's first-order expansion, and the Fourier modal method, we compute the fields generated by incoming plane waves of energies from 1700 meV to 2400 meV. The results computed with the Fourier modal method involve the derivation of the solution of Maxwell's equations at each frequency, thus it will be considered as a reference. All the full wave calculations of the Fourier modal method and the field distributions at the resonances are computed using 51 Fourier harmonics in the reciprocal space without adaptive spatial resolution for this example.

The structure exhibits three resonances between 1700 meV and 2400 meV denoted by black arrows in Fig. 3.6 (a). These resonances and the corresponding field distributions have been calculated using the method described in the section 2.7. The pole expansion of the field and the

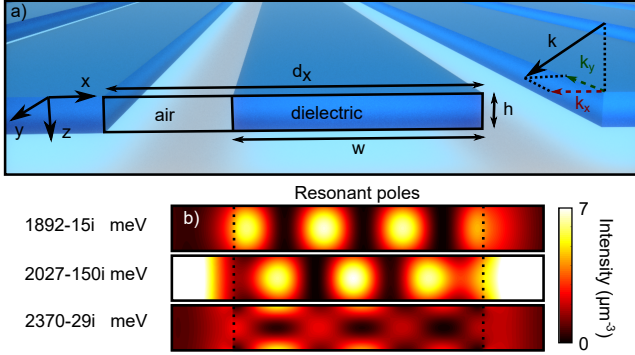


Figure 3.5: (a) Schematic of a one-dimensional dielectric grating with definition of geometrical parameters. (b) Normalized electric field intensity of three resonant states at $1892 - 15i$ meV, $2027 - 150i$ meV, and $2370 - 29i$ meV inside the dielectric grating for period $d_x = 0.8 \mu\text{m}$, width $w = 0.53 \mu\text{m}$, height $h = 0.1 \mu\text{m}$, and a grating refractive index of $n = 2.6$. The incidence parameters are $k_x = 0.5 \mu\text{m}^{-1}$ and $k_y = 0.7 \mu\text{m}^{-1}$. The vertical dotted lines indicate the interface positions, and the horizontal extension of the plots is over one unit cell.

Green's dyadic inside the system are computed accounting for these three resonances. The background contribution is calculated for each method by resolving the exact field distribution inside the structure at three off-resonant energies denoted by the gray arrows in Fig. 3.6 (a). The field outside the structure is computed with the reciprocity theorem and the procedure explained in the previous section. In the case of the one dimensional grating, the near field outside the structure is more complex and contains many diffraction orders, thus instead of only calculating the Fourier coefficient of the fundamental Fourier order, we have to account for the Fourier coefficients of each harmonic $\alpha_{s/p, \mathbf{K}}^{t/b}$ in the two different polarization. The considered grating has a Rayleigh anomaly at 1550 meV that marks the opening of diffraction channels to the far field. Thus, beyond 1550 meV any small error in the calculation of the field propagating inside higher order Fourier harmonics can have dramatic consequences. However the pole expansion of the field and the Green's dyadic remain very accurate. We calculate the L^2 error for each method by integrating along x and z the square of the the absolute value of the fields from the pole expansion divided by the integration of the squared absolute value of the field computed with the Fourier modal method. The division of one by the other provides the relative error displayed in panel b). As it is plotted one can observe that the error exhibited by the Green's dyadic expansion

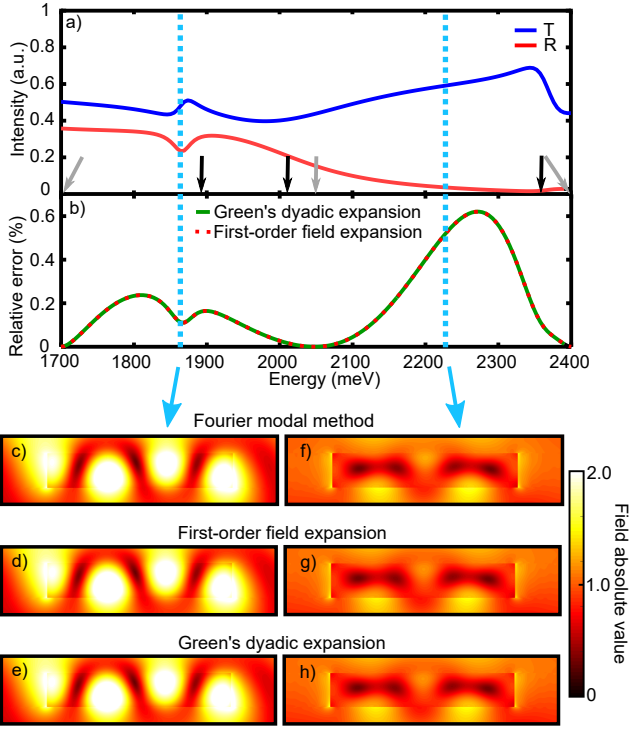


Figure 3.6: (a) Spectra of the dielectric grating shown in Fig. 3.5. The three resonant states of Fig. 3.5(b) have been used for the pole expansions of the near fields. Their spectral position is indicated by black arrows. (b) Relative L^2 error of pole expansion integrated over one unit cell of the structure along x and over the thickness of the grating plus 50 nm of superstrate and substrate. As a reference, we used the field computed with the Fourier modal method. (c-h) Map of the absolute value of electric field within the structure and its surrounding at 1870 meV (c-e) and 2225 meV (f-h). The electric field is calculated by the Fourier modal method (b,e) as well as the Mittag-Leffler expansion of the total field (d,g) and the Green's dyadic (e,h). Note that the pole expansion of the fields includes a quadratic fit of the background field at the positions of the gray arrows.

is almost equal to the error of the field expansion. A very detailed plot would reveal that the Green's dyadic expansion is 0.0001% more accurate.

The field distributions are displayed in two columns and three rows. Each column denotes a calculation whether at 1870 or 2225 meV. The field distribution of the first row Fig. 3.6 (c) and (f) show the full wave calculations provided by the Fourier modal method. In the second row, panel (d) and (g) is displayed the field calculated using the first-order field expansion. Finally in the last row, panels (e) and (h) are displayed the results obtained with the Green's dyadic pole expansion. We can appreciate that almost no deviation can be observed by eye.

The structure of the third example is displayed Fig. 3.7 (a). It is a two dimensional grating made of periodically arranged rectangular holes filled with air in a film made of gold. The structure is 50 nm thick and surrounded by air. The grating has a periodicity of $d_x = d_y = 1.2 \mu\text{m}$ and the size of each hole is $w_x = 300 \text{ nm}$ by $w_y = 960 \text{ nm}$. The permittivity of gold is computed with the critical point model [73]. The system is excited by plane waves incoming with normal incidence and polarized along x . In Fig. 3.7 (b) is displayed the spectra of the structure from 200 meV to 900 meV. In this spectral range, the system has one resonance for x polarized electric fields at $543 - 135i$ meV that is marked with a black arrow in Fig. 3.7 (b). Panel (c) displays a map of the intensity belonging to the resonance at $543 - 135i$ meV. In panels (d-f) is plotted the field calculated 12 nm below the top interface of the grating, for the near field induced by an x -polarized incoming plane wave at an energy of 537 meV. The fields are calculated with the Fourier modal method (d), the first order field expansion (e) and the Green's dyadic pole expansion (f). The fields are calculated using adaptive spatial resolution and 29×29 Fourier harmonics. The fastest approach makes use of the Mittag-Leffler expansion of the full field, but the fields derived with the Mittag-Leffler expansion of the Green's dyadic are more accurate, as can be seen by the small deviations between panels (e) and (f) of Fig. 3.7.

In these examples we can see that the fit procedure and the field expansion can be computed while using the adaptive spatial resolution. More importantly, we know that adaptive spatial resolution is extremely useful to describe metal-dielectric interfaces. It demonstrates that the pole expansion can be used in combination with other features to describe more complex systems.

In addition the series expansion provides an easy and switchable access to the contribution of each pole, to the overall behavior of a system. Moreover, depending on the polarization state and the field symmetries of a pole, the calculations of the overlap integrals can be greatly simplified.

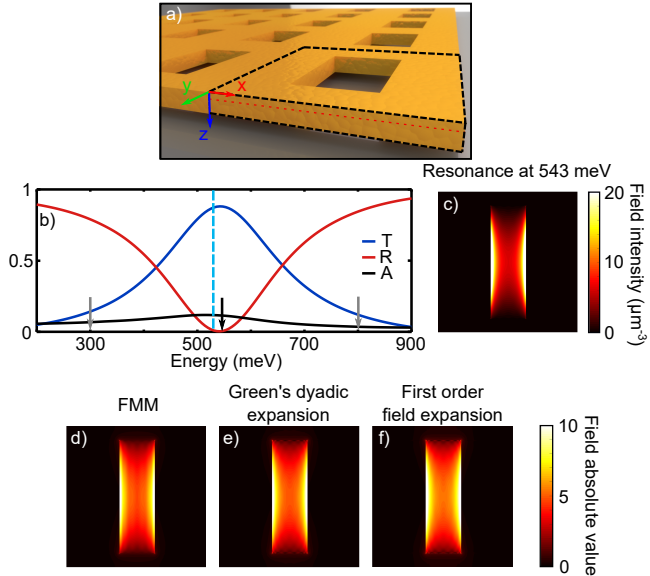


Figure 3.7: (a) Schematic of gold film of thickness 50 nm with air holes of size 300 nm times 960 nm in a square lattice configuration with period 1.2 μm . (b) Reflectance (red), transmittance (blue), and absorbance (black) of the gold grating depicted in panel (a) for a plane wave excitation at normal incidence from the top with field polarized along x . Panel (c) displays the normalized electric field intensity of an exemplary resonant state of that system at 543 – 135*i* meV. The resonance position is indicated by a black arrow in panel (b). The field distributions displayed at the bottom panels are calculated at 537 meV [light blue dashed vertical line in (b)] by the Fourier modal method (d), the Mittag-Leffler expansion of the Green’s dyadic (e), and the first-order Mittag-Leffler expansion of the total field (f). The background contribution to the pole expansions has been fitted by a first-order polynomial to exact results at 300 meV and 800 meV [indicated by the gray arrows in panel (b)]. All field distributions are calculated in the xy plane of a unit cell, 12 nm below the top interface [red dashed line in panel (a)].

The overlap integral calculation itself provides a quantitative method to measure the coupling of each mode with the exterior of the structure that independently of the field calculation helps to understand the physics and the mechanism behind any arbitrarily chosen system.

Thus, the pole expansion has many advantages and can be implemented upon another solver. However, the accuracy of the method is entirely limited to the accuracy with which the resonant energies and the associated fields are computed. Few mode searchers exist, nonetheless this numerical task is still improved regularly [67, 74, 75]. Thus, this method benefits from any improvement achieved in the development mode solver with higher speed or accounting for more different phenomena such as nonlocality, which would allow us to model structures with more delicate properties [21, 76, 77].

4 Nonlinear optics

It doesn't matter how beautiful your theory is, it doesn't matter how smart you are. If it doesn't agree with experiment, it's wrong.

Richard Feynman (1918-1988)

4.1 Introduction

In the previous chapter, we detailed one method to solve Maxwell's equations inside one- or two-dimensional layered structures with common invariance symmetry amongst their layers. The scheme presented in the previous chapters account only for the linear optical properties of the materials. However, in the case of highly nonlinear materials or in the situation where the near field is strongly enhanced, the nonlinear properties of the considered materials cannot be neglected anymore. Thus, in these situations we have to describe additional light-matter interactions.

In this chapter, we will first briefly study different microscopic descriptions of nonlinear optical phenomena. The first numerical approach we will present is a method used in previous works [78] that provides the efficiency of harmonic conversion without accounting for the propagation of the generated harmonic to the far field. We will call a method with such a characteristic a non-propagative approach. Then we will present a rather heavy but very stable method based on a full wave calculation using the reciprocity principle to derive harmonic generation within nanostructures accounting for the propagation of the generated harmonic to the far field. Then, we will describe the second-harmonic generation inside dielectric materials such as GaAs and LiNbO₃. Second-order nonlinear optical phenomena inside dielectric media are described using the third rank tensor $\chi^{(2)}$. The approach depicted next is the implementation of a direct emission scheme within the Fourier modal method. In a last scheme, we will study the implementation of the pole expansion for nonlinear optics. As it has been explained, the pole expansion approach is extremely fast and reduces considerably the heavy numerical cost required for the modeling of nonlinear effects. It will be used in the picture of second-, third- and higher-harmonic generation within a dielectric slab. Finally, we will study how the pole expansion approach can be used to describe the Kerr optical effect.

4.2 Different microscopic models

The different methods presented in this chapter to account for nonlinear phenomena describe the nonlinear properties of a material using higher order tensors such as the $\chi^{(2)}$ and $\chi^{(3)}$ tensors. However, the values and the symmetry of these tensors are related to the choice of a microscopic model to describe the anharmonic character of the microscopic polarization induced inside the nonlinear media. A first approach is the description of the microscopic polarization by a dipole oscillating as a classic anharmonic

oscillator inside a potential $V_p(x)$ (for a one dimensional system).

In the situation where V_p is a quadratic function, the strength of the restoring force acting on the oscillator is proportional to x and the response of the oscillator contains only the frequency of the external driving force [79, 80]. Nonetheless, V_p can be described as a higher order polynomial

$$V_p(x) = \sum_{j=1}^n a_j x^j, \quad (4.1)$$

where a_j is the amplitude of each polynomial order and the term a_0 is most of time nil unless the system is exposed to an electrostatic field.

In the latter case, the restoring force contains n harmonics of the excitation frequency which will be as many harmonics radiated by the dipole. The restoring force is proportional to the opposite of the derivative of the potential [79], thus to observe the apparition of a second- or other even-harmonics, we need a potential depicted by a polynomial containing third order terms x^3 and higher odd-orders, respectively. As a consequence, to exhibit a response with even harmonics-order the potential of the oscillator has to be asymmetric [80, 81]. Through this picture, we understand that the induction of a nonlinear polarization field of an even order requires a symmetry breaking inside the structure. The nature of the symmetry breaking can occur at the crystalline or at the structural levels, as it will be explained shortly.

The symmetry of a nonlinear susceptibility tensor is related to the crystalline symmetry of the material of interest, henceforth only dielectric materials with non centro-symmetric lattices should generate second-harmonic [81]. However, nano-particles made of metals with centro-symmetric lattices are still able to generate a second-harmonic. The reason of this behavior is due to the population of quasi free electrons oscillating inside metallic structures. Indeed, when such metallic nano-particles are exposed to electromagnetic radiations, an electric field exponentially decaying is induced inside the metal near the interfaces [82, 83]. Thus, the quasi-free electrons oscillating with the field near the interfaces behave as oscillators inside a gradient of potential. The gradient induces a symmetry breaking in the potential that transforms the harmonic oscillator into an anharmonic oscillator. This process enables the emission of even harmonics-order by the polarization field induced by the quasi-free electrons oscillating an-harmonically near interfaces. These surface effects induce local symmetry-breaking near interfaces. Such nonlinear behavior is described, modeling electrons as a cold plasma within the so called *hard wall hydrodynamic model* and *jellium hydrodynamic model* [58, 84, 85]. Thus, in these pictures the equation of motion of electrons is derived from

fluid mechanics [83] that provides the expression of a current term. Then this current term is used in the derivation of Maxwell's equations [86].

As mentioned above, solving Maxwell's equations in metals leads to the calculation of evanescent modes that exhibit exponentially decaying field distributions near metal dielectric interfaces. The exponential profile of the modes on the metal side of the interface exhibits spatial derivatives that are rather difficult to compute numerically. Experimentally, this type of measurement is utterly difficult to set up in a reproducible manner. Indeed, experimental parameters such as the roughness of the metal dielectric interfaces are difficult to control and influence dramatically the efficiency of the second harmonic conversion. Beyond this observation, nonlinear surface effects are sensitive to structural symmetry-breaking and imperfections small enough to be hardly detectable and even more difficult to control in the production process of an experiment.

Unlike second-harmonic generation, the third-harmonic generation inside metal nano-particles is mostly a volumetric effect [87] that is more accurately controllable experimentally. However, we will see in the next chapter that even though the third-harmonic generation inside metal nano-particles is a volumetric effect, it still undergoes the strong influence of minute structural imperfections. In the numerical examples of the next chapter, we will use the method based on the volumetric form of the reciprocity principle described in the previous paragraphs Eq. (4.5) to calculate the third-harmonic generation inside metal nanoparticles with a complex geometry. In these examples, the structures exhibit mode hybridization and complex plasmonic phenomena that we tailored to achieve different effects such as electromagnetically induced absorbance. We will study these phenomena and their interest in nonlinear optics. The microscopic model used to express the $\chi^{(3)}$ tensor in the next chapter is based on the anharmonic oscillator model, which is a good approximation if we stay away from material resonances such as inter-band transition-energies. The anharmonic description of the motion of electrons can be found in textbooks [81] and yields

$$\chi^{(3)}(3\omega; \omega, \omega, \omega) = \frac{4\pi\omega_0^2 m}{3d^2 N^3 e^4} \chi^{(1)}(3\omega) [\chi^{(1)}(\omega)]^3, \quad (4.2)$$

where ω_0 is a resonance frequency related to the metal properties, N is the density of atoms, m and e are the mass and the charge of an electron. Finally d is a length of the order of the material lattice constant.

In this section, we have thus discussed the microscopic models used to describe nonlinear optical phenomena inside dielectrics en metals. In the next sections, we will describe numerical approaches using these microscopic models to solve nonlinear Maxwell's equation inside nanostructured

media.

4.3 Non-propagative and reciprocity based approaches

4.3.1 The non-propagative method

Let us first present a simple approach to derive the efficiency of harmonic conversion for volumetric nonlinear optical phenomena [87, 88]. We consider a third order nonlinear phenomenon generating third-harmonic. The first step is to derive the induced nonlinear polarization using the anharmonic oscillator model as

$$\mathbf{P}^{(3)}(3\omega) = \chi^{(3)}(3\omega; \omega, \omega, \omega) \mathbf{E}_{\text{loc}}^3(\omega), \quad (4.3)$$

where \mathbf{E}_{loc} is the local field at the pump frequency inside the material with nonlinear properties. $\chi^{(3)}$ is derived using Eq. (4.2).

In a second step, the efficiency of the harmonic conversion can be approximated by integrating the complex nonlinear polarization inside the volumes of nonlinear materials [78]. Thus the integration yields:

$$E_{\text{THG}}(3\omega) \approx 3\omega \int_V \mathbf{P}^{(3)}(\mathbf{r}, 3\omega) d\mathbf{r}^3. \quad (4.4)$$

This method is rather simple and it can be implemented using the Fourier modal method or a finite element method. However, in this approach we do not calculate the propagation of the field at the third harmonic to the far field. Thus we do not account for the radiation efficiency of the third harmonic from near field to far field. Nevertheless, in the next paragraphs, we will derive a more accurate method that will account for the propagation of the third harmonic to the far field using the reciprocity principle.

4.3.2 Emission by reciprocity

Let us remind that we focus on structures made of layers that are periodic along one or two directions with common translation symmetry. In structures with such properties, we demonstrated in chapter 2 that we can use the reciprocity principle depicted in Eq. (2.53) to calculate the field emitted outside a structure by a volumetric emitter located inside the system. For instance, in the case of nonlinear optical phenomena, we can describe

third-harmonic generation by considering nonlinear material as volumetric emitters [87]. Thus, to derive the far field radiated at the third harmonic, we can use either a surface overlap integral over the generated field at 3ω as in Eq. (2.56), or a volumetric overlap integral over the source term describing the nonlinear interaction as in Eq. (2.57). We will use the latter form, but let us first remind the master equation we need:

$$\alpha_{a,\mathbf{K}}^{t/b} = \mathbb{B}_V \left[(\mathbb{F}_B)_{a,-\mathbf{K}}^{t/b}, \mathbb{J}_A \right]. \quad (4.5)$$

In the latter equation, \mathbb{J}_A denotes a source current radiating a field from inside the closed volume V , $\mathbb{F}_{B_{a,-\mathbf{K}}}^{t/b}$ is the near field produced by a plane wave incoming from the exterior of V , with the in-plane momentum $-\mathbf{K}$ and the polarization $a \equiv s$ or p . The operator \mathbb{B}_V denotes the volumetric integral defined equation Eq. (2.42). The latter vector function applied to the source term \mathbb{J}_A and the near field $\mathbb{F}_{B_{a,-\mathbf{K}}}^{t/b}$ provides the amplitude of the field radiated by the source A , outside the volume V , in the diffraction channel \mathbf{K} and with the polarization a . This calculation can be done for excitation fields coming from the top and bottom half spaces, above and below the system, which are referred to with the superscript t/b . The result of the volumetric integrals is denoted by the Fourier coefficients $\alpha_{a,\mathbf{K}}^{t/b}$. Thus, the electric and magnetic fields emitted outside the structure can be expressed as the superposition of plane waves:

$$\mathbb{F}_{\text{tot}}^{t/b} = \sum_{a,\mathbf{K}} \alpha_{a,\mathbf{K}}^{t/b} \mathbb{O}_{a,\mathbf{K}}^{t/b}, \quad (4.6)$$

where $\mathbb{F}_{\text{tot}}^{t/b}$ is the total field radiated outside the structure by the source \mathbb{J}_A , $\alpha_{a,\mathbf{K}}^{t/b}$ is the result of the overlap integral equation (4.5) and $\mathbb{O}_{a,\mathbf{K}}^{t/b}$ is the basis unit vector defined Eq. (2.39) and normalized with the constant given Eq. (2.47). Using this approach, we can compute the Fourier coefficients of the field radiated in the diffraction channels that propagate to the far field. It is important to note that in the case of harmonic generation, the source current can be derived from the nonlinear polarization field: $j^\alpha = -i\omega P^\alpha/4\pi$.

The advantage of this approach is that the overlap integral can be calculated whether in the Fourier reciprocal space or in the real space. In the context of the calculation of third-harmonic generation, as it will be explained later, heavy factorization rules hampers the calculation of the nonlinear polarization in the reciprocal Fourier space. However, the nonlinear polarization can be computed in real space from the known spatial distribution of the materials, their nonlinear susceptibilities and the inverse

Fourier transformation of the fields inside the layers. Thus, a volumetric integral evaluated in real space will avoid issues related to the finite size of the reciprocal space and it leads to the value of the field radiated outside the system at the third harmonic.

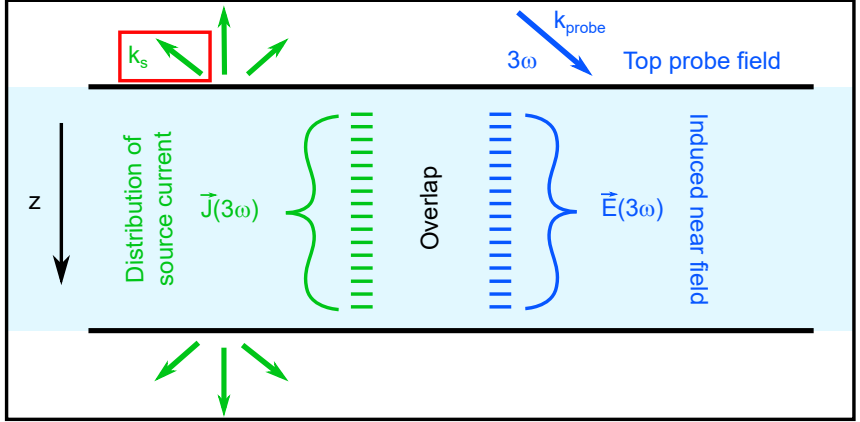


Figure 4.1: This scheme describes how the amplitude of the field emitted above the structure by a source current is calculated using the reciprocity principle. According to Eq. (4.5) the amplitude of the field radiated in a certain diffraction order \mathbf{K} is the volumetric overlap integral of the source current distribution with the near field induced by an incoming plane wave propagating in the diffraction order $-\mathbf{K}$. This procedure has to be repeated to compute the field above and below the structure. Depending if we compute the radiated near field or the far field, we need to calculate the overlap integral for incoming plane wave in all diffraction order, or we just account only for the diffraction order reaching the far field.

The procedure is as follow: First, using the Fourier modal method, we calculate the near field produced inside the structure by an incoming excitation field, at the pump frequency. The near field is originally computed in the Fourier reciprocal space, however to avoid any issue related to the truncation of the reciprocal space, we transform the fields back to the real space. Thus, using any kind of microscopic model, one can calculate the value of the $\chi^{(3)}(\mathbf{r}; k)$ tensor inside materials exhibiting nonlinear properties. Then, multiplying the latter forth-order tensor with the near field computed earlier, we obtain the value of the third order nonlinear polarization $P^{(3)}(\mathbf{r}; k)$ in real space.

In a second step, we calculate at the third order frequency the propagation inside the structure of s- and p-polarized incoming plane waves from

the top and bottom half spaces. The distribution of these probe fields inside the structure is calculated using the Fourier modal method. The resulting near fields are then transformed back into real space.

The last step is the most important and the most meaningful. In the case of third harmonic generation where the third-order nonlinear polarization is calculated in real space as described above, we calculate the overlap integral equation (4.5) in real space. We do not need to worry about factorization rules in the calculation of $P^{(3)}(\mathbf{r}; k)$ and we can still use adaptive spatial resolution to achieve accurate results. The backside of this method is the necessary inverse Fourier transformations of the pump field and the probe field at the third harmonic, which are extremely time consuming.

One possible improvement would be the calculation of the near fields induced by the pump and the probe fields using the approach of the pole expansion in real space. In this context the field is calculated in the reciprocal Fourier space at the position of the resonant energies and transformed back in real space. Finally, the electromagnetic fields inside the structure can be calculated at any frequency by using the pole expansion of whether the field or the Green's dyadic in real space. This method would considerably reduce the number of indispensable inverse Fourier transformations to the number of poles inside the spectra while the nonlinear polarization and the overlap integral are still evaluated in real space.

4.4 Nonlinear optics in modal methods

4.4.1 Inhomogeneous Maxwell's equations

Let us consider the second-harmonic generation taking place inside a multilayer made of a dielectric material whose nonlinear susceptibility is described by the third rank tensor $\chi^{(2)} \neq 0$. The value of this tensor comes from the microscopic model chosen to describe the nonlinear phenomenon. A good approximation is provided by the anharmonic oscillator model, though a more complete description can be derived from quantum mechanics [81]. However, in the following section the values used are measured data [81]. Let us consider just the type of periodic multilayer that can be modeled within the Fourier modal method. The structure is excited by an incoming plane wave that we will call the pump. The linear scattering of this plane wave at the frequency ω is described by the linear Maxwell's equations that are solved within the Fourier modal method as described chapter 2. However, a part of the energy carried by the pump is scattered at the second-harmonic frequency 2ω . The phenomenon is described by the

nonlinear susceptibility that is a function of 3 frequencies. One frequency is the generated frequency and the two others are the frequencies of the interacting fields. For instance the tensor for second-harmonic generation is written: $\chi^{(2)}(2\omega; \omega, \omega)$. In addition, a back interaction of the second harmonic with the pump is possible, it is expressed as $\chi^{(2)}(\omega; 2\omega, -\omega)$. In the following description we decide to use the undepleted pump approximation in the limit of slowly varying envelopes. Thus, we do not account for the energy depletion caused by the second-harmonic generation in the propagation of the pump field. Additionally, we do not account for the back conversion $\chi^{(2)}(\omega; 2\omega, -\omega)$, neither do we account for the sum frequency $\chi^{(2)}(3\omega; 2\omega, \omega)$ and the optical rectification $\chi^{(2)}(0; \omega, -\omega)$, which are also second order effects. It is obvious that in a real system the energy carried by the generated harmonics has been provided by the pump field. Hence, the undepleted-pump approximation stands only if a small amount of energy is transferred without dramatic consequences on the shape and intensity of the pump field. The limit of the slowly varying envelopes imply that the envelope of the incoming pump field should vary slowly in time and space compared to the field pulsation and wavelength, respectively.

The undepleted pump approximation leads us to a two-step process. We first derive the pump field from Maxwell's equations for a given incident field. The resulting near fields behave as sources for fields at the generated harmonic frequency. The emission intensity of these sources at the harmonic depends on the nonlinear susceptibility tensor as well as on the optical properties of the given system at the harmonic. Therefore, we need to solve only two linear problems – a homogeneous and an inhomogeneous differential equations for the pump field and the field generated at the harmonic, respectively. The nonlinear response of structures undergoing an interaction of order n is proportional to the pump field magnitude raised to the power n . Thus, small errors in the linear field calculation propagate in the numerical scheme with a dramatic effect hampering the computed nonlinear response. As a consequence, the modeling of nonlinear optical phenomena has a heavy numerical cost. The modeled structures have to be described with an extremely fine spatial grid, in order to increase the accuracy of the linear calculation and to resolve the wavelength of the generated harmonics. Though the resolution of two systems of Maxwell's equations with high accuracy is rather time consuming, the sampling of nonlinear tensors $\chi^{(n)}$ owning 3^{n+1} components in a fine grid requires computers with a large memory and the memory allocation time might be longer than the calculations themselves. In this context, the improvement of the numerical methods describing nonlinear optical phenomena is highly relevant.

Though modal methods such as the Fourier modal method described in chapter 2 are restricted to the description of layered structures, one of the strength of these methods is the absence of spatial discretization in the direction of invariance of the layers. These schemes solve the propagation of the field inside each layer at once, which is fast compared to other methods. In addition, the absence of discretization avoids numerical artifact or nonphysical discontinuities inside layers. Thus, the low error and the speed of the Fourier modal method are perfectly suitable for the calculation of nonlinear optical phenomena in multilayers.

Possible formulations for the calculation of harmonic generation in the Fourier modal method with the undepleted approximation are described in Refs. [89, 90].

While previous approaches for solving the inhomogeneous equations at the generated harmonic rely on deriving the solutions for entire layers [89, 90], we propose here to consider nonlinear sources in planes normal to the stacking direction and to coherently integrate over the emission of these sources. Thus, we treat the harmonic emission in the same way as the emission from currents in certain layers [91, 92], with the currents originating now in the nonlinear polarization.

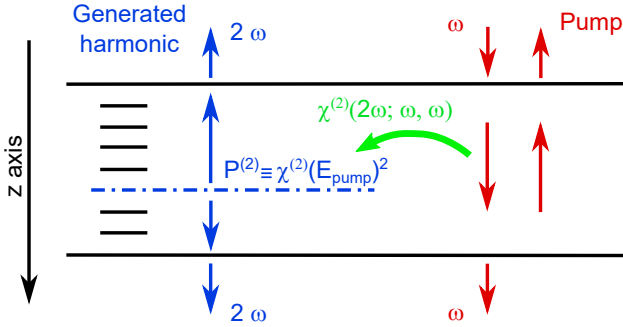


Figure 4.2: Numerical scheme describing the generation of the second-harmonic within a single layer assuming the undepleted pump approximation. The near field distribution induced by the pump is calculated at every position along z but it is numerically evaluated only at the position of the set of slices. The nonlinear polarization induced by the pump field is calculated at the position of each slice denoting virtual planar emitters. The total volumetric emission of the second harmonic is obtained by integrating numerically along z , the field emitted by all the planar emitters.

Moreover, we combine the derivation of the harmonic emission with two advanced formulations of the Fourier modal method: Factorization rules [4,

30] and matched coordinates with adaptive spatial resolution [31, 32]. As explained chapter 2, these formulations have been introduced in order to prevent inaccuracies in the Fourier modal method related to the Gibbs phenomenon that occur due to the finite Fourier basis. Regarding the factorization rules, we find that their formulation for the second-harmonic susceptibility has been incomplete in previous works [89, 90]. In particular, we show that it is necessary to account for the discontinuities of the fields at the pump energy and the harmonic simultaneously. This new formulation of the Fourier factorization of the nonlinear susceptibility tensor allows for including matched coordinates and adaptive spatial resolution. Thus, even nontrivial lateral geometries with large contrast in the dielectric function can be calculated efficiently by using a coordinate system in which all material interfaces are described by surfaces of constant coordinates with an increased spatial resolution in the vicinity of these interfaces.

Let us remind the covariant formulation of Maxwell's equations (in frequency domain and Gaussian units) with a nonlinear polarization:

$$\epsilon^{\alpha\beta\gamma}\partial_\beta E_\gamma = ik_0\mu^{\alpha\beta}H_\beta, \quad (4.7)$$

$$\epsilon^{\alpha\beta\gamma}\partial_\beta H_\gamma = -ik_0(\epsilon^{\alpha\beta}E_\beta + P^\alpha) + \frac{4\pi}{c}j^\alpha. \quad (4.8)$$

Equations (4.7) and (4.8) hold for higher harmonics and for the pump field, with P^α and j^α denoting the α component of the nonlinear polarization and free currents, respectively. The time dependence of the fields is assumed to be $\exp(-i\omega t)$; the vacuum wave number is denoted as $k_0 = \omega/c$. In the undepleted pump approximation for harmonic generation, $P^\alpha(\omega) = 0$ at the pump energy, while the simplest form at the generated harmonic is given by [90]

$$P^\alpha(n\omega) = 4\pi\chi^{(n),\alpha\beta_1\beta_2\dots\beta_n}(n\omega;\omega,\omega,\dots)\underline{E}_{\beta_1}(\omega)\underline{E}_{\beta_2}(\omega)\dots\underline{E}_{\beta_n}(\omega), \quad (4.9)$$

with the underlined quantities calculated at the pump frequency and $\chi^{(n),\alpha\beta_1\beta_2\dots\beta_n}$ being the components of the n^{th} -harmonic susceptibility tensor. Therefore, in the undepleted pump approximation, the equations describing the pump field are independent of the fields at the harmonic, whereas the pump field enters as an inhomogeneity in the equations at the generated harmonic.

The calculation of the field at the pump frequency is carried out as explained in the section (2.6). The field evaluated inside the material with nonlinear properties is discretized along the stacking direction as a series of plane surfaces. Knowing the pump field, we convolute the latter with the nonlinear permittivity in the reciprocal space to find the nonlinear polarization field.

However, to evaluate the polarization field correctly and accurately near interfaces, the nonlinear tensor has to be expressed in curvilinear coordinates with adaptive spatial resolution. $\chi^{(n)}$ is a tensor of rank n and weight one. The transformation of this tensor from curvilinear coordinates to general coordinates is:

$$\chi^{(n),\rho\sigma_1\sigma_2\dots\sigma_n} = \bar{\chi}^{(n),\alpha\beta_1\beta_2\dots\beta_n} \sqrt{g} \frac{\partial x^\rho}{\partial \bar{x}^\alpha} \frac{\partial x^{\sigma_1}}{\partial \bar{x}^{\beta_1}} \frac{\partial x^{\sigma_2}}{\partial \bar{x}^{\beta_2}} \dots \frac{\partial x^{\sigma_n}}{\partial \bar{x}^{\beta_n}}. \quad (4.10)$$

In the polarization vector Eq. (4.9), we replace the nonlinear permittivity tensor and the fields of the uniform coordinate system by those of the nonuniform coordinate system specified in Eqs. (4.10) and (2.8). Then in the next paragraphs, we carry out the Fourier transformation of the nonlinear susceptibility according to the correct Fourier factorization rules.

4.4.2 Factorization rules

Matched coordinates are indispensable to calculate the field emitted near curvilinear interfaces as in the geometry presented Fig. 2.4. However, the discontinuity of the pump field and the harmonic field at the interfaces produces a dramatic computational error as demonstrated by L. Li for the linear field [30]. Thus, the Fourier transformation of the nonlinear permittivity tensor will require the definition of new factorization rules. The following explanation and calculation can be applied to a tensor $\chi^{(n)}$ of rank n , however we decide to restrict the following demonstration to the tensor $\chi^{(2)}$, the reason of this choice will be provided at the end of the demonstration.

In a first step, we proceed as for the Li's factorization rules described section 2.6. Consider an interface with a normal vector that equals the contravariant basis vector \mathbf{e}^α . D^α is normal to the interface, while E_β with $\beta \neq \alpha$ gives the two tangential electric field components. The constitutive equation for D^α at the generated harmonics is:

$$D^\alpha = \varepsilon^{\alpha\alpha} E_\alpha + \varepsilon^{\alpha\beta} E_\beta + \underbrace{4\pi\chi^{(2),\alpha\rho\sigma} E_\rho E_\sigma}_{P^\alpha}, \quad \alpha \neq \beta. \quad (4.11)$$

We remind that there is no sum convention over index α in the current section, and the sum convention over β runs only over indices $\beta \neq \alpha$. The sum convention for σ_1 and σ_2 spans over all indices.

In a first step, we express the discontinuous component of the electric field as a function of the other field components. Some calculus leads to

the equation:

$$[D^\alpha]_\alpha = [(\varepsilon^{\alpha\alpha})^{-1}]_\alpha^{-1} \left([E_\alpha]_\alpha + [(\varepsilon^{\alpha\alpha})^{-1}\varepsilon^{\alpha\beta}]_\alpha [E_\beta]_\alpha \quad \beta \neq \alpha, \right. \\ \left. + 4\pi [(\varepsilon^{\alpha\alpha})^{-1}\chi^{(2),\alpha\rho\sigma}]_\alpha \underline{E}_\rho \underline{E}_\sigma \right)_\alpha, \quad (4.12)$$

where we denote the Fourier transformation by square brackets with the direction of the transformation as subscript.

This derivation provides the accurate Fourier transformation of D^α for \mathbf{e}^α being normal to the interface. The Fourier transformation of the other two components D^β in direction x^α can be found by substituting E_α in the constitutive equation for D^β by :

$$E_\alpha = (\varepsilon^{\alpha\alpha})^{-1} D^\alpha \quad -(\varepsilon^{\alpha\alpha})^{-1}\varepsilon^{\alpha\beta} E_\beta \quad \alpha \neq \beta. \\ -(\varepsilon^{\alpha\alpha})^{-1}\chi^{(2),\alpha\beta\gamma} \underline{E}_\beta \underline{E}_\gamma, \quad (4.13)$$

We finally achieve:

$$[D^\beta]_\alpha = [\varepsilon^{\beta\alpha}(\varepsilon^{\alpha\alpha})^{-1}]_\alpha [D_\alpha]_\alpha \\ + [\varepsilon^{\beta\gamma} - \varepsilon^{\beta\alpha}(\varepsilon^{\alpha\alpha})^{-1}\varepsilon^{\alpha\gamma}]_\alpha [E_\gamma]_\alpha \quad \beta \neq \alpha \ \& \ \gamma \neq \alpha. \\ + 4\pi [\chi^{(2),\beta\rho\sigma} - \varepsilon^{\beta\alpha}(\varepsilon^{\alpha\alpha})^{-1}\chi^{(2),\alpha\rho\sigma} \underline{E}_\rho \underline{E}_\sigma]_\alpha, \quad (4.14)$$

Inserting Eq. (4.12) into Eq. (4.14) and repeating these steps for the second direction of periodicity yields the factorization as expressed in Eqs. (2.73) and (2.74), for the linear part of the constitutive equation. Thus, the dielectric permittivity at the higher harmonics is factorized in the same fashion as the permittivity in the linear problem Eq. (2.74).

Similarly, it is possible to construct from Eqs. (4.12) and (4.14) an operator m_τ^\pm that should be applied to the second-harmonic susceptibility tensor and accounts for the discontinuities at the second harmonic:

$$G \equiv m_\tau^\pm(B)C, \quad G^{\alpha\rho\sigma} = \begin{cases} B^{\tau\tau} C^{\tau\rho\sigma}, & \alpha = \tau; \\ C^{\alpha\rho\sigma} \pm B^{\alpha\tau} C^{\tau\rho\sigma}, & \alpha \neq \tau. \end{cases} \quad (4.15)$$

Here, the tensors B and C are results of applying specific operators to the permittivity and second-harmonic susceptibility, respectively. For the latter, we have to additionally take into account the discontinuities of the pump field. Hence, we express the discontinuous components of the electric field of the pump as a function of the continuous components of the electric field and displacement as well as the permittivity tensor evaluated at the pump energy:

$$\underline{E}_\alpha = (\underline{\varepsilon}^{\alpha\alpha})^{-1} (\underline{D}^\alpha - \underline{\varepsilon}^{\alpha\beta} \underline{E}_\beta), \quad \alpha \neq \beta. \quad (4.16)$$

Inserting Eq. (4.16) into Eqs. (4.12) and (4.14) results in lengthy expressions that contain no products of functions with concurrent jump discontinuities, so that they can be Fourier transformed. They consist of products of $m_{\tau}^{-}(l_{\tau}^{-}\varepsilon)$, $\underline{\varepsilon}$ and $\chi^{(2)}$, which can be written in the compact form $m_{\tau}^{-}(l_{\tau}^{-}\varepsilon)j_{\tau}^{-}(l_{\tau}^{-}\underline{\varepsilon})\chi^{(2)}$, with the new operator j_{τ}^{\pm} being defined by

$$\Gamma \equiv j_{\tau}^{\pm}(B)G, \quad \Gamma^{\alpha\rho\sigma} = \begin{cases} G^{\alpha\tau\tau}B^{\tau\tau}B^{\tau\tau}, & \rho = \tau, \sigma = \tau; \\ G^{\alpha\tau\sigma}B^{\tau\tau} \pm G^{\alpha\tau\tau}B^{\tau\tau}B^{\tau\sigma}, & \rho = \tau, \sigma \neq \tau; \\ G^{\alpha\rho\tau}B^{\tau\tau} \pm G^{\alpha\tau\tau}B^{\tau\rho}B^{\tau\tau}, & \rho \neq \tau, \sigma = \tau; \\ G^{\alpha\rho\sigma} \pm G^{\alpha\tau\sigma}B^{\tau\rho} \pm G^{\alpha\rho\tau}B^{\tau\sigma}, & \rho \neq \tau, \sigma \neq \tau. \\ \quad + G^{\alpha\tau\tau}B^{\tau\rho}B^{\tau\sigma} \end{cases} \quad (4.17)$$

We can summarize the application of the factorization rules to the second-harmonic susceptibility tensor as

$$T_{\tau}(\varepsilon, \underline{\varepsilon})\chi^{(2)} = j_{\tau}^{+}(F_{\tau}l_{\tau}^{-}\underline{\varepsilon})m_{\tau}^{+}(F_{\tau}l_{\tau}^{-}\varepsilon)F_{\tau}m_{\tau}^{-}(l_{\tau}^{-}\varepsilon)j_{\tau}^{-}(l_{\tau}^{-}\underline{\varepsilon})\chi^{(2)}, \quad (4.18)$$

which gives the correctly factorized Fourier transform $\chi^{(2)}$ in direction x^{τ} , with the operator l_{τ}^{\pm} defined according to Eq. (2.73). Thus, the final result for the correctly factorized Fourier transform of the second harmonic susceptibility yields

$$\tilde{\chi}^{(2)} = T_2(l_1^{+}F_1l_1^{-}\varepsilon, l_1^{+}F_1l_1^{-}\underline{\varepsilon})T_1(\varepsilon, \underline{\varepsilon})\chi^{(2)}. \quad (4.19)$$

Once the Fourier transformation of the nonlinear susceptibility is derived correctly, it is possible to calculate the nonlinear polarization in the Fourier reciprocal space by the mean of the following convolution:

$$P_{mn}^{\alpha} = \sum_{p', q', p'', q''} \tilde{\chi}_{mnp'q'p''q''}^{(2), \alpha\sigma_1\sigma_2} \underline{E}_{\sigma_1, p'q'} \underline{E}_{\sigma_2, p''q''}. \quad (4.20)$$

Here, m, n, p', q', p'', q'' are integers that refer to the Fourier harmonics of the fields and the nonlinear susceptibility.

These derivations holds for the second-harmonic susceptibility tensor $\chi^{(2)}$. As explained earlier, it can be generalized to higher harmonics as well, however the number of terms that have to be combined to generate the factorized nonlinear permittivity is proportional to a combination of two binomial factors growing with n . For instance the factorization of $\chi^{(2)}$ requires the combination of 75 terms while the factorization of $\chi^{(3)}$ would require the combination of 375 factors. The factors themselves are known quantities of which many are used multiple times, nonetheless the number of necessary additions and multiplications grows accordingly. Thus, another approach should be used for the calculation of harmonic generation at an order higher than two.

4.4.3 Scattering matrix of an emitted field

The correct Fourier transformation of the linear and nonlinear permittivity permits us to solve Maxwell's equations in the Fourier reciprocal space at the frequency of the radiated field. As in the linear case Eq (2.75), we reach a propagation equation that has the form of an inhomogeneous equation [89]:

$$-i\partial_3\mathcal{E}(x^3) = \tilde{M}\mathcal{E}(x^3) + \tilde{\mathbf{Q}}(x^3). \quad (4.21)$$

The inhomogeneous term reads

$$\tilde{\mathbf{Q}}(x^3) = -i4\pi \begin{bmatrix} -K_1(\tilde{\varepsilon}^{33})^{-1}\mathbf{P}^3 \\ -K_2(\tilde{\varepsilon}^{33})^{-1}\mathbf{P}^3 \\ k_0[\tilde{\varepsilon}^{23}(\tilde{\varepsilon}^{33})^{-1}\mathbf{P}^3 - \mathbf{P}^2] \\ -k_0[\tilde{\varepsilon}^{13}(\tilde{\varepsilon}^{33})^{-1}\mathbf{P}^3 - \mathbf{P}^1]. \end{bmatrix}, \quad (4.22)$$

where the quantities K_1 and K_2 are diagonal matrices containing the factors defined by Eq. (2.30), $K_{1,m}$ and $K_{2,n}$ respectively. $\tilde{\varepsilon}_l$ refer to the quantity $l_3^-(\varepsilon)$ and \mathbf{P}^α refers to the nonlinear polarization vector calculated in the Fourier reciprocal space Eq. (4.20).

Then, we would have to integrate the equation (4.21) in the whole layer at once. However, we decided to follow a slightly different path. The total volumetric emission is split in a series of discrete planar emitters. Then from Eq. (4.8), it is obvious that we can treat the nonlinear polarization P^α in the same way as the current j^α , i.e., we define $j^\alpha = -i\omega P^\alpha/4\pi$ in the absence of free currents. In the case that there is a free current in the x^1x^2 plane located at the position x_0^3 that is radiating at the generated harmonic, the field is discontinuous [92]:

$$\begin{pmatrix} \mathbf{E}(x_0^3 + \delta x^3) \\ \mathbf{H}(x_0^3 + \delta x^3) \end{pmatrix} - \begin{pmatrix} \mathbf{E}(x_0^3 - \delta x^3) \\ \mathbf{H}(x_0^3 - \delta x^3) \end{pmatrix} = \begin{pmatrix} \tilde{\mathbf{J}}_E(x_0^3) \\ \tilde{\mathbf{J}}_H(x_0^3) \end{pmatrix}, \quad (4.23)$$

where δx^3 describes a small variation around the position x_0^3 . Then, we find at this position a similar source term as in the inhomogeneous propagation equation that we express in the eigenmode basis using the inverse of the material matrix:

$$\tilde{\mathbf{J}}(x_0^3) = \begin{pmatrix} \tilde{\mathbf{J}}_E(x_0^3) \\ \tilde{\mathbf{J}}_H(x_0^3) \end{pmatrix} = -4\pi i\mathcal{F}_0^{-1} \left\{ \begin{array}{l} -K_1(\tilde{\varepsilon}_0^{33})^{-1}\mathbf{P}^3 \\ -K_2(\tilde{\varepsilon}_0^{33})^{-1}\mathbf{P}^3 \\ k_0[\tilde{\varepsilon}_0^{23}(\tilde{\varepsilon}_0^{33})^{-1}\mathbf{P}^3 - \mathbf{P}^2] \\ k_0[\mathbf{P}^1 - \tilde{\varepsilon}_0^{13}(\tilde{\varepsilon}_0^{33})^{-1}\mathbf{P}^3] \end{array} \right\}, \quad (4.24)$$

with the eigenvector matrix \mathcal{F}_0 (material matrix), the Fourier transformed permittivity tensor $\tilde{\varepsilon}_0$ being that of the layer at x_0^3 and \mathbf{P}^α as a supervector

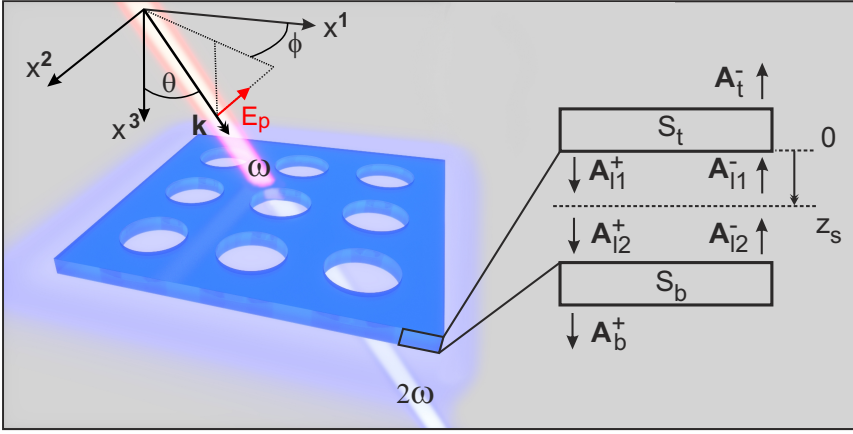


Figure 4.3: Lateral view of a layer of nonlinear material with circular air holes. This structure is one of the examples that will be treated in this paper. As illustrated, the linear field induces a nonlinear polarization that results in a volumetric source at the second harmonic, which we discretize in a set of planar emitting layers. For each discrete source at a position x_0^3 , we calculate the propagation of the field through the structure using the scattering matrix formalism. Then, we integrate coherently over all contributions to obtain the total far field. The inset in the right part depicts a schematic of the scattering matrix formalism, with the amplitude vectors \mathbf{A}^+ and \mathbf{A}^- of downward and upward propagating or decaying eigenmodes in a certain layer [cf. equation (2.79)], respectively. The boxes with S_b and S_t indicate the scattering matrices of the sub-structures above and below a layer.

containing the amplitudes P_{mn}^α of the correctly Fourier factorized second-harmonic polarization.

Thus, the emission of the planar emitter at the position x_0^3 ($x_l^3 < x_0^3 < x_{l'}^3$) is described by the scattering matrix $\Sigma_{l',l}(x_0^3)$ [91, 92]:

$$\mathbf{A}_{l',l}^{\text{out}} = S_{l',l} \mathbf{A}_{l',l}^{\text{in}} + \Sigma_{l',l}(x_0^3) \tilde{\mathbf{J}}(x_0^3). \quad (4.25)$$

with

$$\Sigma_{l',l}(x_0^3) = \begin{bmatrix} S_b^{++} V e^{i\Gamma_0^+(L-x_0^3)} & -S_b^{++} V e^{i\Gamma_0^+ L} S_t^{+-} e^{-i\Gamma_0^- x_0^3} \\ S_t^{--} U e^{-i\Gamma_0^- L} S_b^{+-} e^{i\Gamma_0^+(L-x_0^3)} & -S_t^{--} U e^{-i\Gamma_0^- x_0^3} \end{bmatrix}. \quad (4.26)$$

Here, L is the thickness of the layer generating the second harmonic, S_t and S_b denote the scattering matrices of the groups of layers above and below this region, respectively, and the exponential terms are diagonal

matrices that account for the propagation inside the emitting layer. While deriving the field inside the system, one finds that the amplitude of the internal field is equal to the sum of the field transmitted from the exterior of the structure added to the internal field itself after one round trip inside the system. Thus, each term of the matrix in Eq. (4.26) are divided by a denominator that is the difference of one with the product the reflection coefficients at the top and bottom interfaces times the phase induced by one round trip inside the cavity. These coefficients are denoted by the matrices U and V that account for internal reflections:

$$U = (\mathbb{1} - e^{-i\Gamma_0^- L} S_b^{-+} e^{i\Gamma_0^+ L} S_t^{+-})^{-1}, \quad V = (\mathbb{1} - e^{i\Gamma_0^+ L} S_t^{+-} e^{-i\Gamma_0^- L} S_b^{-+})^{-1}. \quad (4.27)$$

Finally, owing to the linearity of this equation, we can consider the volumetric emission inside the layer as a superposition of sources at positions x^3 , so that

$$\mathbf{A}_{l',l'}^{\text{out}} = S_{l',l} \mathbf{A}_{l',l'}^{\text{in}} + \int_{x_l^3}^{x_{l'}^3} dx^3 \Sigma_{l',l}(x^3) \mathbf{J}(x^3). \quad (4.28)$$

Thus, in this paragraph, we have split the nonlinear volumetric emission of a layer in a series of discrete contributions that we can integrate numerically. This approach avoids to integrate inhomogeneous equation (4.21) that would require a lot of memory and power, while the source term can easily be computed step by step for each planar emitter.

4.4.4 Numerical calculations

As a test system, we consider an asymmetric one-dimensional grating, which is depicted in Fig. 4.4 (a). The structure consists of two adjacent periodic layers with GaAs surrounded by air. Each layer is 100 nm thick. The width of the GaAs region in the upper and lower layer is 0.66 μm and 0.75 μm , respectively. The period is 1 μm . Without the loss of generality, we consider a constant refractive index of $n = 3.85$ for GaAs.

The crystallographic lattice of GaAs is face centered cubic; in Gaussian units, the reduced representation [81] of the second-harmonic susceptibility is

$$\chi^{(2)} = 10^{-7} \begin{pmatrix} 0 & 0 & 0 & 5.73 & 0 & 0 \\ 0 & 0 & 0 & 0 & 5.73 & 0 \\ 0 & 0 & 0 & 0 & 0 & 5.73 \end{pmatrix} \frac{\text{cm}}{\text{statV}}. \quad (4.29)$$

We consider an incoming pump field that is normally incident with 1 W power per unit cell area. The incident electric field is linearly polarized and aligned along the direction of periodicity. The unpolarized second-harmonic intensity is calculated by summing up the s- and p-polarized intensities radiated in the fundamental diffraction order. The field diffracted in higher diffraction orders can be derived using the same methods, however it is not taken into account in this example.

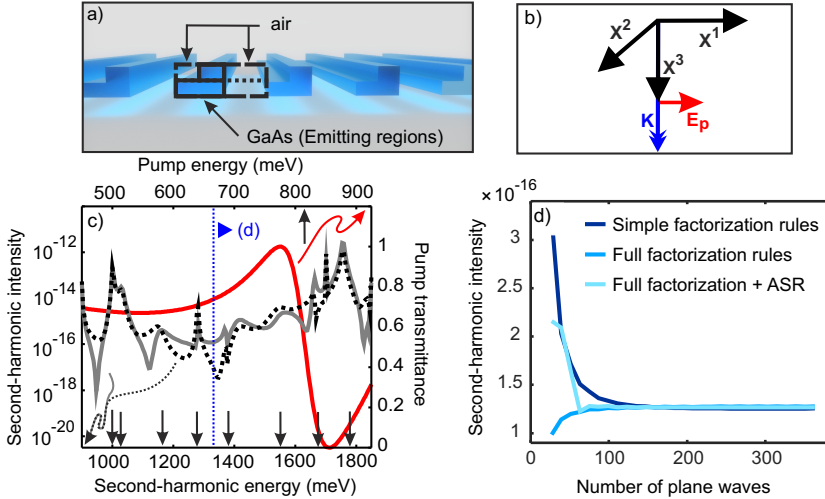


Figure 4.4: (a) One-dimensional periodic asymmetric grating made of GaAs and surrounded by air. This structure consists of two layers, where each layer has a thickness of 100 nm and a period of $1 \mu\text{m}$. The upper part of the grating has a width of $0.66 \mu\text{m}$; the lower part has a width of $0.75 \mu\text{m}$. The second-harmonic emission originates in the GaAs region. (b) The incidence direction is normal, the incident field is p polarized and the incoming pump power is 1 W per unit cell area. (c) Linear transmission (red line), second-harmonic intensity emitted above (black dashed line) and below the structure (gray line) and resonance energies (black arrows). (d) Convergence behavior of the second-harmonic intensity below the system at a pump energy of 670 meV for three different implementations: Simple factorization rules (dark blue line), full factorization rules with (light blue line) and without (blue line) adaptive spatial resolution. When increasing the number of plane waves in the Fourier basis, all three implementations converge to the same value.

In the numerical calculation of the second-harmonic emission, we use a spatial grid of 512 points per unit cell. Fig. 4.4 (b) shows the linear transmittance and the second-harmonic intensity emitted above and below the structure calculated for a reciprocal basis of size 167 Fourier harmonics. In order to illustrate the impact of resonances on the second-harmonic intensity, we denote the resonance energies of that structure by arrows. The resonant energies have been derived from the scattering matrix by the methods described in section 2.7. The two fundamental resonances possess a large linewidth of 84 meV, the higher-order resonances are narrower (from 4.4 meV to 60 meV linewidth). Evidently, we have a peak of emission whenever there is a resonance at the second-harmonic energy.

In order to illustrate the convergence of our calculations, we calculated the second-harmonic intensity for a successively increasing number of plane waves in the reciprocal basis. The results calculated by the Fourier modal method with simple (dark blue line) and full factorization rules with (light blue line) and without (blue line) adaptive spatial resolution are depicted in Fig. 4.4 (c) at a pump energy of 850 meV that is near a fundamental resonance. We can see that all implementations converge to the same value. The formulation with full factorization rules converges faster than the approach with simple factorization rules. The best convergence behavior can be obtained by the formulation with full factorization rules and adaptive spatial resolution.

Two-dimensional grating

Next, we consider a two-dimensional grating that consists of a LiNbO_3 film with circular air holes (see Fig. 4.3). The period is $1.400\ \mu\text{m}$; the radius of the air holes is 600 nm; the thickness of the film is 80 nm. The incoming pump field is normally incident and linearly polarized with 1 W power per unit cell area. The incident electric field is aligned along the x^1 direction. The permittivity of LiNbO_3 is a diagonal tensor with $\epsilon^{11} = \epsilon^{22} = 2.29$ and $\epsilon^{33} = 2.21$. The second-harmonic susceptibility is [81]

$$\chi^{(2)} = 10^{-9} \begin{pmatrix} 0 & 0 & 0 & 0 & -13 & -6.6 \\ -6.6 & 6.6 & 0 & -13 & 0 & 0 \\ -13 & -13 & -75.9 & 0 & 0 & 0 \end{pmatrix} \frac{\text{cm}}{\text{statV}}. \quad (4.30)$$

Fig. 4.5 (a) depicts the linear transmittance and the second-harmonic intensity of this structure calculated for 17×17 plane waves in the Fourier basis (quadratic truncation) and 512×512 spatial points. The structure exhibits a large number of resonances in the given energy range, but only few resonances can be excited by the pump or the second-harmonic energy,

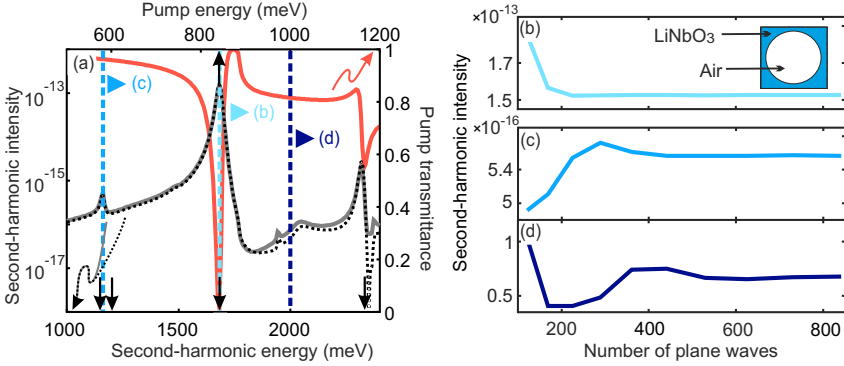


Figure 4.5: (a) Second-harmonic intensity (black line) and linear transmittance spectra (red line) of the structure presented in Fig. (4.3). The thickness of the structure is 80 nm, the period is $1.400\ \mu\text{m}$ along the x and y directions and the radius of the holes is 600 nm. (b-d) Convergence behavior of the calculated second-harmonic intensity with the pump field at (a) 842 meV (dark blue line), (b) 580 meV (blue line), and (c) 1000 meV (light blue line). The arrows in (a) denote the energies at which the convergence curves have been calculated.

with resonance energies of $842 - 8.8i$ meV, $1152 - 25i$ meV, $1183 - 40i$ meV, $1700 - 46i$ meV and $2345 - 10i$ meV. Fig. 4.5(b-d) contains the convergence behavior calculated at pump energies of (a) 842 meV (dark blue line), (b) 580 meV (blue line), and (c) 1000 meV.

4.5 Modeling of harmonic generation within the pole expansion

4.5.1 Theoretical formulation and mode matching

In the previous sections we detailed an approach to compute the radiated harmonics generated inside materials with nonlinear properties. This calculation is rather heavy and requires a lot of resources, memory and calculation time. Furthermore, we discussed in the previous chapter how efficiently the pole expansion diminishes the number of time one needs to solve Maxwell's equations to derive the optical properties of a structure for an arbitrary spectral range. Thus, it seems logic to implement an approach based on the pole expansion to calculate faster and with less resources the nonlinear response of a system over a whole spectral range. All the necessary equations for this journey have already been derived in the previous chapters, we will only stitch together the different parts of the puzzle. I will henceforth repeat some known equations to spare you the time you would need to travel back and forth in this document.

Assuming an approach based on the undepleted pump approximation, we first need to derive the electric field distribution at the pump frequency inside the structure. Let us use the Green's dyadic pole expansion that provided the best results in the chapter 3. The field inside the structure is expressed according to Eqs. (2.64) and (2.65) as

$$\underline{\mathbb{F}}_{\text{tot}}(\mathbf{r}; k) = \underline{\mathbb{F}}_{\text{BG}}(\mathbf{r}; k) - \sum_n \frac{\underline{\mathbb{F}}_n(\mathbf{r})}{k - k_n} k \mathbb{B}_V \left[\underline{\mathbb{F}}_n^{\mathbf{R}}(\mathbf{r}'); \underline{\Delta \hat{M}}(\mathbf{r}'; k) \underline{\mathbb{F}}_{\text{BG}}(\mathbf{r}'; k) \right]. \quad (4.31)$$

As in the previous section, the field derived at the pump frequency will be underlined.

The electric field at the pump frequency induces a nonlinear polarization of p^{th} -order inside the structure:

$$P^\alpha(p\omega) = 4\pi \chi^{(p), \alpha\beta_1\beta_2 \dots \beta_p}(p\omega; \omega, \omega, \dots) \underline{E}_{\beta_1}(\omega) \underline{E}_{\beta_2}(\omega) \dots \underline{E}_{\beta_p}(\omega). \quad (4.32)$$

The last step is to derive how the polarization field radiates outside the structure in the far field. The nonlinear polarization is replaced by the equivalent source current $\mathbf{j}^{\text{NL}} = \frac{-i\omega}{4\pi} \mathbf{P}$. The description of the emission of a source current within the pole expansion is described in Eqs. (2.62-2.65).

It is expressed as

$$\hat{\mathbb{M}}(\mathbf{r}; pk)\mathbb{F}(\mathbf{r}; pk) = \mathbb{J}^{\text{NL}}(\mathbf{r}; pk), \quad (4.33)$$

$$\mathbb{F}(\mathbf{r}; pk) = \int_V dV' \hat{\mathbb{G}}(\mathbf{r}, \mathbf{r}'; pk) \mathbb{J}^{\text{NL}}(\mathbf{r}'; pk). \quad (4.34)$$

In the Mittag Leffler expansion of the Green's dyadic, we assume no background field at the radiated harmonics, thus we can write:

$$\mathbb{F}_{\text{tot}}(\mathbf{r}; pk) = \sum_n \frac{\mathbb{F}_n(\mathbf{r})}{pk - k_n} \mathbb{B}_V[\mathbb{F}_n^{\mathbf{R}}(\mathbf{r}'); \mathbb{J}^{\text{NL}}(\mathbf{r}'; pk)]. \quad (4.35)$$

Even though the nonlinear polarization and the associated source current \mathbb{J}^{NL} have to be calculated at every frequency, the solution of Maxwell's equation at the pump frequency is derived using the pole expansion, thus this step is very fast. Additionally, the poles used for the Mittag-Leffler expansion of the Green's dyadic at the pump frequency are the same poles used for the expansion of the Green's dyadic at the second harmonic. Thus, the resonant modes of the structure are calculated only ones in the whole scheme and the calculation of the harmonic emission is rather fast. An analytic formulation of the field scattered at the second harmonic can be computed in the undepleted pump approximation using the nonlinear source-current:

$$\begin{aligned} \mathbb{J}_{\mathbf{E}}^{\text{NL},\alpha} = & -ik4\pi\chi^{(2),\alpha\beta\gamma} \left[\underline{E}_{\text{BG},\beta} \underline{E}_{\text{BG},\gamma} + 2\underline{E}_{\text{BG},\beta} \underline{k} \Delta\varepsilon \sum_i \frac{\underline{E}_{i,\gamma}}{k-k_i} \underline{I}_i \right. \\ & \left. + (k\Delta\varepsilon)^2 \sum_{i,j} \frac{\underline{E}_{j,\beta} \underline{E}_{i,\gamma}}{(k-k_i)(k-k_j)} \underline{I}_i \underline{I}_j \right]. \end{aligned} \quad (4.36)$$

In the latter equation, the spatial and the implicit frequency dependence have been removed to keep the formalism as simple as possible. However, though these calculations can be done in real and reciprocal space, here all the fields and susceptibility tensors are assumed to be calculated at the position \mathbf{r}' for a wave vector $k = \omega/c$. In addition, we assume $\mathbb{J}_{\mathbf{H}}^{\text{NL},\alpha} = 0$.

Thus, the total field generated at the harmonic, inside the structure, can be expressed as

$$\mathbb{F}_{\text{tot}} = \sum_n \frac{\mathbb{F}_n}{2k - k_n} (A_n + B_n + C_n), \quad (4.37)$$

with:

$$A_n = -ik4\pi\mathbb{B}_V \left[E_{n,\alpha}^{\mathbf{R}}; \chi^{(2),\alpha\beta\gamma} \underline{E}_{\text{BG},\beta} \underline{E}_{\text{BG},\gamma} \right], \quad (4.38)$$

$$B_n = -ik4\pi\mathbb{B}_V \left[E_{n,\alpha}^{\mathbf{R}}; \chi^{(2),\alpha\beta\gamma} \underline{E}_{\text{BG},\beta} \underline{k} \Delta \underline{\varepsilon} \sum_i \frac{I_i \underline{E}_{i,\gamma}}{\underline{k} - k_i} \right], \quad (4.39)$$

$$C_n = -ik4\pi\mathbb{B}_V \left[E_{n,\alpha}^{\mathbf{R}}; \chi^{(2),\alpha\beta\gamma} (k \Delta \underline{\varepsilon})^2 \sum_{i,j} \frac{I_j \underline{E}_{j,\beta} I_i \underline{E}_{i,\gamma}}{(\underline{k} - k_i)(\underline{k} - k_j)} \right], \quad (4.40)$$

where we can identify the electric field scattered inside the structure at the pump frequency as

$$\underline{E}_{\text{Scat},\beta} = \underline{k} \Delta \underline{\varepsilon} \sum_i \frac{I_i \underline{E}_{i,\gamma}}{\underline{k} - k_i}. \quad (4.41)$$

The overlap integral I_i calculated at the pump frequency is defined by Eq. (2.65). The background field propagates through the structure like if it was a homogeneous slab of material owning the permittivity of the half-space of the incoming field.

The formulation of harmonic generation within the pole expansion approach owns three different contributions A_n , B_n and C_n that we will study in more details.

Contribution A_n

The first term A_n is the result of the overlap integral between the field distribution at the resonance n and the nonlinear polarization generated by the background pump field. We can thus identify four different factors that can amplify the value of A_n and thus the frequency conversion of the background field.

1. The overlap itself between the nonlinear polarization $-ik\chi^{(2),\alpha\beta\gamma} \underline{E}_{\text{BG},\beta} \underline{E}_{\text{BG},\gamma}$ and the resonant field distribution $E_{n,\alpha}$ has to be maximum. The fulfilment of this criterion mainly depends on the symmetries of the induced nonlinear polarization and the resonant field. The background field is an incoming plane wave with a symmetric distribution. Thus, the symmetry of the nonlinear polarization field mainly depends on the symmetry of the nonlinear susceptibility tensor, which is related to the symmetry of the crystalline structure of the material. The symmetry of the field distribution at the resonance depends mainly on the type of the resonance.

2. Another criterion that quantifies the efficiency of the conversion is the near field enhancement at the resonant energy k_n . Assuming that the overlap integral is not nil, if the structure exhibit a very strong near field enhancement inside nonlinear media at the resonance n , the overlap integral of a nonlinear polarization with E_n will provide large values.
3. Then we have to account for the "distance" between the radiated frequency and the resonant frequency. In the case where the two frequencies are far from each other, the denominator $2\underline{k} - k_n$ will be large and the resonance at k_n will be only weakly excited. However, if the generated frequency is close to the resonant frequency this denominator will be small, henceforth the resonant mode n will be efficiently excited by the generated harmonic and the emission at the generated frequency will be enhanced.
4. Finally, in the case mentioned in the previous point where the harmonic is generated at the frequency of the resonant mode k_n , the real part of the distance $2\underline{k} - k_n$ will converges to 0. However, the imaginary part of k_n is not canceled. The imaginary part is inversely proportional to the quality factor of the resonance. Thus, the higher is the quality factor, the smaller will be the non-vanishing imaginary part of $2\underline{k} - k_n$ and the larger will be the enhancement.

Contribution B_n

The term B_n denotes the overlap integral between the field distribution at the resonance n and a nonlinear polarization induced by the background pump field and the field scattered by the structure at the pump frequency. As in the case of A_n , if the generated harmonic has a frequency close to a resonance of the structure the value of B_n will be larger than in the off resonant case. Thus, the overlap integral between the nonlinear polarization and the near field E_n is important and it is scaling according to the four criteria aforementioned. However, in this case, the amplitude of the nonlinear polarization itself is influenced by resonances at the pump frequency. Let us study the impact of a resonance at the pump frequency within two key points.

1. We note the presence of a factor $\underline{k}\Delta\varepsilon$ that is characteristic of the scattering occurring at the pump frequency described by Eq. (4.41). Thus, this term is scaling up the amplitude of the nonlinear polarization for lower wavelengths.

2. As in the case of the generated harmonics, if a structural resonance is excited efficiently at the pump frequency, it will dramatically increase the value of the contribution B_n . The efficiency of the excitation of the resonance at the pump frequency is calculated as the overlap integral \underline{I}_i divided by the denominator $\underline{k} - k_i$. It has to be noted that the symmetries of the resonant field \underline{E}_i and the background field strongly influence the amplitude of \underline{I}_i . In addition, the amplitude of \underline{E}_i that corresponds to the near field enhancement of the resonance k_i contributes to scaling up the nonlinear polarization as well as a high quality factor.

Contribution C_n

The term C_n denotes the overlap integral between the resonant field E_n and a nonlinear polarization induced by the scattered pump field interacting with itself. While the presence of a resonance near the frequency of the generated harmonic is still accountable, we will see here that the resonance and the near field enhancement at the pump frequency has a larger impact on the efficiency of the frequency conversion. First the nonlinear polarization expressed in C_n scales with a factor $(\underline{k}\Delta\varepsilon)^2$. Secondly, the efficiency of the excitation of the structural resonances at the pump frequency are defined by the overlap integrals $\underline{I}_i, \underline{I}_j$ and the denominator $(\underline{k} - k_i)(\underline{k} - k_j)$. Thus, the near field enhancement exhibited by \underline{E}_i and \underline{E}_j contributes to scale up the induced nonlinear polarization. We then have to distinguish two different situations:

1. Let us assume two different resonances in k_i and k_j that are excited by a pump field at a nearby frequency. The symmetry of the induced nonlinear polarization henceforth can be predicted from the symmetries of the two interacting resonant modes and the symmetry of the $\chi^{(2)}$ tensor. Thus, the geometry of the polarization field can be tailored at the condition that the two modes are excited efficiently by the pump. Thus, the nonlinear polarization scales as the product of the two near fields \underline{E}_i and \underline{E}_j . However, in this situation, none of the denominator factors $(\underline{k} - k_i)(\underline{k} - k_j)$ get close to zero so that the enhancement of the conversion efficiency is limited.
2. In the situation where the pump frequency would be close to a resonant frequency, we observed that the contribution B_n is strongly enhanced. However, the larger contribution originates from the C_n component. In this case, we have to account for the following pole

contribution in the sum calculated inside C_n :

$$C_{n,i} = -ik4\pi\mathbb{B}_V \left[E_{n,\alpha}^{\mathbf{R}}; \chi^{(2),\alpha\beta\gamma} (\underline{k}\Delta\underline{\varepsilon})^2 \frac{E_{i,\beta}^2}{(\underline{k} - k_i)^2} I_i \right]. \quad (4.42)$$

Assuming that the resonant mode at k_i exhibits a strong near field enhancement, the nonlinear response will scale up as the square of the pump field E_i . Additionally this contribution grows as the inverse of the difference $(k - k_i)^2$, which definitely enhances the signal more efficiently than the $2k - k_n$ at the generated harmonics. However, the overlap integral I_i has to be maximized thus we will see in the chapter 5 that field at the resonance needs to fulfill symmetry conditions to ensure a non-nil overlap integral with the background field.

The factor C_n is proportional to k^2 , henceforth it is obviously the predominant contribution in the case where a resonant mode is excited efficiently at the pump frequency. Though resonances at the generated harmonic are improving the conversion efficiency, it is less influential than the resonances at the pump frequency. However, the most optimized situation remains double resonant situations where the system exhibits a resonance at the pump frequency and at the second harmonic.

Finally, once the field generated at the harmonic is calculated inside the structure, we use the reciprocity principle to derive the radiated field outside the structure. We then have to compute the same overlap surface-integral as in the derivation of the transmittance and the reflectance given by Eqs. (3.31) and (3.32) that provide the radiated field outside the structure in each diffraction order as

$$\begin{aligned} \alpha_{a,\mathbf{K}}^{t/b}(2\underline{k}) &= \mathbb{B}_{\partial\nu} \left[\mathbb{I}_{a,-\mathbf{K}}^{t/b}(r; 2\underline{k}); \mathbb{F}_{\text{tot}}^{t/b}(\mathbf{r}; 2\underline{k}) \right], \\ &= \sum_n \frac{\mathbb{B}_{\partial\nu} \left[\mathbb{I}_{a,-\mathbf{K}}^{t/b}(\mathbf{r}; 2\underline{k}); \mathbb{F}_n(\mathbf{r}) \right]}{pk - k_n} (A_n + B_n + C_n), \end{aligned} \quad (4.43)$$

where the lower index a denotes the s or p polarization, \mathbf{K} denotes the diffraction order and the superscript defines if the fields are derived at the top or bottom interface.

The new overlap integral that arises Eq. (4.43) is very similar to the term I_n in Eq. (2.65). Indeed, the total field \mathbb{F}_{tot} is calculated as the superposition of the resonances of the structure, which are excited by the nonlinear source. Thus, the field emitted outside the structure is proportional to the coupling coefficient of each of these resonance with the exterior that is calculated by the means of the overlap integral $\mathbb{B}_{\partial\nu} \left[\mathbb{I}_{a,-\mathbf{K}}^{t/b}(r; 2\underline{k}); \mathbb{F}_n(\mathbf{r}) \right]$.

Finally, in this paragraph, we have been able to derive analytically the emission process taking place in a nanostructure made of materials with nonlinear properties. The equation contains in separate quantities the influence of each mode at the pump and at the generated harmonic, their quality factors and their symmetries, which are implicitly taken into account in each overlap integral.

4.5.2 Numerical analysis

Let us study the example of a dielectric slab to illustrate the calculation of higher-harmonic generation using the pole expansion approach. We will keep the parameters used in the section 3.2.2 whose structure is illustrated in Fig. 3.1. The dielectric slab is 1 μm thick and owns a refractive index of 3.5. The structure is excited by a top incoming plane wave with normal incidence and polarized along the x axis. The structure exhibits excitable Fabry Perot modes at the energies $177.1n - 33.1i$ meV with n being an integer number. For the sake of simplicity and clarity, we will assume in a first place a second order susceptibility with only one non-nil parameter $\chi^{(2),xxx} = -6.6 \cdot 10^{-9}$ cm.statV $^{-1}$.

We observe that the emission spectra owns two types of local maximum. The local maximum reached for a harmonic generation at 1594 meV corresponds to an enhanced harmonic generation with one resonant pole at the generated harmonic and no resonance at the pump frequency. On the other hand, the local maximum at 1416.8 meV marks the excitation of one resonance at the generated harmonic precisely, and one resonance at the pump frequency at 708.4 meV. We observe that the enhancement provided by the resonant pump field is much more significant than the enhancement provided by a resonance at the second harmonic. Additionally, we note that the amplitude of the double resonant peaks of emission grows faster as a function of the pump energy, than the peaks originating from simple resonances. This effect is depicted by the dark and bright green-dashed lines Fig. 4.6.

Finally, we still see a small mismatch between the direct emission scheme and the pole expansion approach. This mismatch might be due to a background contribution at the second harmonic. Such deviation can be corrected with the second harmonic generation calculated with the direct emission scheme at the higher and lower energies of the studied spectral range. Thus, from the exact calculation at two point of the spectra we can compute the error in the calculation of the electric and magnetic fields inside the structure at the second harmonic at these two frequencies. Knowing the error at these two points of the spectra, the results obtained by the

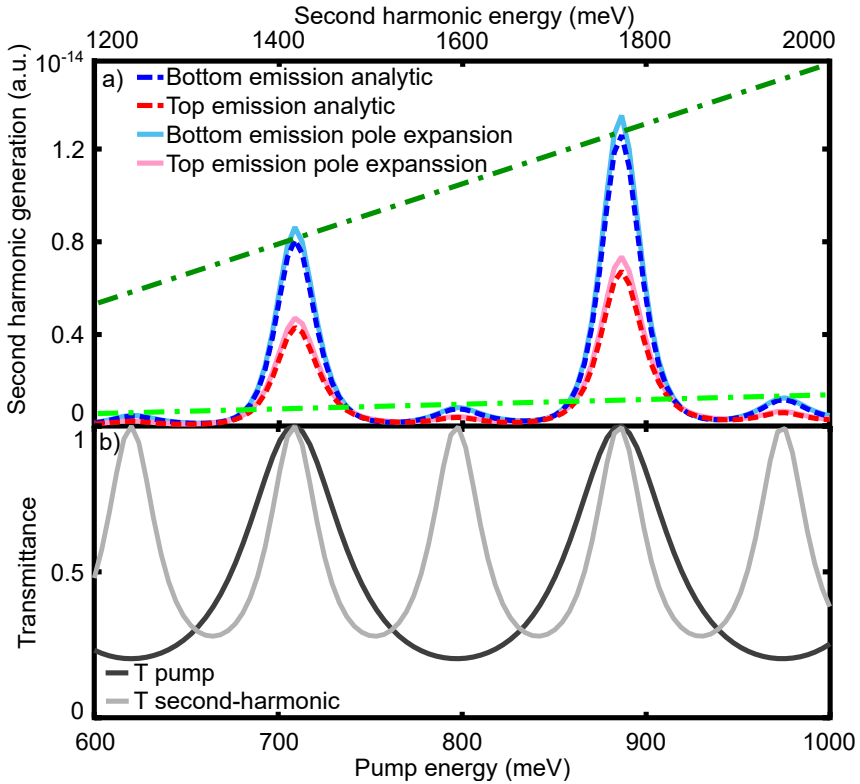


Figure 4.6: (a) Second-harmonic generated by a dielectric slab excited with a top incoming plane wave at normal incidence. The power radiated in the top and bottom half space is displayed with red and blue lines, respectively. The solid lines denote the emission calculated using the Mittag-Leffler expansion of the Green's dyadic at the second harmonic and the reciprocity principle accounting for 800 poles, the dashed lines represent the SHG computed using the direct emission scheme detailed in the previous section. The dark and bright green dashed lines schematically fit the local maxima of frequency conversion at double and single resonant working points, respectively. (b) The dark gray and light gray solid lines denote the transmittance of the slab calculated at the pump energy and the generated harmonic, respectively. The enhancement of the harmonic generation provided by the resonant poles at the pump frequency is stronger than the enhancement produced by the poles at the generated frequency.

pole expansion approach are replaced with the exact values. In addition, the correction terms are interpolated through the whole spectral range of interest. Background contributions are smooth functions and such fitting procedure is enough to provide accurate results for a minimal numerical cost.

In Fig. 4.7 is derived the second-, third- and fourth-harmonic generation within the same dielectric slab as in the Fig. 4.6. The nonlinear susceptibilities are arbitrarily chosen to be

$$\chi^{(2),xxx} = \chi^{(3),xxx} = \chi^{(2),xxxx} = -6.6 \cdot 10^{-9}. \quad (4.44)$$

The approach provided by the pole expansion provides a swift calculation of these results. We can observe that enhancement at the resonant pump frequencies is dominant in any cases. Rather small enhancements are also observable for resonances at the generated harmonics, however it is almost invisible on this figure. Finally we observe that the emitted intensity grows with the order of the nonlinear generation. It occurs because we took the same value for all the nonlinear susceptibilities in order to obtain emitted intensities in the same order of magnitude. For instance a realistic third-order nonlinear susceptibility should have a value around $3.10^{-17} \text{ cm}^2 \cdot \text{statV}^{-2}$.

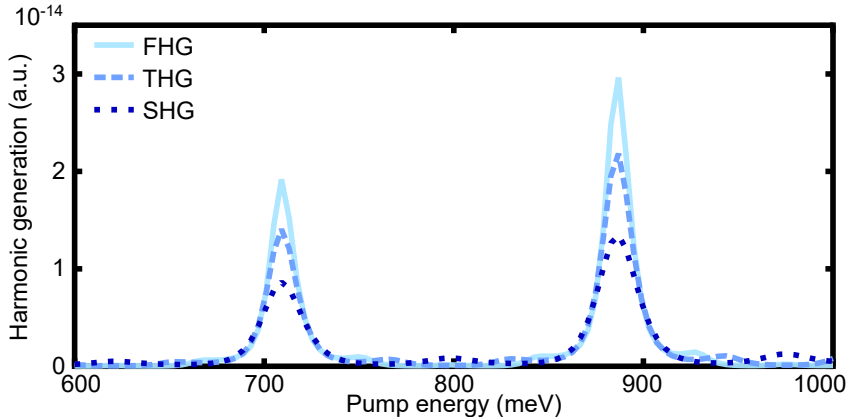


Figure 4.7: Higher harmonic generation radiated below a dielectric slab excited by a top incoming plane wave with normal incidence. The slab is $1 \mu\text{m}$ thick and own a refractive index of $n = 3.5$. The nonlinear susceptibilities assumed for this numerical example are $\chi^{(2),xxx} = \chi^{(3),xxx} = \chi^{(2),xxxx} = -6.6 \cdot 10^{-9}$. The dark-blue and blue dashed lines denotes the second- and third-harmonic generation. The light-blue solid line represents the fourth harmonic generation.

4.6 Kerr optical effect

4.6.1 Modeling of a third order nonlinear effect

One of the possible nonlinear effects we observe in dielectric as well as in metallic materials and semi-conductors is known as the Kerr optical effect. This effect is often associated to the electro-optical Kerr effect accounting for changes of refractive index as a function of an applied electrostatic field, however they should not be confused. The nonlinear optical Kerr effect is a third order nonlinearity described by the polarization vector:

$$P^{(3),\alpha}(\omega) = 4\pi 3\chi^{(3),\alpha\beta\gamma\sigma}(\omega; \omega, -\omega, \omega)E_{\beta}(\omega)E_{\gamma}(-\omega)E_{\sigma}(\omega). \quad (4.45)$$

The main components of this tensor are broadly discussed in textbooks [81], this interaction can happen in the context of material resonances or out of resonance. It is often represented as a refractive index correction:

$$n = n_0 + 2n_2|E(\omega)|^2, \quad (4.46)$$

where n_0 is the linear refractive index and n_2 is the higher order coefficient that describes the rates at which the optical refractive index changes as a function of the optical intensity.

Such effect has already been discussed in the scope of the Fourier modal method [93], where appropriate factorization rules are provided. In the following derivations, I will solve Maxwell's equations using the pole expansion and I will use the advantages provided by such scheme to account for the Kerr optical effects. In this study, we will assume the case where the phenomenon is described as a self-interaction of the field itself at the pump frequency ω . The induced nonlinear polarization will then be expressed as a source current emitting still at the frequency of the pump field. As in [93] we will use a recursive scheme to calculate the necessary corrections applied to the initial field distribution, to account for the nonlinear interaction. However, we won't solve Maxwell's equations at each step of the process, thus the shift of the resonant frequencies and the changes in the associated field distributions due to the nonlinear effect are not taken into account.

The first step of this approach is to derive the constitutive equation accounting for the third order nonlinear polarization:

$$D^{\alpha} = \varepsilon^{\alpha\tau} E_{\tau} + P^{(3),\alpha}, \quad (4.47)$$

with the nonlinear polarization given by Eq. (4.45).

The sum convention over α , β , γ and σ leads to the calculation of 81 terms in the more complicated case, which account for all the possible

combinations of the different components of the field. In addition, we have a factor 3 that accounts for all the possible permutations between the conjugated field and the two other components. However, it has been demonstrated that this expression can be simplified to the form [81]

$$\mathbf{P}^{(3)} = 4\pi \left[6\chi^{(3),1122}(\mathbf{E} \cdot \mathbf{E}^*)\mathbf{E} + 3\chi^{(3),1221}(\mathbf{E} \cdot \mathbf{E})\mathbf{E}^* \right], \quad (4.48)$$

where all the fields are ω dependent and \mathbf{E}^* denotes the complex conjugate of \mathbf{E} . Thus, the nonlinear polarization is split into two contributions driven by $\chi^{(3),1122}$ and $\chi^{(3),1221}$. The advantage of this formulation is that $\chi^{(3),1122}$ and $\chi^{(3),1221}$ are scalars, thus we do not need to account for the full convolution of the fields with the nonlinear susceptibility, we only need to consider the two scalar products over the field components in Eq. (4.48). Then, we can derive the equivalent source current as 4π times the time derivative of the nonlinear polarization. The latter source current will henceforth generate another electromagnetic field at the pump frequency that we will have to account for, as a correction of the initial field. Then we will have to reiterate the procedure until the correction term becomes small enough to be neglected. It is to be noted that we account for the emission of a field at the pump frequency in addition to the initial pump field that propagated from the far field inside the structure. Thus, this approach violate the conservation of energy, in that sense we are doing an approximation.

Let us call $\mathbf{E}^{[0]}$ the initial field induced in the system without correction, we will then call $\mathbf{E}^{[j]}$ the field correction calculated at the j^{th} recursive step. It is then appropriate to rewrite the constitutive equation accounting for the total field with all the correction terms.

$$\begin{aligned} \mathbf{D} = \varepsilon \sum_l \mathbf{E}^{[l]} &+ 4\pi 6\chi^{(3),1122} \left[\sum_j \mathbf{E}^{[j]} \cdot \sum_k (\mathbf{E}^{[k]})^* \right] \sum_l \mathbf{E}^{[l]} \\ &+ 4\pi 3\chi^{(3),1221} \left[\sum_j \mathbf{E}^{[j]} \cdot \sum_k \mathbf{E}^{[k]} \right] \sum_l (\mathbf{E}^{[l]})^*. \end{aligned} \quad (4.49)$$

We observe that each nonlinear susceptibility tensor is multiplied by the product of three sums that account for the nonlinear polarization induced by each field correction. In addition cross terms appear. They account for the interaction of the j^{th} field correction with the pump field and all the other corrections calculated in the previous recursive steps. This scheme provides a consistent approach on how to compute the nonlinear polarization without violating the constitutive equation. In a first place, we will study the calculation of the nonlinear polarization induced by $\chi^{(3),1122}$.

We assume that this nonlinear susceptibility induces at each correction step a nonlinear polarization $\mathbf{P}_{1122}^{(3)[j]}$, which generates the correction field of the next iteration $\mathbf{E}^{[j]}$. For instance:

$$\mathbf{P}_{1122}^{(3)[1]} = 4\pi 6\chi^{(3),1122} \left[\mathbf{E}^{[0]} \cdot (\mathbf{E}^{[0]})^* \right] \mathbf{E}^{[0]}, \quad (4.50)$$

$$\begin{aligned} \mathbf{P}_{1122}^{(3)[2]} = 4\pi 6\chi^{(3),1122} \left\{ \right. & \left[\mathbf{E}^{[0]} \cdot (\mathbf{E}^{[0]})^* \right] \mathbf{E}^{[1]} \\ & + \left[\mathbf{E}^{[0]} \cdot (\mathbf{E}^{[1]})^* + \mathbf{E}^{[1]} \cdot (\mathbf{E}^{[0]})^* \right] (\mathbf{E}^{[0]} + \mathbf{E}^{[1]}) \\ & \left. + \left[\mathbf{E}^{[1]} \cdot (\mathbf{E}^{[1]})^* \right] (\mathbf{E}^{[0]} + \mathbf{E}^{[1]}) \right\}. \end{aligned} \quad (4.51)$$

Before defining the general form of $\mathbf{P}^{(3)[j]}$, let us define a new factor:

$$\begin{aligned} (\chi^{(3),1122})^{[j]} = 6\chi^{(3),1122} \left\{ \right. & \left(\sum_{p=0}^{j-1} \mathbf{E}^{[p]} \right) \cdot (\mathbf{E}^{[j]})^* + \mathbf{E}^{[j]} \cdot \left[\sum_{p=0}^{j-1} (\mathbf{E}^{[p]})^* \right] \\ & \left. + 6\chi^{(3),1122} \left[\mathbf{E}^{[j]} \cdot (\mathbf{E}^{[j]})^* \right] \right\}. \end{aligned} \quad (4.52)$$

It is then possible to derive a nonlinear polarization vector that takes into account each of the previous field correction due to $\chi^{(3),1122}$ and preserve the constitutive equation:

$$\mathbf{P}_{1122}^{(3)[j+1]} = \sum_{p=0}^j (\chi^{(3),1122})^{[p]} \mathbf{E}^{[p]} + (\chi^{(3),1122})^{[j]} \sum_{p=0}^{j-1} \mathbf{E}^{[p]}. \quad (4.53)$$

Similar derivations lead to the definition of the coefficient:

$$\begin{aligned} (\chi^{(3),1221})^{[j]} = 3\chi^{(3),1221} \left\{ \right. & \left(\sum_{p=0}^{j-1} \mathbf{E}^{[p]} \right) \cdot \mathbf{E}^{[j]} + \mathbf{E}^{[j]} \cdot \left[\sum_{p=0}^{j-1} \mathbf{E}^{[p]} \right] \\ & \left. + 6\chi^{(3),1221} \left[\mathbf{E}^{[j]} \cdot \mathbf{E}^{[j]} \right] \right\}. \end{aligned} \quad (4.54)$$

The latter term is used in the definition of $\mathbf{P}_{1221}^{(3)[j]}$:

$$\mathbf{P}_{1221}^{(3)[j+1]} = \sum_{p=0}^j (\chi^{(3),1221})^{[p]} (\mathbf{E}^{[p]})^* + (\chi^{(3),1221})^{[j]} \sum_{p=0}^{j-1} (\mathbf{E}^{[p]})^*. \quad (4.55)$$

Thus, the total nonlinear polarization induced by an infinity of corrections yields:

$$\mathbf{P}^{(3)} = \sum_{i=1}^{\infty} \left(\mathbf{P}_{1122}^{(3)[i]} + \mathbf{P}_{1221}^{(3)[i]} \right). \quad (4.56)$$

One can verify that the field correction $\mathbf{E}^{[j]}$ is proportional to $\chi^{(3)}$ to the power $n - 1$. Assuming that $\chi^{(3)}$ is of the order of $10^{-17} \text{ cm}^2/\text{statV}^2$ [81], the largest value contributing to the nonlinear polarization is $\mathbf{E}^{[0]}$. Thus, the dominant contribution inside each corrective nonlinear-polarization $\mathbf{P}^{(3)[j]}$ will be the cross terms:

$$\chi^{(3),1122} \left[\mathbf{E}^{[0]} \cdot (\mathbf{E}^{[0]})^* \right] \mathbf{E}^{[j]} = (\chi^{(3),1122})^{[1]} \mathbf{E}^{[j]}, \quad (4.57)$$

$$\chi^{(3),1221} \left[\mathbf{E}^{[0]} \cdot \mathbf{E}^{[0]} \right] (\mathbf{E}^{[j]})^* = (\chi^{(3),1221})^{[1]} (\mathbf{E}^{[j]})^*. \quad (4.58)$$

This approach will be used in the next part to account for the optical Kerr effect inside layered structures.

Though we decided in this chapter to use rather simple approaches to demonstrate the efficiency of the pole expansion approach to derive solutions of Maxwell's equations, it is clearly possible to improve these approaches beyond the current approximations. In the case of harmonic generation, the implementation of a recursive scheme such as the scheme used for the optical Kerr effect, could account for a back interaction between the generated field and the pump (for instance $\chi^{(2)}(\omega; 2\omega, -\omega)$ and $\chi^{(2)}(3\omega; 2\omega, \omega)$). In addition, we could also consider other generated frequencies such as the third harmonic in the case $\chi^{(2)}(3\omega; \omega, 2\omega)$. Moreover, another description of the optical Kerr effect is obtained while introducing the nonlinear polarization as a correction of the refractive index. Using this type of approach, we might be able to account for the conservation of energy during the nonlinear process. However, one needs to solve Maxwell's equations for the new refractive index distribution, at each correction step. However, it is known that fast and efficient approaches based on the pole expansion of the Green's dyadic called *resonant state expansion* are able to predict the shift of resonances induced by structural perturbations without solving Maxwell's equations [44, 71, 94]. Thus, the current approach could be improved without increasing much the numerical cost by using the resonant state expansion to predict the changes induced by the modifications of refractive index at each correction step.

4.6.2 Numerical example

We consider as a test structure, the U-shaped metallic grating depicted Fig. 4.8 (a) and in [93]. The structure is $d_x = 1 \text{ }\mu\text{m}$ periodic and the grooves are $h = 494 \text{ nm}$ deep by $w = 0.5 \text{ }\mu\text{m}$ large. The structure is mainly made of silver, the grooves are filled with a dielectric material, the superstrate is assumed to be air and the substrate is silver. The permit-

tivity of silver is derived using the drude model:

$$\varepsilon = \varepsilon_\infty - \frac{\omega_p^2}{\omega(\omega + i\omega_\gamma)}. \quad (4.59)$$

In the linear spectra displayed in Fig. 4.8, we assume the properties of silver to be: $\varepsilon_\infty = 5$, $\omega_p = 1.355 \cdot 10^{16} \text{ s}^{-1}$ (0.139 μm) and $\omega_\gamma = 3.425 \cdot 10^{13} \text{ s}^{-1}$ (55 μm). The refractive index of air and the permittivity of the dielectric material are respectively, $n = 1$ and $\varepsilon_d = 12.04$. We assume the nonlinear susceptibility of the dielectric material to be $\chi^{(3),1221} = 10^{-6} \text{ cm}^2 \cdot \text{statV}^{-2}$ that is two orders of magnitude higher than the third-order nonlinear susceptibility of Si near its absorption band at 1170 meV [93, 95]. The nonlinear susceptibility is defined with a value much higher than a regular third-order nonlinear term to test our algorithm as it has been done in other works[93]. In the linear spectra Fig. 4.8, we observe that the structure posses two resonances at $786 - 3i$ meV and $806 - 12i$ meV. Exciting the structure near these resonances will provide a near field enhancement that will require us to account for the Kerr optical effect. Thus, we compute the field emitted by the dielectric material at the pump frequency. The emission is calculated with the pole expansion approach Eq. (4.35) assuming the source term $-i\omega\mathbf{P}$ derived from Eq. (4.56).

The field distribution accounting for the optical Kerr effect is calculated using the pole expansion of the Green's dyadic at 785 meV and 806 meV. The fields are obtained by calculating numerically the contribution of the poles denoted by a solid black arrows at $786 - 3i$ meV and $806 - 12i$ and the background field at the position of the gray arrows at 700 meV and 900 meV in Fig. 4.8 (a). The field distributions at the resonance and the background corrections are derived using a reciprocal space with 61 plane waves.

In Fig. 4.9 the field distributions derived in the top and bottom row respectively at 785 meV and 806 meV account for the optical Kerr effect in the right column Fig. 4.9 (b,d) while the field distributions of the pump field without corrections are displayed in the left column panels (a,c). The fields are calculated for an incoming plane wave with normal incidence and an amplitude of $|E_{pump}| = 6.5 \text{ statV/cm}$. We observe that the corrections accounting for the Kerr optical effect at 785 meV result in differences between the field distribution displayed in Fig. 4.9 (a) and (b). More precisely, at the top of the dip (near $z = 0 \mu\text{m}$) and in the center of the lower part ($x = 0.5 \mu\text{m}$ & $z > 0.4 \mu\text{m}$) the nonlinear phenomenon decreased the field amplitude while it amplified the near field amplitude in the two bottom corners of the dip ($z = 0.495 \mu\text{m}$ & $x = 0.25$ and $0.75 \mu\text{m}$).

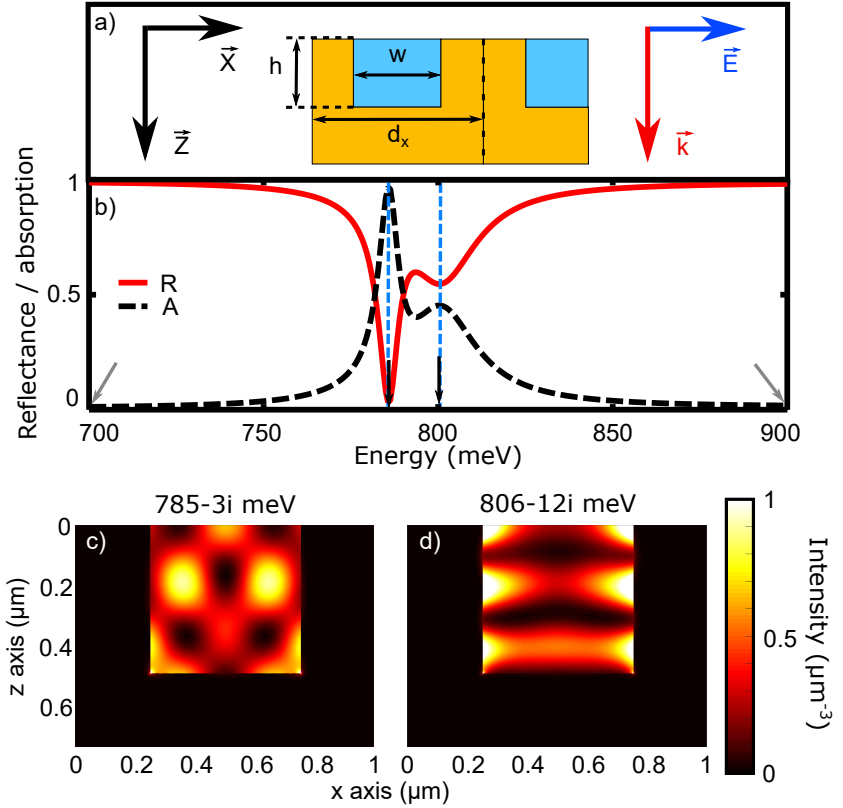


Figure 4.8: (a) This scheme represents a one-dimensional grating made of silver with grooves filled with a dielectric material owning nonlinear properties and a superstrate made of air [93]. The structure is $d_x = 1\text{ }\mu\text{m}$ periodic, the grooves are $h = 494\text{ nm}$ deep and $w = 0.5\text{ }\mu\text{m}$ large and the substrate is 247 nm thick. The permittivity of the metal is derived using the Drude model with $\lambda_p = 0.139\text{ }\mu\text{m}$, $\lambda_\gamma = 55\text{ }\mu\text{m}$ and $\epsilon_\infty = 5$. The permittivity of the dielectric material is $\epsilon_d = 12.04$ and the refractive index of the superstrate is $n = 1$. The nonlinear susceptibility of the dielectric is assumed to be $\chi^{(3),1221} = 10^{-6}\text{ cm}^2 \cdot \text{statV}^{-2}$. The structure is excited by a plane wave with normal incidence polarized along x . (b) In this panel we display the reflectance and absorption spectra of the structure as a function of the wavelength. In this spectral range the structure possesses two resonant wavelengths denoted by black arrows at $786 - 3i$ meV and $806 - 12i$ meV. The field calculation based on the Mittag Leffler expansion is carried out at the energies 785 meV and 806 meV denoted by blue dashed lines, while the background field is fitted at the position of the gray arrows at 700 meV and 900 meV . In panels (c) and (d) are displayed the intensity distribution of the resonances at $786 - 3i$ meV and $806 - 12i$ meV, respectively.

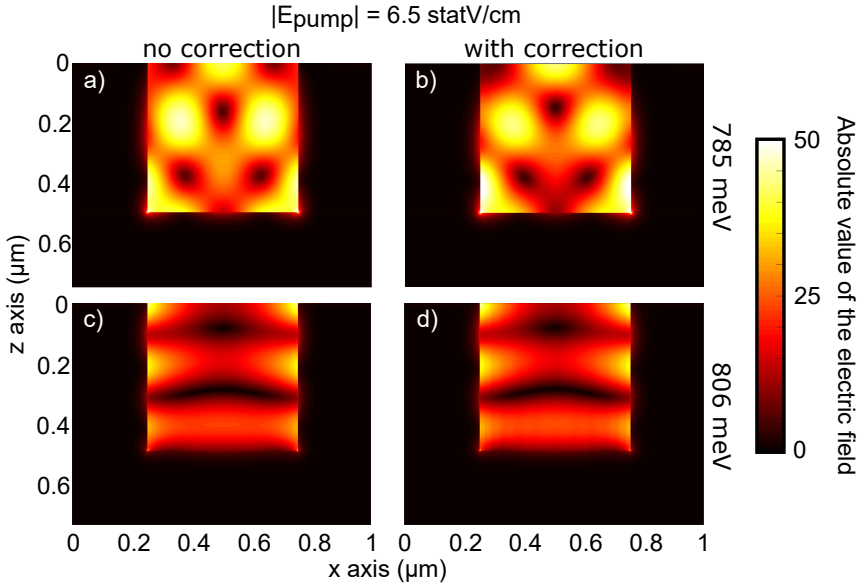


Figure 4.9: In the top and bottom rows are displayed the absolute value of the electric fields inside the structure at 785 meV and 806 meV, respectively. All the fields are derived assuming an incoming field with normal incidence and with an amplitude of 6.5 statV/cm. In the left column is displayed the electric field calculated using the Fourier modal method without accounting for the Kerr optical effect. In the right column is displayed the field calculated using the pole expansion of the Green's dyadic accounting for the Kerr optical phenomenon.

However, accounting for nonlinear Kerr effect at 806 meV produces almost no changes between Figs. 4.9 (c) and (d). On the one hand, we observe Fig. 4.9 (c) and (d) that the resonance at 806 meV is inducing a near field enhancement nearly 1.5 times stronger than the enhancement induced by the resonance at 786 meV. On the other hand, the linewidth of the resonance at 786 meV is 4 times smaller than the linewidth of the resonance at 806 meV. Referring to Eq. (4.36), we observe that in this situation the narrow resonance exhibits stronger nonlinearities than the resonance with the strongest near field enhancement. This observation is interesting, though it might not be true in all situations and there might be cases where the near field enhancement becomes more important than the linewidth of the excited resonances.

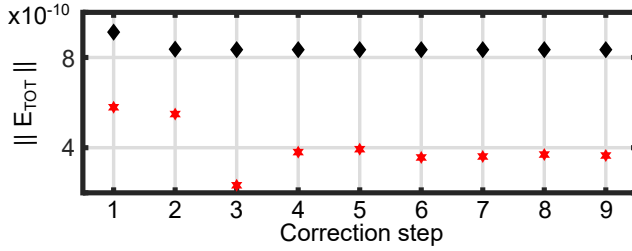


Figure 4.10: The markers denotes the L^2 norm of the total field after j correction steps. The red and black markers denote the convergences of the total field at 785 meV and 806 meV, respectively. The convergence diagram is calculated for an incoming field of amplitude $|E_{pump}| = 6.5$ statV/cm.

In such numerical calculations, it is possible in the case of intense incoming fields that the corrections accounting for nonlinear phenomenon do not converge and provide a total field with a higher and higher amplitude. Thus, we calculated the L^2 norm of the total electric field, in the case of the calculations in Fig. 4.9 (b,d). The L^2 norm is calculated as the integral of the squared absolute value of the electric field in one unit cell. The integration is carried out for one period of the structure (1 μm) in x direction and through the thicknesses of the grating (495 nm) and the substrate (247 nm) in z direction:

$$\|E_\alpha\| = \int dx dz |E_\alpha|^2. \quad (4.60)$$

The calculation is done for the total electric field at each correction step $j > 0$. As we can observe, the L^2 norm of the total electric field converges, which ensure the quality of the results displayed Fig. 4.9.

Finally, we have to note that the near field enhancement observed Fig. 4.9 leads to self-focusing. In the case of large intensities, solving Maxwell's equations at each step would lead the reduction of the size of the hot-spots. At the same time, the amplitude of the field locally increases that enhances further the nonlinear interaction. This effect can damage the structure in the case of filament propagation. In such situation, the numerical scheme provided would not converge and additional phenomena as thermal effects should be considered.

In this section, we provided a new method to account for the Kerr optical effect inside nanostructures. This nonlinear phenomenon is described by attributing a $\chi^{(3)}$ tensor to the medium that possesses nonlinear properties. In the next chapter, we will see that third order nonlinear phenomena that are described by the $\chi^{(3)}$ tensor can also generate third harmonics inside metallic nanostructures. However, in the next chapter the third harmonic generation inside plasmonic systems will be derived using reciprocity principal as explained in the section 4.3.2.

5 Experimental and numerical study of third-harmonic generation

What we observe is not nature itself, but nature exposed to our method of questioning.

Werner Heisenberg (1901-1976)

5.1 Nonlinear optics within chiral systems

5.1.1 Linear and nonlinear circular dichroism

Chirality is a property that characterizes objects lacking any kind of mirror symmetry. For instance the left and right hands of a human are chiral. Indeed they are the mirror projection of each other, however they cannot be superposed perfectly no matter how you turn them. The two versions of an object owning a chiral geometry are called enantiomorphs or enantiomers in the case of molecules. In a Cartesian coordinate system the 3 basis vectors form a chiral object, indeed once the x and y axis are defined the z axis can be oriented along two possible directions that refers to two different basis that are the mirror symmetric of each other. These two basis cannot be superposed and are called right- and left-handed basis (see Fig. 6.1).



Figure 5.1: Representations of a Cartesian right-handed basis (a) as well as a left-handed basis (b).

The choice of a left- or right-handed vector basis defines the orientation of the vector product, henceforth the vector product and thus the curl operator can be used to discriminate the two different types of handedness inside one coordinate system.

Beyond the mathematical facts and the observation of macroscopic chiral objects, chirality is widely present in nature at nano- and microscopic scales. A large amount of molecules are chiral and probing the handedness of molecular species is a broad topic of research. Probing the handedness of a chiral object requires a chiral probe. In this aspect, optical radiations are highly interesting since the left- and right-circular polarization states of light are chiral. Thus, so called chiroptical effects can occur through light-matter interactions. Though linear light-matter interactions can be described using the harmonic oscillator model, chiroptical effects have to be described using the coupled oscillator model. Thus, we can consider a system of two oscillators interacting with each other as illustrated in

Fig. 5.2.

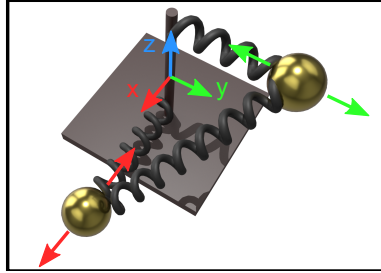


Figure 5.2: Illustration of a coupled oscillator system made of two mechanic oscillators. Each mechanic oscillator is constituted of a mass oscillating at the extremity of a spring. Each mass is moving along the axis of the corresponding spring, thus the two masses are oscillating in perpendicular directions. The coupling between the oscillators is modeled with a third spring.

This model leads to the Drude-Born-Fedorov constitutive equations for reciprocal chiral media [96]:

$$\mathbf{D} = 4\pi\epsilon_c\mathbf{E} + \Gamma \nabla \times \mathbf{E}, \quad (5.1)$$

$$\mathbf{B} = 4\pi\mu_c\mathbf{H} + \frac{\mu_c}{\epsilon_c}\Gamma \nabla \times \mathbf{H}. \quad (5.2)$$

μ_c and ϵ_c are quantities that are derived from the coupled oscillator model and approximate the dielectric permittivity and magnetic permeability in the same fashion as the Lorentz model does for a single harmonic oscillator. Γ represents the chiral response of the medium, even though in specific cases the permittivity ϵ_c derived from the coupled oscillator model can depend on the chiral properties of the medium as well. These equations can be however reduced to the simpler constitutive equations (2.20) and (2.21) given in chapter 2 [97].

It has been shown that plasmonic nanoparticles with specific shapes can exhibit chiroptical effects that are orders of magnitude higher than in bio-molecules [98–103]. Additionally, such plasmonic structures can be used to strongly enhance the chiral response of molecules [104, 105]. Thus, plasmonic structures provide an efficient method to analyze the chirality of biological and chemical objects. In this section we will focus on circular dichroism spectroscopy that is a well-known method to detect the chiroptical phenomenon. The circular dichroism of a medium is usually calculated as the difference of absorption spectra between left- and right-

circularly polarized light:

$$CD = A_{LCP} - A_{RCP}. \quad (5.3)$$

In the case of nano-structures made of materials with nonlinear properties capable of radiating pump harmonics, one can define a nonlinear circular-dichroism for the generated harmonic. It is the relative difference of intensity emitted in each circular polarization-state:

$$CD^{NL} = \frac{I_{LCP}^{NL} - I_{RCP}^{NL}}{I_{LCP}^{NL} + I_{RCP}^{NL}}. \quad (5.4)$$

Previous research work demonstrated that even though the intensity detected at the generated harmonic is weak, the nonlinear circular dichroism (calculated as a relative strength) is stronger than the linear circular dichroism [106–108]. The previous work mainly aimed for second-harmonic chiroptical effects, however SHG inside gold nanoparticles takes place at the interfaces and thus suffer from surface defects. Additionally, this type of harmonic generation requires non centro-symmetric systems henceforth it is extremely sensitive to the geometry of the metallic nanostructures. In this context experimental measurements of the circular dichroism of emitted second-harmonics are challenging because any small imperfection in the fabrication process will have dramatic consequences.

5.1.2 Numerical model and experiment

In this section, we will use the reciprocity principle to calculate the circular dichroism of third-harmonic radiations emitted inside plasmonic structures with a C_4 symmetry. The result of the calculation will be compared with experimental results, indeed, the third harmonic generation is a volumetric process less sensitive to structural imperfections, which is a strong advantage from an experimental perspective.

Before describing the complete structure that has a rather complicated geometry, let us shortly present the Born-Kuhn plasmonic analog [34]. The left-handed and right-handed versions of the Born-Kuhn plasmonic structures are built as the superposition of two metallic nano-rods (see Fig. 5.3) that behave as two coupled oscillators.

Individually each rod is designed to exhibit a fundamental resonance around the wavelength λ_0 , however the two rods are close enough to couple through their near fields. Hence, we can observe a splitting of the resonance into two hybrid resonant modes located symmetrically around the original resonance of the single rod. The two hybrid resonances are often referred to as bonding and anti-bonding modes, which are illustrated in Fig. 5.3 panels

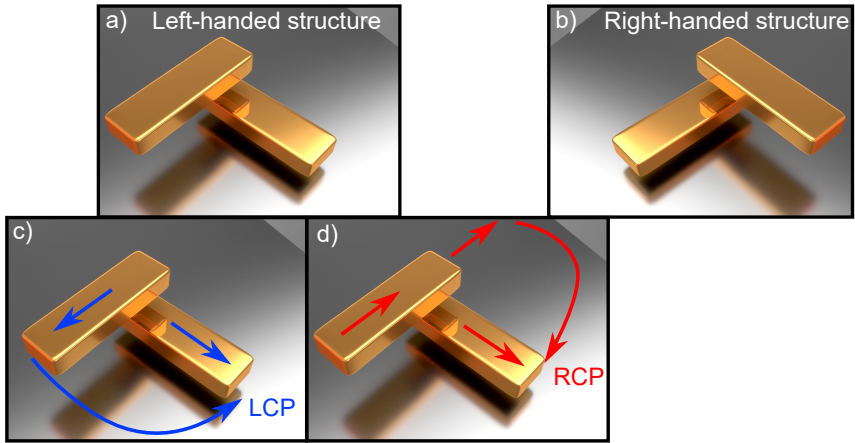


Figure 5.3: Panels (a) and (b) are illustrating left-handed and right-handed gold nanostructures exhibiting the chiroptical properties predicted by the Born-Kuhn coupled oscillator model. In panel (c) is represented the anti-bonding mode of a left handed structure excited by an incoming left handed circular polarized radiation. The blue arrows represent the dipolar moment induced in each gold nano rod for an anti-bonding mode. (d) Representation of a bonding mode in a left handed structure excited by right circularly polarized light. The red arrows denote the induced moment of each rod for a bonding mode.

(c) and (d). The symmetric bonding mode has a lower energy than the anti-bonding mode that exhibits an anti-symmetric distribution of charge and thus store an additional load of electrostatic energy. Furthermore, the bonding mode of a chiral structure is excited by radiations with a circular polarization of opposite handedness while the anti-bonding mode is excited with a circular polarization of same handedness as illustrated Fig. 5.3.

The experimental structure has been arranged in a lattice with C_4 symmetry [6] as illustrated Fig. (5.4). The left- and right-handed circular polarization states are eigen-polarizations of systems with C_4 symmetry. Incoming electromagnetic radiations polarized with an eigen-polarization state keep their polarization unchanged while propagating through the structure. Hence, no polarization conversion occurs, which prove to be convenient in the measurement of circular dichroism and thus the detection of the chiroptical phenomenon.

In an experimental structure with such properties, each unit cell contains 4 corner stack Born-Kuhn analogs of same handedness. The metallic nano rods are made of gold embedded inside a dielectric material (IC1-200).

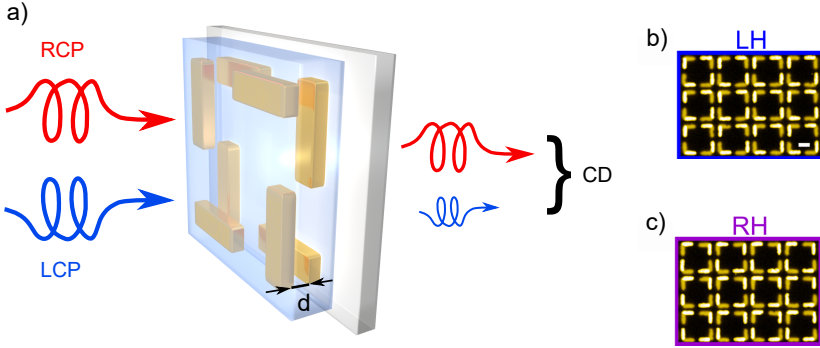


Figure 5.4: (a) Design of a bi-layer containing corner stacked Born-Kuhn analogs arranged with a C_4 symmetry. The CD spectra of the structure is computed by detecting the difference of the absorption calculated for the two circular polarizations. In (b) and (c) are the SEM images of left- and right-handed enantiomers, in (b) is inserted a scale bar of 200 nm. (Reprinted with permission from [6]. Copyright (2019) American Chemical Society. Only the panels (b) and (c) are from the original print.)

The system is printed on top of a substrate of glass. The refractive index of IC1-200 and glass are assumed to be 1.3 and 1.46, respectively. The dielectric permittivity of gold is calculated using the critical point model [73]. The structure has a periodicity of 600 nm, each rod has a length of 200 nm, a width of 70 nm and a thickness of 40 nm. The spacer layer in between the gold nanorods is $d = 110$ nm thick.

The structure is excited by a top incoming plane wave with normal incidence and either a left- or right circular polarization. Using the algorithm based on the S-matrix approach described section 2.7 [68, 69], we identify the bonding and anti-bonding modes at respectively $1110 - 48i$ meV (1116 nm) and $1160 - 17i$ meV (1070 nm).

The third harmonic generation is numerically calculated in three steps. First the field distribution of the pump field inside the structure is calculated using the Fourier modal method. For this simulation, the structure is modeled using a spatial sampling $N_x = 2048$ in real space and 43×43 Fourier harmonics in the reciprocal space.

In a second step, we use the anharmonic oscillator approach [81] to define the third-order nonlinear susceptibility of gold that we multiply with the pump field to obtain the induced nonlinear polarization field in

real space as derived in Eqs. (4.2) and (4.3). As discussed in the previous chapters, the nonlinear polarization behaves as a source current at the third harmonic. Thus in a third step, we finally use the volumetric form of the reciprocity principle as in the section 4.3.2. We calculate the near field generated by s- and p- polarized plane waves incoming from the far field at the third harmonic frequency. The overlap integral of the latter fields with the volumetric nonlinear source provides the third harmonic radiated into the far field with s- and p-polarization. Obviously, the s- and p-polarized states are chosen as a basis for convenience but the polarization basis defined with the two circular polarization could have been chosen too.

While it is possible to model the linear properties of the full structure with the coupled oscillator model, it has been shown that the nonlinear properties can be modeled with a similar approach. The parameters of the linear system are defined using a fit of the linear spectra experimentally measured on the structure. By the mean of perturbations in the coupled equations describing the system, it is possible to derive a source term that describes the harmonic generation inside the structure [6]. The results of this method are given side by side with the experimental results and the full wave simulation figures 5.5 and 5.6.

The numerical results and the experimental measurements reveal in a first place that a circularly polarized pump generates a third harmonic with the opposite handedness. This polarization conversion occurs during the harmonic generation. It is due to the symmetry of the structure [109]. This conversion can be understood intuitively calculating the nonlinear polarization vector using the anharmonic oscillator model for the third-order nonlinear susceptibility and the Jones vector of the electric field. Owing to the eigen-polarization states of the structure, we know that the field inside the structure will be left- or right-handed circularly polarized and thus in the first case the nonlinear polarization reads:

$$\mathbf{P}^{(3)}(3\omega) \propto \chi^{(1)}(3\omega) \left[\chi^{(1)}(\omega) \begin{pmatrix} 1 \\ i \\ 0 \end{pmatrix} \right]^3. \quad (5.5)$$

We see immediately that the induced nonlinear polarization has the opposite handedness $\mathbf{P}^{(3)} \propto (-i, 1, 0)$ of the pump field. Hence the third harmonic is polarized accordingly in the simple situation where anharmonic oscillator model can be used to determine the nonlinear susceptibility [87].

Left-handed and right-handed structures display similar behaviors plotted in figures (5.5) and (5.6). The black solid lines in panels (a,d,g) denote the extinction factor for left-circularly polarized incoming light, the panels (b,e,h) denote, in black, the linear response for right-circular polarized ex-

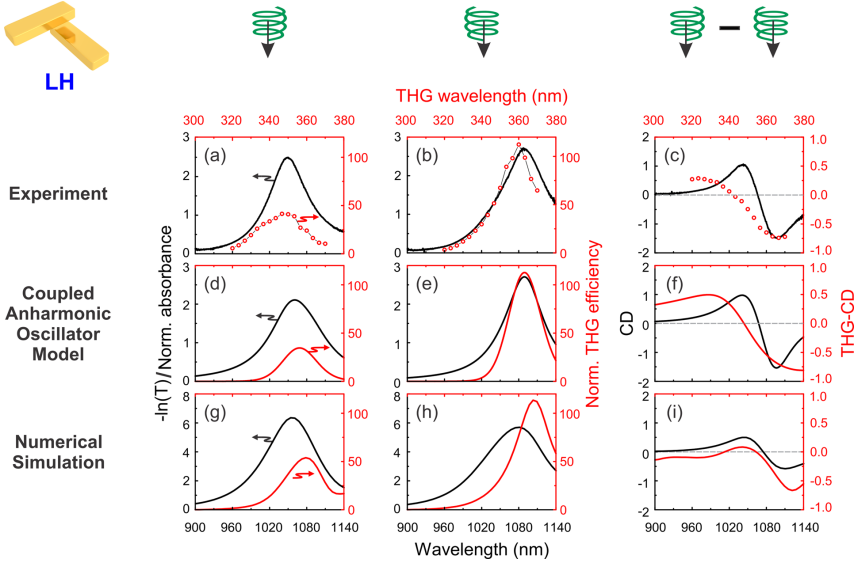


Figure 5.5: Measured (top row), modeled (middle row) and simulated (bottom row) linear (black) and nonlinear (red) chiroptical response of the left-handed enantiomer. The extinction defined as the negative logarithm of transmittance $-\ln(T)$ and the THG efficiency are displayed in (a), (d) and (g) for LCP and (b), (e) and (h) for RCP excitation schemes, and yield the CD and THG-CD shown in (c), (f) and (i). (Reprinted with permission from [6]. Copyright (2019) American Chemical Society.)

citation. We observe that the two polarization states excite two different resonant modes as expected. These modes are located at the maximums of linear extinction displayed in each panel. The circular dichroism, in this example, is calculated as the difference of the extinction for each incoming circular polarization ($CD = -\ln(T_{LCP}) + \ln(T_{RCP})$), which is plotted in panels (c), (f) and (i). We can observe in the linear CD response the fingerprint of chiroptical effects denoted by a local minimum followed by a local maximum.

The nonlinear response displays a similar behavior. The emission at the third harmonic for each handedness of incoming pump is displayed whether with red points in panels (a), (b) for the experiment or a red solid lines panels (d), (e) for the model and (g), (h) for the simulation. It occurs that the resonant modes excited at the pump frequency, in each case, produce an enhancement of the harmonic conversion process as we could expect from the pole expansion approach detailed in chapter 4. For

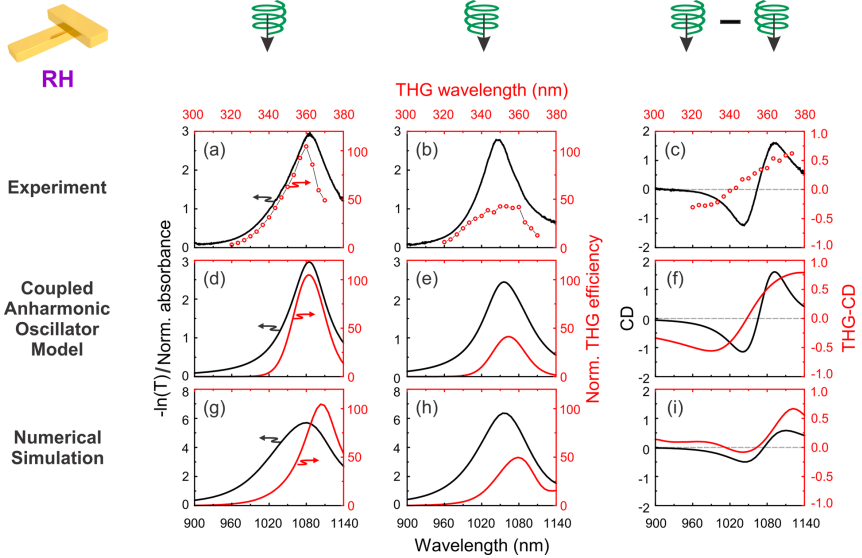


Figure 5.6: Measured (top row), modeled (middle row) and simulated (bottom row) linear (black) and nonlinear (red) chiroptical response of the right-handed enantiomer. The extinction defined as the negative logarithm of transmittance $-\ln(T)$ and the THG efficiency are displayed in (a), (d) and (g) for LCP and (b), (e) and (h) for RCP excitation schemes, and yield the CD and THG-CD shown in (c), (f) and (i). (Reprinted with permission from [6]. Copyright (2019) American Chemical Society.)

instance, in the left handed structure in Fig. 5.5 the maximum of THG will occur at three times the frequency of the bonding or anti-bonding mode, respectively for right- and left-handed circularly polarized pump fields. The nonlinear CD-spectra is displayed panels (c), (f) and (i) with red points and red solid lines for the experimental measurement, the model and the simulation, respectively. We observe that the relative nonlinear circular-dichroism expressed by Eq. (5.4) displays a similar fingerprint as the linear CD-spectra, which was expected from the position of the peak of nonlinear emission at the position of the bonding and anti-bonding modes.

The simulation displays slightly broader extinction peaks than the peaks measured experimentally. It might be due to the difference between the perfect nano-rods of the model and the imperfect rods printed for the experiment. This difference would yield different coupling constants and then different damping rates for the bonding and anti-bonding modes of the experiment and the simulation. Additionally, we observe that the peak of

nonlinear emission calculated in our simulation is red-shifted compared to the experiment. This behavior is due to the fact that the maximum of near field enhancement that strongly influence the harmonic generation occurs at lower energies (larger wavelength) than the far field enhancement [110]. Thus, the shifted near field enhancement might be stronger in the case of the simulated perfect structure than the imperfect experimental structure, which then would display a better efficiency at shorter wavelength.

Besides the small mismatch discussed above, the numerical simulations display a good agreement with the experiment and the model being able to reproduce the chiroptical effect at the third harmonic using rather simple assumptions such as the anharmonic oscillator model for the nonlinear susceptibility. In addition, one should note that using 43×43 harmonics for the numerical simulation generates gigantic matrices that are more difficult to invert numerically and push the model close to its limit. In the next chapter we will study a simpler structure that still undergoes mode hybridization as the Born-Kuhn plasmonic analog and exhibits a rather singular harmonic-conversion mechanic very different from the nonlinear chiroptical phenomenon.

5.2 Influence of symmetry breaking on the third-harmonic generation

5.2.1 Electromagnetically induced absorption

We observed in the previous section that the hybridization of two modes can trigger interesting phenomena such as chiroptical effects. The third harmonic has proven to exhibit a circular dichroism whose amplitude calculated relatively to the total field amplitude is higher than the relative circular dichroism of the linear signal. However, such measurements require very sensitive sensors at the third harmonic frequency. Indeed, in the situation where the plasmonic structure is not designed appropriately, the nonlinear harmonic generation is weak.

In this section, we aim to design a plasmonic structure that would exhibit an enhanced third-harmonic conversion efficiency. From the pole expansion approach providing Eq. (4.37), we observed that a pump frequency close to a resonant mode exhibits a high harmonic conversion efficiency. The generated intensity scales with the quality factor of the resonance and the amplitude of the resonant near field to the power n ($n = 3$ in the case of THG) as it can be observed by rewriting Eq. (4.36) for third-harmonic generation. Additionally, the scattered near field in Eq. (4.37) is proportional

to the amplitude of the pump wave-vector, which provides better efficiency for higher energies. Thus, our current goal is to excite a structure with the pump at the frequency of a resonant mode exhibiting a large near field enhancement. In addition, this theoretical assumption is correlated with experimental studies, which proved that the near field enhancement and the quality factor of resonant modes at the pump frequency play indeed a critical role in the frequency conversion efficiency [101]. In this section, we will study specifically the interaction of a dipolar resonant mode with a quadrupolar mode that is of particular interest in plasmonics.

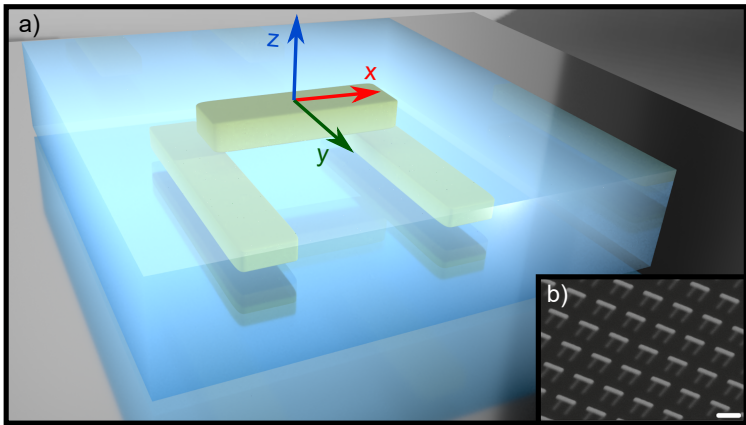


Figure 5.7: (a) Example of a dolmen structure built out of three gold nano-rods, two rods in the lower layers parallel to each other and one rod on top of the latter oriented in a perpendicular direction. The three nano-rods are embedded inside a dielectric material. The gold nano-rod on top of the structure owns a fundamental resonance with a strong dipole moment whose near field induces the excitation of the two gold nano-rods located below that exhibit a quadrupolar mode. (Reprinted with permission from [7]. Copyright (2019) American Chemical Society. Only the panel (b) comes from the original print.)

So called plasmonic *dark modes* might exhibit the near field enhancement and the large quality factor required to provide a high conversion efficiency to the third harmonic. However, dark modes cannot be excited from- and radiate to the far field because their overall dipolar moment is nil. In other words they cannot exchange energy with the far field at all. One alternative is to introduce an additional element to the system that can sustain energy exchange with the far field and couple with the dark mode. Hence, the dark mode could receive and radiate energy through this element. In a plasmonic structure for instance, the idea would be to

induce a near field mediated hybridization of a dark mode with a dipolar plasmonic resonance that can be excited from the far field.

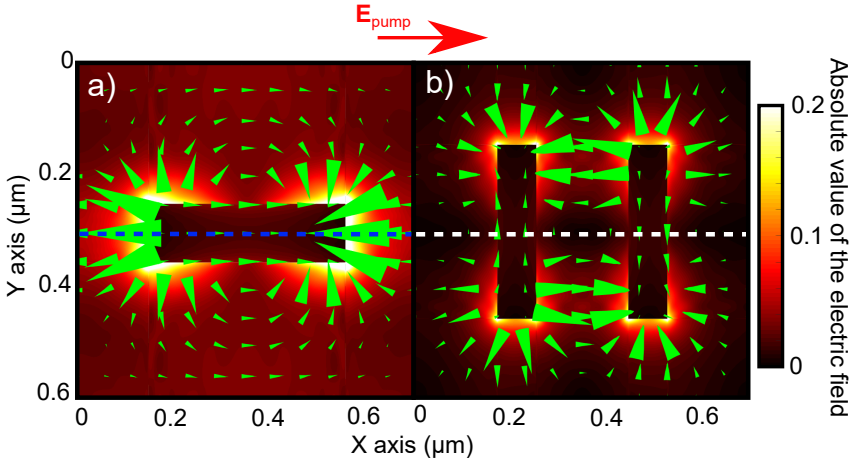


Figure 5.8: In this figure are displayed as an example the top view of a plan $(0,x,y)$ of the near fields of a dipolar and a quadrupolar resonance in panels (a) and (b), respectively, without external excitation [67]. The dipolar resonance in panel (a) is excited on a gold nano-rod 450 nm long, 120 nm large and 60 nm thick. The blue dashed line denotes a symmetry plane of the field. In (b) the quadrupolar mode is excited on a pair of nano-rods 400 nm by 80 nm by 40 nm separated from each other by 120 nm center-to-center. The white dashed line denotes a plane of anti-symmetry of the field at the quadrupolar resonance. The red arrow denotes the orientation of an incoming x -polarized electric field.

Let us first study individually a quadrupolar and a dipolar plasmonic resonant mode. Fig. 5.8 (a) displays the top view of the electric field belonging to a plasmonic dipolar resonance on a single gold nano-rod. Panel (b) contains the field of a quadrupolar resonant mode on a pair of nano-rods. The green arrows denote the in-plane components of the electric fields. These fields are calculated using the approach described in section 2.7 that does not account for an external excitation. In addition, we do not consider any coupling between the quadrupolar and the dipolar modes. The dimensions of the gold nano-rods are given in the caption below the figure but since they are not yet relevant in these explanations, let us focus on the symmetries of the fields.

We consider the situation of an incoming plane wave with normal incidence and polarized along the x axis marked by a red arrow at the top of the Fig 5.8. Consequently, an associated background field can be

considered, by definition we assume that the background field propagates through the structure as if it was a homogeneous material with the same permittivity as the superstrate. The capability of the incoming field to excite each mode is quantified by the overlap integral of the background field with the resonant near field (see Eq. (2.64)). We observe that the field of the dipolar mode possesses one plane of symmetry, marked with a blue dashed line in Fig. 5.8 (a). The overlap integral of the background electric field with the field of the dipolar mode, on each side of the symmetry plane, will provide the same results that we will add to each other to calculate the total overlap. In the case of the quadrupolar mode, the same plane marked with a white dashed line is a plane of anti-symmetry. Thus in Fig. 5.8 (b), the overlap integral of the background field with the field distribution of the quadrupolar mode on each side of the white dashed line will provide opposite values that will exactly cancel each other. Thus, the overall overlap integral is equal to zero. Using the approach depicted in the pole expansion Eqs. (2.64) and (2.65), we can deduce that the dipole mode can be excited from the far field but the quadrupolar mode cannot be excited this way and thus the quadrupolar plasmonic mode depicted in Fig. 5.8 (b) is a dark mode.

According to the idea previously mentioned, we now assume the situation where the single nano-rod is located near to the pair of nano-rods so that they can couple by the mediation of their near-fields. Additionally, we consider that the frequencies of the dipolar and the quadrupolar modes of the single and the pair of nano-rods are close enough to hybridize. We can study the capability of the quadrupolar plasmonic mode to radiate to the far field through the dipolar resonance using the approach based on the pole expansion detailed in the previous chapters. While deriving Eq. (2.64), we found that the overlap integral of a resonant near field with a plane wave coming from the far field results in the coupling coefficient of this resonance with the far field. In the same fashion, we can assume that the coupling between the dipolar mode and the quadrupolar mode can be evaluated by the overlap of their respective near fields. In the situation where the single nano-rod has a centered position relatively to the pair of nano-rods, we can anticipate from Fig. 5.8 that the overlap integral between a symmetric and an anti-symmetric field distribution is going to be nil. Due to symmetry, the dipole has to be moved aside, more specifically in the direction \mathbf{y} .

We finally reach the design of an experimental plasmonic system, the dolmen structure [7, 37, 111] depicted in Fig. 5.7. The structure is made out of three layers, a first layer contains two gold nano-rods parallel to each other and close enough to couple and exhibit a quadrupolar resonant mode.

On top of the first layer is printed in a perpendicular direction a single nano-rod exhibiting a resonant mode with a strong dipolar moment. These two layers are separated by a spacer that will induce a phase retardation in the coupling between the quadrupolar mode and the dipolar mode. The retardation effect gives rise to a peculiar behavior known as the so called *electromagnetically induced transparency* (EIT), which is originally a quantum phenomenon observed in atomic physics.

This phenomenon is best described using an energy level diagram that provides an analogy with atomic physics. Let us consider a system with three energy levels as depicted in Fig. 5.9. The energy level $|0\rangle$ represents the ground state. $|1\rangle$ represents the energy level of a dipolar mode that can be excited from the ground state. $|2\rangle$ denotes the energy level of the quadrupolar mode that cannot be excited from the ground state. γ_1 and γ_2 are the decay rates of $|1\rangle$ and $|2\rangle$. The energy level of the quadrupolar mode cannot exchange energy with the ground state and thus its decay rate γ_2 is non-radiative. As a consequence, γ_2 is much smaller than the decay rate of the dipolar mode γ_1 that can radiate. On the other hand a possible coupling between the two excited energy states can occur and is expressed by the factor $\kappa e^{i\phi}$ that describes the intensity of the coupling and the phase retardation induced by the energy exchange between the two resonant modes. Thus, the energy state $|2\rangle$ can be excited and radiate by the mediation of $|1\rangle$. The three level system owns two excitation-to-radiation paths: $|0\rangle \rightarrow |1\rangle$ and $|0\rangle \rightarrow |1\rangle \rightarrow |2\rangle \rightarrow |1\rangle$, where the energy is radiated from the dipolar mode. These two patterns allow the two excited states to radiate coherently and thus interfere with each other, accounting for the phase retardation ϕ due to the complex coupling factor.

In the plasmonic analog the coupling strength κ between the dark mode and the bright dipolar mode is proportional to the displacement of the single nano-rod out of the centered position on top of the quadrupolar mode. The phase ϕ induced during the coherent emission of the two modes is proportional to the thickness of the spacer between the single nanorod and the pair of nanorods. The value of the phase retardation will define the kind of interference that will occur between the two modes. In the case $\phi = 0$, a destructive interference occurs and a transmission window opens in between the two resonances with a minimum of absorption. In the case $\phi = \pi/2$ a constructive interference occurs and we observe a strong peak of absorption in between the two resonances that is characteristic from the so called *electromagnetically induced absorption* (EIA) [112].

In the case of EIA, the peak of absorption is the sign of a strong enhancement of the near field. The latter effect is of interest in our journey to design a structure with a high conversion efficiency from the pump fre-

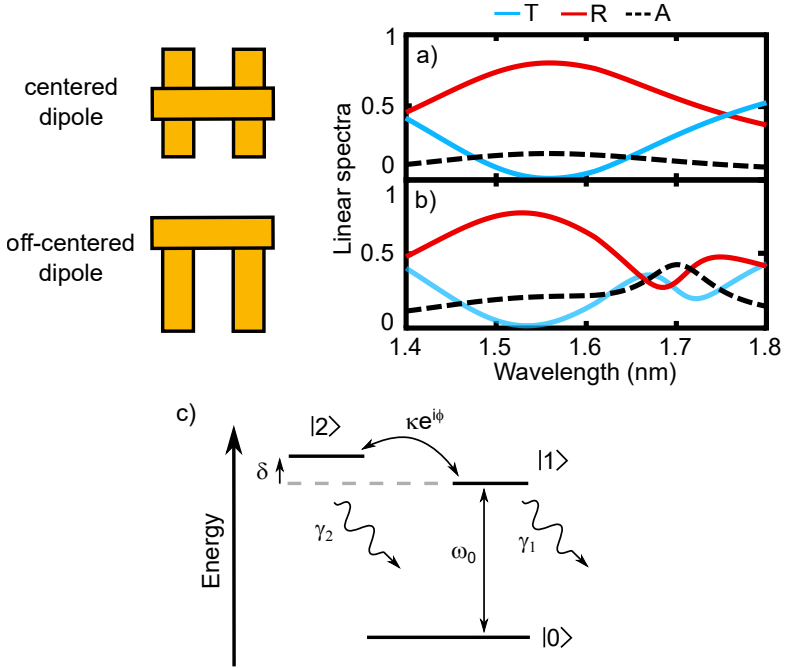


Figure 5.9: (a) Scheme and linear spectra of a EIA structure with a centered dipole. The dipole cannot excite the quadrupolar mode of the pair of gold nano-rod. Thus, the quadrupolar mode cannot be excited and only the dipolar resonance appears in the linear spectra. In panel (b) is displayed the scheme and linear spectra of the structure with a shifted dipole. We observe a second resonance occurring at $1.72 \mu\text{m}$ and a local peak of absorption. These are the signs that the dipolar resonance hybridize with the dark mode, which can then radiate to the far field. Panel (c) is displayed the energy level diagram illustrating the electromagnetically induced transparency or absorption. The ground state is the energy level $|0\rangle$. Thus, $|1\rangle$ and $|2\rangle$ are the quadrupolar and dipolar resonances. The coupling between the two resonant modes is modeled by $\kappa e^{i\phi}$. Depending if ϕ is equal to 0 or $\pi/2$ we obtain an electromagnetically induced transparency or absorption [112].

quency to the third harmonic. Additionally, from the classical point of view we consider that the two modes hybridize and the overall structure will then exhibit two resonances with interesting properties. Both hybridized resonant modes have a higher quality factor than dipolar resonances, a characteristic they inherit from the dark mode. However, they can both be excited from the far field. Considering the enhanced absorption and the very high quality factors owned by the dolmen structure resonances, the latter seems a very good choice of structure for frequency conversion to the third harmonic.

5.2.2 Enhanced third-harmonic generation in dolmen structures

Let us consider the experimental structure depicted Fig. 5.7 (b). The top single nano-rod is 450 nm long, 120 nm wide and 60 nm thick. Both rods of the lower pair are 400 nm by 80 nm by 40 nm and they are separated from each other by a center-to-center distance of 270 nm. The single nano-rod is separated from the pair of nano-rods by a spacer 120 nm thick and the nano-rods are made of gold while the surrounding dielectric is as in the previous example IC1-200. The refractive index of both materials is numerically modeled using the same models as in the previous section, the gold dielectric permittivity is calculated using the critical point model, and the refractive index of IC1-200 is assumed to be 1.3.

The experimental measurement is performed on an array of $100 \times 100 \mu\text{m}^2$ containing many structures. The array is excited with an incoming pump field polarized along the \mathbf{x} axis, with a wavelength between 1.2 μm and 1.9 μm . The resulting signals are displayed Fig. 5.10 panels (a) and (b). The red solid line denotes the absorption of the structure. The black dots connected with a black solid line mark the third harmonic generation measured by transmittance and polarized along \mathbf{x} and \mathbf{y} in (a) and (b), respectively. Below, in the panels (c) and (d) are displayed the numerical results calculated using the nonlinear Fourier modal method and a model based on the finite elements method.

In Fig. 5.10 panel (c), the red solid line denotes the linear absorption numerically calculated within the Fourier modal method. The black solid line represents the intensity generated at the third harmonic. The response at the third harmonic is calculated in two steps as in the previous example. In a first step we use the linear Fourier modal method to compute the near field created by pump. Thus, we use the extended anharmonic oscillator model to calculate the $\chi^{(3)}$ that we multiply to the pump near field to obtain the nonlinear polarization field inside the structure. Finally, we

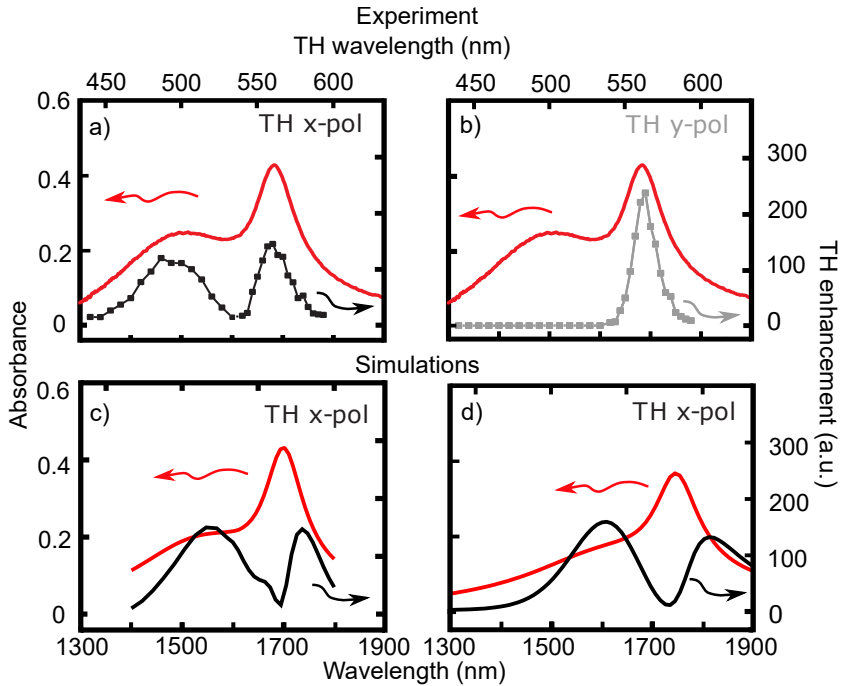


Figure 5.10: (a) The red solid line displays the linear spectra of absorption of the structure excited by a x-polarized plane wave with normal incidence, the black dots linked by a solid black line represent the measured third harmonic generation emitted with x-polarization. In (b) is displayed the y-polarized third harmonic generation that is triggered by a symmetry breaking. Panel (c) displays the x-polarized third harmonic generation theoretically predicted using the Fourier modal method and the reciprocity principle applied for a perfectly symmetric structure. In (c) is plotted the third harmonic enhancement predicted by integrating the pump field inside the gold nano-rods using a finite element method. (Reprinted with permission from [7]. Copyright (2020) American Chemical Society. The panel (c) is not part of the original print and has been added by the author of this thesis.)

calculate the propagation of plane waves incoming from the top and bottom half spaces at the third harmonic frequency with normal incidence and with a s- and p-polarizations. Owing to the reciprocity principle, the overlap integral between the near field induced by the incoming plane waves at the third harmonic and the nonlinear polarization field provide the field radiated to the far field at the third harmonic as explained in section 4.3.2.

In panel (d) the near field induced at the pump frequency is calculated using the finite element method. Then the generated third harmonic is calculated by integrating the nonlinear polarization induced inside the gold nano-rods as described section 4.3.1.

We observe that the linear response calculated with the Fourier modal method is fairly similar to the measured absorption, however in the result computed using the FEM, the plateau at 1550 nm is not as pronounced as in the experiment. At the third harmonic the Fourier modal reproduce well the two peak of emission of same amplitude and similar linewidth observed in the experiment. However, in the third harmonic signal calculated with the nonlinear Fourier modal method, the peak of smaller wavelength exhibits a slight slope-breaking on its side at 1680 nm that is a numerical artifact whose amplitude decreased while we increased the accuracy of the calculation. The third harmonic generation calculated with the finite element method do not exhibit similar artifact, however the second peak of emission calculated at 1800 nm is smaller and with a larger linewidth than in the experiment. Finally, the peak of emission radiated at the third harmonic are red shifted in the simulations compared to the experiment. This phenomenon has been explained in the previous section. Additionally, in the current experiment, the sample was not excited with a perfectly normal incidence, which could have slightly shifted the third harmonic response to shorter wavelength compared to the numerical calculation modeling a perfectly normal incidence.

Finally, a very interesting effect has been observed. Indeed in the case of a perfect structure with $(O, \mathbf{y}, \mathbf{z})$ as symmetry plan, there is no third-harmonic generated with a polarization along the direction \mathbf{y} . This characteristic is predicted in both simulations. Indeed, in perfectly symmetric dolmen structures, the third harmonic is radiated through the dipole that radiate with a polarization aligned with its moment. Though in our case the dipolar mode has a x -oriented moment, in the experiment a very strong peak of emission polarized along the y axis has been measured at 1700 nm. In the end, it has been demonstrated that the unexpected peak of emission was due to a structural symmetry breaking of the nano-rod pair [7]. In the situation where the two nano-rods do not own the same length, the symmetry breaking induces a very strong third-harmonic generated directly by

5.2 Influence of symmetry breaking on the third-harmonic generation

the quadrupole and leading to the apparition of the peak in Fig.5.10 (b). The importance of structural symmetries and anti-symmetries in nonlinear optical phenomena is known. However, in this example we observe that the enhancement induced by a symmetry breaking can be stronger than the complicated process we enabled using an EIA structure.

6 Conclusion and outlook

One of the weaknesses of our age is our apparent inability to distinguish our need from our greed.

James Clerk Maxwell (1831-1879)

In this thesis, we explored different approaches based on the Mittag-Leffler expansion. We showed that not only the scattered field but also the total field inside a nano-structure can be derived using the pole expansion. This additional insight on the Mittag-Leffler expansion shows that this series expansion can be used in a more general and systematic manner for the calculation of different physical quantities. This method describes the behavior of a structure over a full spectral range by the only mean of few full-wave solutions of Maxwell's equations that is of high interest for time consuming calculations such as the modeling of complex nanostructures or nonlinear phenomena, as it is demonstrated in chapter 4. While the approach is already fast, it could be improved by the development of methods able to retrieve different types of modes like static modes [113]. In addition, the derivation of resonant modes could account for the hydrodynamic model to consider different types of phenomena like nonlocality or inter-band transitions inside metals [58]. In addition, a model with such properties could then calculate hydrodynamic resonances.

The description of nonlinear optical phenomena in systems made of stacked periodic layers is expressed by extending the original scheme of the Fourier modal method. This approach uses the undepleted pump approximation. Additionally, we formulate new factorization rules necessary for the Fourier transformation of higher order tensors as the nonlinear susceptibility. Combined with adaptive spatial resolution, these new features ensure the fastest convergence achieved so far to solve nonlinear Maxwell's equations within the Fourier modal method. This method is unfortunately limited by the new factorization rule that becomes memory and power consuming for tensors of order higher than two. However, it is demonstrated later that other alternatives are possible using the reciprocity principle.

We observe that even the calculation of the second-harmonic generation within the Fourier modal method can become rather time consuming for complex structures. Thus, we show that it is possible to improve upon the previous work, using the pole expansion in the derivation of the harmonic generation within periodic structures made of materials with nonlinear properties. The pole expansion comes as a semi analytic model that is by definition faster than fully numerical schemes. Additionally, the semi-analytic formulation expressed in Eq. (4.37) gives a deep insight in the physics ruling nonlinear phenomena inside nanostructures. Indeed, in this formula the different competing effects enhancing or hampering the nonlinear conversion are expressed separately. On one hand the superior enhancement provided by resonances at pump frequencies is analytically expressed and quantified. On the other hand, the influence of the quality factor of each resonance occurs explicitly in the denominator of the pole

expansion as a non-vanishing imaginary part in the limit of frequencies close to the resonant poles. Finally the importance of the symmetries and anti-symmetries and the impact of the near field enhancement of each resonance is accurately quantified by the mean of overlap integrals. This last step might be calculated numerically in nontrivial cases. However, visualizing the symmetries of the resonant poles at the pump and at the harmonic frequencies using field plots already provides a good indication concerning the possible enhancement of harmonic generation within a nanostructure. In addition, the speed and the memory consumption of the method can be further improved using an approach based on the group theory as L. Li did for the linear Fourier modal method [114–116].

While we tackle the contribution of symmetries and anti-symmetries in the volumetric emission of pump harmonics, we might remember that the crystalline symmetries of a dielectric material are described by the symmetry of its nonlinear susceptibility tensor. We are thus able to draw a crystalline to structural symmetry analysis within the same picture that could be relevant in the optimization of the frequency conversion within nanostructured media.

We showed that Kerr optical phenomenon can be modeled using a recursive method, which calculates a field emitted at the pump frequency. However, instead of modeling the emission of light at the pump frequency, we can modify this approach considering a change of refractive index proportional to the square of the electric field that will ensure the conservation of energy. In theory, this other approach requires that we account for structural changes at each recursive step, thus we would have to calculate the new position and field distribution of resonant modes at every iteration. Nonetheless, one can use approaches based on the resonant state expansion that can account for structural changes without requiring new solutions of Maxwell's equations [44, 71, 94]. Thus, we could account for the Kerr optical effect accurately for a low numerical cost combining the pole expansion approach and the resonant state expansion. Similarly, a perturbative approach implemented upon the pole expansion could take into account energy depletion in the pump field and thus get rid of the undepleted pump approximation we used so far.

In the last part of the 4th-chapter we demonstrated how the reciprocity principle can be used in real space to calculate third-harmonic generation, avoiding at the same time the issue related to the implementation of heavy factorization rules. This method proved to be efficient in the resolution of nonlinear Maxwell's equations, in complex plasmonic structures exhibiting dark resonant modes or chiroptical effects. Applying the reciprocity principle in real space is nonetheless time consuming due to the many Fourier

transformations required at each spectral point. An improvement of this approach would remain in the implementation of the pole expansion for the calculation of the pump field but also the calculation of the probe field at the generated harmonic.

The pole expansion provided a powerful tool capable of drastically improving the current numerical methods. Thus the construction of optimization algorithms solving nonlinear Maxwell's equations within the Fourier modal method becomes possible. Such algorithm could in principle further optimize known structures to achieve even higher conversion efficiency and eventually discover new designs exhibiting strong nonlinear effects.

Bibliography

- [1] M. Castro-Lopez, D. Brinks, R. Sapienza, and N. F. van Hulst, “Aluminum for Nonlinear Plasmonics: Resonance-Driven Polarized Luminescence of Al, Ag, and Au Nanoantennas,” *Nano Letters* **11**(11), 4674–4678 (2011).
- [2] R. Yu, J. D. Cox, and F. J. G. de Abajo, “Nonlinear Plasmonic Sensing with Nanographene,” *Phys. Rev. Lett.* **117**, 123,904 (2016).
- [3] S. G. Tikhodeev, A. L. Yablonskii, E. A. Muljarov, N. A. Gippius, and T. Ishihara, “Quasiguidded modes and optical properties of photonic crystal slabs,” *Physical Review B* **66**, 045,102 (2002).
- [4] L. Li, “Fourier modal method for crossed anisotropic gratings with arbitrary permittivity and permeability tensors,” *Journal of Optics A: Pure and Applied Optics* **5**(4), 345 (2003).
- [5] T. Paul, C. Rockstuhl, and F. Lederer, “A numerical approach for analyzing higher harmonic generation in multilayer nanostructures,” *J. Opt. Soc. Am. B* **27**, 1118–1130 (2010).
- [6] L. Gui, M. Hentschel, J. Defrance, J. Krauth, T. Weiss, and H. Giessen, “Nonlinear Born-Kuhn Analog for Chiral Plasmonics,” *ACS Photonics* **6**(12), 3306–3314 (2019).
- [7] J. Krauth, T. Schumacher, J. Defrance, B. Metzger, M. Lippitz, T. Weiss, H. Giessen, and M. Hentschel, “Nonlinear Spectroscopy on the Plasmonic Analog of Electromagnetically Induced Absorption: Revealing Minute Structural Asymmetries,” *ACS Photonics* **6**(11), 2850–2859 (2019).
- [8] J. C. Maxwell, “A dynamical theory of the electromagnetic field,” *Philosophical Transactions of the Royal Society of London* **455**, 459–512 (1865).
- [9] J. B. Pendry, D. Schurig, and D. R. Smith, “Controlling Electromagnetic Fields,” *Science* **312**(5781), 1780–1782 (2006).
- [10] E. Yablonovitch, T. J. Gmitter, and K. Leung, “Photonic band structure: The face-centered-cubic case employing nonspherical atoms,” *Phys. Rev. Lett.* **67**, 2295–2298 (1991).

- [11] D. R. Smith, W. J. Padilla, D. C. Vier, S. C. Nemat-Nasser, and S. Schultz, “Composite Medium with Simultaneously Negative Permeability and Permittivity,” *Phys. Rev. Lett.* **84**, 4184–4187 (2000).
- [12] F. Cheng, J. Gao, T. S. Luk, and X. Yang, “Structural color printing based on plasmonic metasurfaces of perfect light absorption,” *Scientific Reports* **5**, 11,045 (2015).
- [13] M. Esposito, F. Todisco, S. Bakhti, A. Passaseo, I. Tarantini, M. Cuscunà, N. Destouches, and V. Tasco, “Symmetry Breaking in Oligomer Surface Plasmon Lattice Resonances,” *Nano Letters* **19**(3), 1922–1930 (2019).
- [14] M. A. Barry, V. Berthier, B. D. Wilts, M.-C. Cambourieux, R. Pollès, O. Teytaud, E. Centeno, N. Biais, and A. Moreau, “Evolutionary algorithms converge towards evolved biological photonic structures,” *Sci. Rep.* **10**, 12,024 (2020).
- [15] N. Liu, M. Mesch, T. Weiss, M. Hentschel, and H. Giessen, “Infrared Perfect Absorber and Its Application As Plasmonic Sensor,” *Nano Letters* **10**(7), 2342–2348 (2010).
- [16] F. Kiani, F. Sterl, T. V. Tsoulos, K. Weber, H. Giessen, and G. Tagliabue, “Ultra-Broadband and Omnidirectional Perfect Absorber Based on Copper Nanowire/Carbon Nanotube Hierarchical Structure,” *ACS Photonics* **7**(2), 366–374 (2020).
- [17] P. Russell, “Photonic Crystal Fibers,” *Science* **299**(5605), 358–362 (2003).
- [18] P. S. Russell, “Photonic-Crystal Fibers,” *J. Lightwave Technol.* **24**(12), 4729–4749 (2006).
- [19] J. Karst, N. H. Cho, H. Kim, H.-E. Lee, K. T. Nam, H. Giessen, and M. Hentschel, “Chiral Scatterometry on Chemically Synthesized Single Plasmonic Nanoparticles,” *ACS Nano* **13**(8), 8659–8668 (2019).
- [20] J. Karst, N. Strohfeldt, M. Schäferling, H. Giessen, and M. Hentschel, “Single Plasmonic Oligomer Chiral Spectroscopy,” *Advanced Optical Materials* **6**(14), 1800,087 (2018).
- [21] A. Moreau, C. Ciraci, and D. R. Smith, “The impact of nonlocal response on metallo-dielectric multilayers and optical patch antennas,” *Phys. Rev. B* **87**(4), 045,401 (2013).

- [22] J. A. H. van Nieuwstadt, M. Sandtke, R. H. Harmsen, F. B. Segerink, J. C. Prangma, S. Enoch, and L. Kuipers, “Strong modification of the nonlinear optical response of metallic subwavelength hole arrays,” *Phys. Rev. Lett.* **97**, 146,102 (2006).
- [23] K. Martti and V. Z. Anatoly, “Nonlinear plasmonics,” *Nature Photonics* **6**(11), 737–748 (2012).
- [24] S. Palomba, M. Danckwerts, and L. Novotny, “Nonlinear plasmonics with gold nanoparticle antennas,” *Journal of Optics A: Pure and Applied Optics* **11**(11), 114,030 (2009).
- [25] T. Steinle, M. Floess, A. Steinmann, V. Kumar, G. Cerullo, and H. Giessen, “Stimulated Raman Scattering Microscopy with an All-Optical Modulator,” *Phys. Rev. Applied* **11**, 044,081 (2019).
- [26] M. Mesch, B. Metzger, M. Hentschel, and H. Giessen, “Nonlinear plasmonic sensing,” *Nano Letters* **16**, 3155–3159 (2016).
- [27] J.-J. Li and K.-D. Zhu, “Nonlinear optical mass sensor with an optomechanical microresonator,” *Applied Physics Letters* **101**(14), 141,905 (2012).
- [28] D. M. Sullivan, “Nonlinear FDTD formulations using Z transforms,” *IEEE Transactions on Microwave Theory and Techniques* **43**, 676–682 (1995).
- [29] K. Hayata, M. Nagai, and M. Koshiba, “Finite-element formalism for nonlinear slab-guided waves,” *IEEE Transactions on Microwave Theory and Techniques* **36**, 1207–1215 (1988).
- [30] L. Li, “Use of Fourier series in the analysis of discontinuous periodic structures,” *J. Opt. Soc. Am. A* **13**, 1870–1876 (1996).
- [31] G. Granet, “Reformulation of the lamellar grating problem through the concept of adaptive spatial resolution,” *J. Opt. Soc. Am. A* **16**, 2510–2516 (1999).
- [32] T. Weiss, G. Granet, N. A. Gippius, S. G. Tikhodeev, and H. Giessen, “Matched coordinates and adaptive spatial resolution in the Fourier modal method,” *Optics express* **17**, 8051–8061 (2009).
- [33] R.-C. Ge, P. T. Kristensen, J. F. Young, and S. Hughes, “Quasinormal mode approach to modelling light-emission and propagation in nanoplasmonics,” *New J. Phys.* **16**(11), 113,048 (2014).

- [34] X. Yin, M. Schäferling, B. Metzger, and H. Giessen, “Interpreting Chiral Nanophotonic Spectra: The Plasmonic Born-Kuhn Model,” *Nano Letters* **13**(12), 6238–6243 (2013).
- [35] M. Schäferling, D. Dregely, M. Hentschel, and H. Giessen, “Tailoring enhanced optical chirality: design principles for chiral plasmonic nanostructures,” *Physical Review X* **2**, 031,010 (2012).
- [36] Y. Tang and A. E. Cohen, “Optical Chirality and Its Interaction with Matter,” *Phys. Rev. Lett.* **104**, 163,901 (2010).
- [37] N. Liu, L. Langguth, T. Weiss, Ka, M. Fleischhauer, T. Pfau, and H. Giessen, “Plasmonic Analogue of Electromagnetically Induced Transparency at the Drude Damping Limit,” *Nat. Mater.* **8**, 758 (2009).
- [38] L. Li, “Use of Fourier series in the analysis of discontinuous periodic structures,” *J. Opt. Soc. Am. A* **13**, 1870–1876 (1996).
- [39] E. J. Post, *Formal structure of electromagnetism* (North Holland, Amsterdam, 1962).
- [40] H. Chen, C. T. Chan, and P. Sheng, “Transformation optics and metamaterials,” *Nature Materials* **9**(5), 387–396 (2010).
- [41] A. Vakil and N. Engheta, “Transformation Optics Using Graphene,” *Science* **332**(6035), 1291–1294 (2011).
- [42] A. V. Kildishev and V. M. Shalaev, “Engineering space for light via transformation optics,” *Opt. Lett.* **33**(1), 43–45 (2008).
- [43] A. Zee, *Group Theory in a Nutshell for Physicists* (Princeton, New Jersey, 2016).
- [44] E. A. Muljarov and T. Weiss, “Resonant-state expansion for open optical systems: generalization to magnetic, chiral, and bi-anisotropic materials,” *Opt. Lett.* **43**(9), 1978–1981 (2018).
- [45] T. Weiss and E. A. Muljarov, “How to calculate the pole expansion of the optical scattering matrix from resonant states,” *Phys. Rev. B* **98**, 085,433 (2018).
- [46] P. T. Leung, S. Y. Liu, and K. Young, “Completeness and orthogonality of quasinormal modes in leaky optical cavities,” *Phys. Rev. A* **49**, 3057–3067 (1994).

- [47] K. M. Lee, P. T. Leung, and K. M. Pang, “Dyadic formulation of morphology-dependent resonances. I. Completeness relation,” *J. Opt. Soc. Am. B* **16**(9), 1409–1417 (1999).
- [48] M. D. Doost, W. Langbein, and E. A. Muljarov, “Resonant-state expansion applied to planar open optical system,” *Phys. Rev. A* **85**, 023,835 (2012).
- [49] R.-C. Ge and S. Hughes, “Design of an efficient single photon source from a metallic nanorod dimer: a quasi-normal mode finite-difference time-domain approach,” *Opt. Lett.* **39**(14), 4235–4238 (2014).
- [50] R.-C. Ge, P. T. Kristensen, J. F. Young, and S. Hughes, “Quasi-normal mode approach to modelling light-emission and propagation in nanoplasmonics,” *New Journal of Physics* **16**(11), 113,048 (2014).
- [51] B. Gralak and M. Abdelrahman, “Completeness and divergence-free behavior of the quasi-normal modes using causality principle,” in *The International Photonics and Optoelectronics Meeting (POEM)*, p. 36 (Optical Society of America, 2018).
- [52] P. T. Kristensen, C. V. Vlack, and S. Hughes, “Generalized effective mode volume for leaky optical cavities,” *Opt. Lett.* **37**(10), 1649–1651 (2012).
- [53] M. Perrin, “Eigen-energy effects and non-orthogonality in the quasi-normal mode expansion of Maxwell equations,” *Opt. Express* **24**(24), 27,137–27,151 (2016).
- [54] Q. Bai, M. Perrin, C. Sauvan, J.-P. Hugonin, and P. Lalanne, “Efficient and intuitive method for the analysis of light scattering by a resonant nanostructure,” *Opt. Express* **21**(22), 27,371–27,382 (2013).
- [55] P. Lalanne, W. Yan, K. Vynck, C. Sauvan, and J. Hugonin, “Light Interaction with Photonic and Plasmonic Resonances,” *Laser Photonics Rev.* **12**(5), 1700,113 (2018).
- [56] L. Armitage, M. D. Doost, W. Langbein, and E. A. Muljarov, “Resonant-state expansion applied to planar waveguides,” *Phys. Rev. A* **89**, 053,832 (2014).

- [57] A. J. Bennett, “Influence of the electron charge distribution on surface-plasmon dispersion,” *Phys. Rev. B* **1**(1), 203–207 (1970).
- [58] G. Toscano, J. Straubel, A. Kwiatkowski, C. Rockstuhl, F. Evers, H. Xu, N. Asger Mortensen, and M. Wubs, “Resonance shifts and spill-out effects in self-consistent hydrodynamic nanoplasmonics,” *Nat. Commun* **6**(1), 7132 (2015).
- [59] H. S. Sehmi, W. Langbein, and E. A. Muljarov, “Applying the resonant-state expansion to realistic materials with frequency dispersion,” *Phys. Rev. B* **101**, 045,304 (2020).
- [60] C. Sauvan, P. Lalanne, and J. Hugonin, “Truncation rules for modelling discontinuities with Galerkin method in electromagnetic theory,” *Optical and Quantum Electronics* **36**(1-3), 271–284 (2004).
- [61] G. Granet and J. P. Plumey, “Parametric formulation of the Fourier modal method for crossed surface-relief gratings,” *J. Opt. A: Pure Appl. Opt.* **4**, S145–S149 (2002).
- [62] T. Weiss, N. A. Gippius, S. G. Tikhodeev, G. Granet, and H. Giessen, “Efficient calculation of the optical properties of stacked metamaterials with a Fourier modal method,” *J. Opt. A: Pure Appl. Opt.* **11**, 114,019–1–5 (2009).
- [63] T. Schuster, J. Ruoff, N. Kerwien, S. Rafler, and W. Osten, “Normal vector method for convergence improvement using the RCWA for crossed gratings,” *J. Opt. Soc. Am. A* **24**, 2880–2890 (2007).
- [64] R. Antos, “Fourier factorization with complex polarization bases in modeling optics of discontinuous bi-periodic structures,” *Opt. Express* **17**, 7269–7274 (2009).
- [65] S. Essig and K. Busch, “Generation of adaptive coordinates and their use in the Fourier modal method,” *Opt. Express* **18**, 23,258–23,274 (2010).
- [66] J. Küchenmeister, T. Zebrowski, and K. Busch, “A construction guide to analytically generated meshes for the Fourier modal method,” *Opt. Express* **20**, 17,319–17,347 (2012).
- [67] T. Weiss, N. A. Gippius, S. G. Tikhodeev, G. Granet, and H. Giessen, “Derivation of plasmonic resonances in the Fourier modal method with adaptive spatial resolution and matched coordinates,” *J. Opt. Soc. Am. A* **28**, 238–244 (2011).

- [68] D. A. Bykov and L. L. Doskolovich, “Numerical Methods for Calculating Poles of the Scattering Matrix With Applications in Grating Theory,” *Journal of Lightwave Technology* **31**(5), 793–801 (2013).
- [69] T. Weiss, M. Mesch, M. Schäferling, H. Giessen, W. Langbein, and E. A. Muljarov, “From dark to bright: First-order perturbation theory with analytical mode normalization for plasmonic nanoantenna arrays applied to refractive index sensing,” *Phys. Rev. Lett.* **116**, 237,401 (2016).
- [70] G. B. Arfken and H. J. Weber, *Mathematical Methods for Physicists*, 6th ed. (2011).
- [71] S. V. Lobanov, W. Langbein, and E. A. Muljarov, “Resonant-state expansion of three-dimensional open optical systems: Light scattering,” *Phys. Rev. A* **98**, 033,820 (2018).
- [72] M. Kamandar Dezfouli and S. Hughes, “Regularized quasinormal modes for plasmonic resonators and open cavities,” *Phys. Rev. B* **97**, 115,302 (2018).
- [73] P. G. Etchegoin, E. Le Ru, and M. Meyer, “An analytic model for the optical properties of gold,” *J. Chem. Phys.* **125**, 164,705 (2006).
- [74] J. R. de Lasson, P. T. Kristensen, J. Mørk, and N. Gregersen, “Roundtrip matrix method for calculating the leaky resonant modes of open nanophotonic structures,” *J. Opt. Soc. Am. A* **31**(10), 2142–2151 (2014).
- [75] P. Lalanne, W. Yan, A. Gras, C. Sauvan, J.-P. Hugonin, M. Besbes, G. Demésy, M. D. Truong, B. Gralak, F. Zolla, A. Nicolet, F. Binkowski, L. Zschiedrich, S. Burger, J. Zimmerling, R. Remis, P. Urbach, H. T. Liu, and T. Weiss, “Quasinormal mode solvers for resonators with dispersive materials,” *J. Opt. Soc. Am. A* **36**(4), 686–704 (2019).
- [76] S. Raza, G. Toscano, A.-P. Jauho, M. Wubs, and N. A. Mortensen, “Unusual resonances in nanoplasmonic structures due to nonlocal response,” *Phys. Rev. B* **84**(12), 121,412 (2011).
- [77] N. Crouseilles, P.-A. Hervieux, and G. Manfredi, “Quantum hydrodynamic model for the nonlinear electron dynamics in thin metal films,” *Phys. Rev. B* **78**(15), 155,412 (2008).

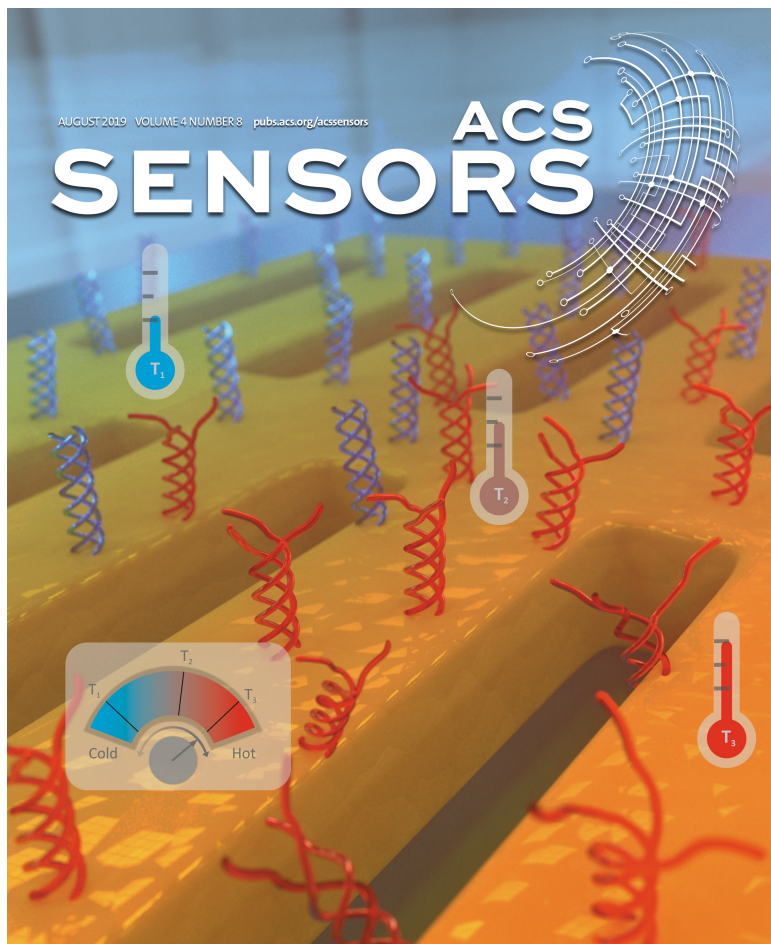
- [78] B. Metzger, T. Schumacher, M. Hentschel, M. Lippitz, and H. Giessen, “Third Harmonic Mechanism in Complex Plasmonic Fano Structures,” *ACS Photonics* **1**(6), 471–476 (2014).
- [79] R. P. Feynman, *Volume 1: mainly mechanics, radiation, and heat* (Basic Books, New York, 1963).
- [80] E. Rosencher and B. Vinter, *Optoélectronique*, 2nd ed. (Dunod, Paris, 2002).
- [81] R. W. Boyd, *Nonlinear optics*, 3rd ed. (Academic Press, 2008).
- [82] C. Ciraci, J. B. Pendry, and D. R. Smith, “Hydrodynamic Model for Plasmonics: A Macroscopic Approach to a Microscopic Problem,” *ChemPhysChem* **14**, 1109–1116 (2013).
- [83] K. Baumgärtel and K. Sauer, *Topics on Nonlinear Wave-Plasma Interaction* (Birkhäuser Basel, Basel, 1987).
- [84] P. Ginzburg, A. V. Krasavin, G. A. Wurtz, and A. V. Zayats, “Non-perturbative Hydrodynamic Model for Multiple Harmonics Generation in Metallic Nanostructures,” *ACS Photonics* **2**(1), 8–13 (2015).
- [85] A. Hille, M. Moferdt, C. Wolff, C. Matyssek, R. Rodríguez-Oliveros, C. Prohm, J. Niegemann, S. Grafström, L. M. Eng, and K. Busch, “Second Harmonic Generation from Metal Nano-Particle Resonators: Numerical Analysis On the Basis of the Hydrodynamic Drude Model,” *J. Phys. Chem. C* **120**(2), 1163–1169 (2016).
- [86] T. Paul, C. Rockstuhl, and F. Lederer, “Integrating cold plasma equations into the Fourier modal method to analyze second harmonic generation at metallic nanostructures,” *Journal of Modern Optics* **58**(5-6), 438–448 (2011).
- [87] K. O’Brien, H. Suchowski, J. Rho, A. Salandrino, B. Kante, X. Yin, and X. Zhang, “Predicting nonlinear properties of metamaterials from the linear response,” *Nat. Mater.* **14**, 379 (2015).
- [88] M. L. Nesterov, M. Schäferling, K. Weber, F. Neubrech, H. Giessen, and T. Weiss, “Line-current model for deriving the wavelength scaling of linear and nonlinear optical properties of thin elongated metallic rod antennas,” *J. Opt. Soc. Am. B* **35**(7), 1482–1489 (2018).

- [89] B. Bai and J. Turunen, “Fourier modal method for the analysis of second-harmonic generation in two-dimensionally periodic structures containing anisotropic materials,” *JOSA B* **24**, 1105–1112 (2007).
- [90] T. Paul, C. Rockstuhl, and F. Lederer, “A numerical approach for analyzing higher harmonic generation in multilayer nanostructures,” *JOSA B* **27**, 1118–1130 (2010).
- [91] D. M. Whittaker and I. S. Culshaw, “Scattering-matrix treatment of patterned multilayer photonic structures,” *Phys. Rev. B* **60**, 2610–2618 (1999).
- [92] S. V. Lobanov, T. Weiss, D. Dregely, H. Giessen, N. A. Gippius, and S. G. Tikhodeev, “Emission properties of an oscillating point dipole from a gold Yagi-Uda nanoantenna array,” *Physical Review B* **85**, 155,137 (2012).
- [93] N. Bonod, E. Popov, and M. Nevière, “Fourier factorization of nonlinear Maxwell equations in periodic media: application to the optical Kerr effect,” *Opt. Commun.* **244**, 389–398 (2005).
- [94] S. Neale and E. A. Muljarov, “Resonant-state expansion for planar photonic crystal structures,” *Phys. Rev. B* **101**, 155,128 (2020).
- [95] P. Vincent, N. Paraire, M. Neviere, A. Koster, and R. Reinisch, “Gratings in nonlinear optics and optical bistability,” *J. Opt. Soc. Am. B* **2**(7), 1106–1116 (1985).
- [96] I. V. Lindell, A. H. Sihvola, S. Tretyakov, and A. J. Viitanen, *Electromagnetic Waves in Chiral and Bi-Isotropic Media* (Artech House, London, 1994).
- [97] A. H. Sihvola and I. V. Lindell, “Bi-isotropic constitutive relations,” *Microw. Opt. Technol. Lett.* **4**, 295–297 (1991).
- [98] M. Decker, M. Ruther, C. Kriegler, J. Zhou, C. Soukoulis, S. Linden, and M. Wegener, “Strong optical activity from twisted-cross photonic metamaterials,” *Opt. Lett.* **34**, 2501 (2009).
- [99] M. Schäferling, D. Dregely, M. Hentschel, and H. Giessen, “Tailoring enhanced optical chirality: design principles for chiral plasmonic nanostructures,” *Phys. Rev. X* **2**, 031,010 (2012).

- [100] M. Schäferling, N. Engheta, H. Giessen, and T. Weiss, “Reducing the complexity: Enantioselective chiral near-fields by diagonal slit and mirror configuration,” *ACS Photonics* **3**, 1076 (2016).
- [101] M. Hentschel, T. Utikal, H. Giessen, and M. Lippitz, “Quantitative Modeling of the Third Harmonic Emission Spectrum of Plasmonic Nanoantennas,” *Nano Lett.* **12**, 3778 (2012).
- [102] L. V. Poulikakos, P. Gutsche, K. M. McPeak, S. Burger, J. Niegemann, C. Hafner, and D. J. Norris, “Optical chirality flux as a useful far-field probe of chiral near fields,” *ACS Photonics* **3**, 1619 (2016).
- [103] L. V. Poulikakos, P. Thureja, A. Stollmann, E. De Leo, and D. J. Norris, “Chiral light design and detection inspired by optical antenna theory,” *Nano Lett.* **18**, 4633 (2018).
- [104] J. Garcia-Guirado, R. A. Rica, J. Ortega, J. Medina, V. Sanz, E. Ruiz-Reina, and R. Quidant, “Overcoming diffusion-limited biosensing by electrothermoplasmonics,” *ACS Photonics* **5**, 3673 (2018).
- [105] G. Baffou and R. Quidant, “Nanoplasmonics for chemistry,” *Chem. Soc. Rev.* **43**, 3898 (2014).
- [106] M. J. Huttunen, G. Bautista, M. Decker, S. Linden, M. Wegener, and M. Kauranen, “Nonlinear chiral imaging of subwavelength-sized twisted-cross gold nanodimers,” *Opt. Mater. Express* **1**, 46 (2011).
- [107] V. K. Valev, J. Baumberg, B. De Clercq, N. Braz, X. Zheng, E. Osley, S. Vandendriessche, M. Hojeij, C. Blejean, and J. Mertens, “Nonlinear superchiral metasurfaces: tuning chirality and disentangling nonreciprocity at the Nanoscale,” *Adv. Mater.* **26**, 4074 (2014).
- [108] J. Byers, H. Yee, and J. Hicks, “A second harmonic generation analog of optical rotatory dispersion for the study of chiral monolayers,” *J. Chem. Phys.* **101**, 6233 (1994).
- [109] S. Chen, G. Li, F. Zeuner, W. Han Wong, E. Yue Bun Pun, T. Zentgraf, K. Wai Cheah, and S. Zhang, “Symmetry-Selective Third-Harmonic Generation from Plasmonic Metacrystals,” *Phys. Rev. Lett.* **113**, 033,901 (2014).

- [110] J. Zuloaga and P. Nordlander, “On the energy shift between nearfield and far-field peak intensities in localized plasmon systems,” *Nano Lett.* **11**, 1280 (2011).
- [111] R. Taubert, M. Hentschel, J. Kästel, and H. Giessen, “Classical Analog of Electromagnetically Induced Absorption in Plasmonics,” *Nano Lett.* **12**, 1367 (2012).
- [112] R. Taubert, M. Hentschel, and H. Giessen, “Plasmonic analog of electromagnetically absorption: simulations, experiments, and coupled oscillator analysis,” *J. Opt. Soc. Am. B* **30**, 3123 (2013).
- [113] S. V. Lobanov, W. Langbein, and E. A. Muljarov, “Resonant-state expansion applied to three-dimensional open optical systems: Complete set of static modes,” *Phys. Rev. A* **100**, 063,811 (2019).
- [114] B. Bai and L. Li, “Group-theoretic approach to enhancing the Fourier modal method for crossed gratings with one or two reflection symmetries,” *Journal of Optics A: Pure and Applied Optics* **7**(7), 271–278 (2005).
- [115] B. Bai and L. Li, “Group-theoretic approach to the enhancement of the Fourier modal method for crossed gratings: C2 symmetry case,” *J. Opt. Soc. Am. A* **22**(4), 654–661 (2005).
- [116] B. Bai and L. Li, “Group-theoretic approach to enhancing the Fourier modal method for crossed gratings with C4symmetry,” *Journal of Optics A: Pure and Applied Optics* **7**(12), 783–789 (2005).

Art work



 ACS Publications
Most Trusted. Most Cited. Most Read.

www.acs.org

Figure 6.1: ACS sensors, August 23, 2019, Volume 4, Issue 8.

Acknowledgment

In these lines, I would like to thank the people who helped me to achieve this work through their support in scientific and personal matters.

I am grateful to my supervisor Jun.-Prof. Dr. Thomas Weiss for giving me the opportunity to do my Ph.D. in the 4th-physics institute at the university of Stuttgart. He shared his deep enthusiasm for sciences and guided me during these last four years with regular meetings that were indispensable in the achievement of this work.

I express my gratitude to Prof. Dr. Lutz and Prof. Dr. Loth for agreeing to be my second examiner and the head of my committee and for taking the time to read my thesis.

I would like to thank the head of our institute Prof. Dr. Harald Giessen who always provided the best work conditions for us with the regular group meetings and our group trips, which were a great source of inspiration and motivation.

I am indebted to Dr. Christine von Rekowski who provided a precious help at my arrival in Stuttgart when my health condition was not the best. She also provided an indispensable help for administrative matters that I could have never done alone.

I wish to express my gratitude to Dr. Mario Hentschel, Dr. Lili Gui and Dr. Joachim Krauth for our collaboration in the projects about third harmonic generation and the many fruitful discussions.

Many thanks to Prof. Dr. Sergei Tikhodeev, our guest professor, who welcomed me in Russia and shared his knowledge through our discussions about my research topics and other interesting scientific matters.

As Ph. D. student, I spent most of my time working with computers and calculation servers. I thank all the people who helped me to keep the servers and the network operational. I thank Dr. Martin Schäferling who welcomed me in the team and made the best of our computers and servers, Tobias Pohl and Tim Meiler who shared the responsibility of network admin with me and did an awesome job.

I thank all my colleagues from the institute, Sascha Böhrkircher who accepted to proof read my thesis, Swaathi Upendar and Dr. Andy Steinmann who shared my office at different times during my Ph. D. and as a consequence, were the target of unexpected tricks on top of being involved in pretty random discussions, Florian Sterl and Florian Mörz who shared with me their interest for mountain biking and downhill, the theory group Steffen Both and Izzatjon Allayarov and Dr. Rodolphe Collin for our nice discussions.

Last but clearly not least, I deeply thank my parents André and Françoise Defrance for always supporting me in all situations, my brother Dr. Fabien Defrance who did and continue to show me the right way.

Josselin Defrance

29, Badstrasse, 70372 - Stuttgart - Germany

✉ joss.defrance@gmail.com

Education

- **Ph. D.** **Stuttgart University, Germany**
Topic: Theory of nonlinear plasmonics *Since November 2015*
- **Master Photonics: ENSSAT** **University of Rennes, France**
(École Nationale Supérieures des Sciences Appliquées et de Technologies)
Option: Nanotechnologies *2014 – 2015*
- **Engineer degree: ENSSAT** **University of Rennes, France**
(École Nationale Supérieures des Sciences Appliquées et de Technologies)
Speciality: Optronics *2011 – 2015*
- **Classe préparatoire aux grandes écoles** **Clermont Ferrand, France**
Specialty PSI, (Physics and engineer sciences) *2009 – 2011*
- **Bacalauréat** **Riom, France**
2009

Professional experiences

- **Ph.D.** **Stuttgart, Germany**
4th Physics Institute, Stuttgart University *2015-2020, 4 years & 6 months*
 - Implementation of an algorithm based on the Fourier modal method and the scattering matrices formalism that calculates the second-harmonic generation in multilayers made of stacked 1D and 2D gratings.
 - Development of an algorithm based on the reciprocity principle that computes third-harmonic generation inside metallic nanostructures exhibiting dark mode hybridization or owning a chiral geometry.
 - Development of a numerical method based on the Mittag-Leffler expansion calculating electromagnetic field distribution and harmonic generation inside nanostructures.
- **Research assistant on the Moosh project** **Clermont Ferrand, France**
Pascal institute *2015, 6 months*
 - Implementation of a numerical code modelling the propagation of electromagnetic plane-waves through multi-layers made of homogeneous slabs.
 - Development an algorithm modelling the emission of sources inside multi-layers and calculating the loss in individual layers
- **Research assistant on the LISE project** **Ubaye Valley, France**
(Laboratory of Stellar and Exoplanetary Interferometry), University of Nice *2013, 1 month*
 - Alignment of the primary and secondary mirrors by the mean of an informatic servo-system
- **Research assistant** **Clermont Ferrand, France**
Pascal institute *2012, 1 month*
 - Modelling of lenses made with meta-materials with the software COMSOL

Skills

Computing.....

- o **Operating systems:** Windows (7,10), Linux (Ubuntu, Debian)
- o **Programming languages:** Latex, Html, matlab, Php, C
- o **Softwares:** COMSOL, Matlab, Octave, Blender

Languages.....

- o **French:** Native
- o **English:** Fluent
- o **German:** A1 level
- o **Spanish:** A1 level

Publications

Pole expansion of electromagnetic fields

J. Defrance, and T. Weiss, (in preparation)

Nonlinear Born-Kuhn Analog for Chiral Plasmonics

L. Gui, M. Hentschel, J. Defrance, J. Krauth, T. Weiss, and H. Giessen, *ACS Photonics* **6**, 3306 (2019).

Nonlinear Spectroscopy on the Plasmonic Analog of Electromagnetically Induced Absorption: Revealing Minute Structural Asymmetries

J. Krauth, T. Schumacher, J. Defrance, B. Metzger, M. Lippitz, T. Weiss, H. Giessen, and M. Hentschel, *ACS Photonics* **6**, 2850 (2019).

Modeling of second-harmonic generation in periodic nanostructures by the Fourier modal method with matched coordinates

J. Defrance, M. Schäferling, and T. Weiss, *Opt. Express* **26**, 13746 (2018).

Presentations

DPG Spring Meeting 2019 (Rostock), *Modeling of harmonic generation in plasmonic structures with complex geometries*, Josselin Defrance, Lili Gui, Mario Hentschel, Harald Giessen, and Thomas Weiss.

DPG Spring Meeting 2018 (Berlin), *Numerical modeling of second harmonic generation in metal nanoantennas*, Josselin Defrance, and Thomas Weiss.

11th Annual Meeting Photonic Devices 2018 (Berlin), *Modeling of second-harmonic generation in the Fourier modal method with matched coordinates*, Josselin Defrance.

PIERS Meeting 2017 (St. Petersburg), *Modeling of Higher Harmonic Generation in the Fourier Modal Method with Adaptive Coordinates*, Josselin Defrance, Martin Schäferling, Maxim L. Nesterov, and Thomas Weiss.

DPG Spring Meeting 2017 (Dresden), *Modeling of higher harmonic generation with the Fourier modal method using adaptive coordinates*, Josselin Defrance, Martin Schäferling, Maxim L. Nesterov, and Thomas Weiss.

